IDENTIFICATION OF OPTIMUM AGGREGATE GRADATION FOR TRANSPORTATION APPLICATIONS OF MULTIAXIAL GEOGRIDS

A Thesis
Presented to
The Academic Faculty

by

Andres F. Peralta

In Partial Fulfillment
of the Requirements for the Degree
Master of Science in the
School of Civil and Environmental Engineering

Georgia Institute of Technology
December 2016

IDENTIFICATION OF OPTIMUM AGGREGATE GRADATION FOR TRANSPORTATION APPLICATIONS OF MULTIAXIAL GEOGRIDS

Approved by:

Dr. J. David Frost, Advisor
School of Civil and Environmental Engineering
Georgia Institute of Technology

Dr. Susan E. Burns
School of Civil and Environmental Engineering
Georgia Institute of Technology

Dr. Mark Wayne
Director of Application Technology
Tensar International Corporation

Date Approved: 8/22/2016

ACKNOWLEDGEMENTS

The successful culmination of this important stage in my personal and professional life could not have been possible without the support and continued encouragement from several individuals and institutions.

First of all, I would like to express my sincere gratitude to my advisor Dr. J. David Frost for his support and guidance throughout my time at Georgia Tech, for believing in me, and for providing me with the opportunity to become a better geotechnical engineer. His insight on the microscale behavior of soils, and his mindset to approach the problem from alternative directions, have provided me with invaluable lessons, for which I will always be grateful.

I would like to thank Dr. Susan Burns for her lessons and guidance, since my days as an undergraduate student, and also for giving me the opportunity to assist her as the instructor of the soils laboratory class. This experience taught me important lessons, which allowed me to grow in both personal and professional aspects.

I would also like thank Dr. Mark Wayne, from Tensar International Corporation, and Dr. Jayhyun Kwon, from Kennesaw State University, for their confidence in this project, their constant guidance, and their support throughout these two years.

A special word of thanks goes to Dr. Chloe Arson for giving me the opportunity to conduct research in Paris, France at *Ecole Nationale Des Ponts Et Chaussées (ENPC).* This has been one of the most constructive personal and professional experiences that I

have ever encountered, and for that I am really thankful. I would also like to extent my gratitude to Dr. Jean-Michel Pereira at ENPC for his invaluable input on the DEM modeling of multiaxial geogrids during my visit.

This accomplishment would not have been possible without my parents and my family, who have always been there to support my goals and dreams, since I can remember. I would like to express my deepest gratitude to my father Hernan Estrada and my mother Nydia Peralta for all the hard work they have endured, in order to provide me with the tools necessary to succeed in life. I would also like to thank my brother Santiago Estrada, my aunt Belsy Peralta, my cousin Julio Rodriguez, and the rest of my family in Colombia for their constant support and endless love.

In the last two years, I have had the opportunity to make great friendships in the Geosystems department, and these have been a huge support during my graduate studies. I would like to specially thank Alejandro Martinez, Albert Liu, Jackson Su, Jie Cao, Fikret Atalay, Sangy Hanumasagar, Josh Smith, Xenia Wirth, and Longde Jin. A really special thanks goes to Mahdi Roozbahani for all the great discussions, and the help provided throughout this project. His incessant desire to discovery the meaning behind multiple challenges encountered during this study was very instructive.

Finally, I would like to thank all my friends here in Atlanta, who have been my pillar through this time. I would like to specially thank Pablo Casas, Jimena Romero-Casas, Mauricio Reyes, Eduardo Rivera, Francisco Urdaneta, and Renato Vargas for their constant support and encouragement.

TABLE OF CONTENTS

ACKNOWLEDGEMENTS……iii

LIST OF TABLES……..ix

LIST OF FIGURES……xi

SUMMARY……....xviii

CHAPTER I: INTRODUCTION 1

CHAPTER II: LITERATURE REVIEW 5

2.1 Introduction 5

2.2 Early studies on geogrid-reinforced granular materials 6

2.2.1 Surface rutting of geogrid-reinforced structures 6

2.2.2 Geogrid optimum location 9

2.2.3 Ideal aggregate layer thickness 10

2.2.4 Optimum subgrade strength 11

2.2.5 Geogrid reinforcing mechanisms 12

2.2.6 Design Methodologies 14

2.3 Current studies on geogrid-reinforced granular materials 25

2.3.1 Laboratory experimentation 25

2.3.2 Numerical simulations using the Discrete Element Method (DEM) 30

2.4 Closing thoughts 40

CHAPTER III: STUDY, QUANTIFICATION, AND MODELING OF AGGREGATE MORPHOLOGY 41

3.1 Intoduction 41

3.2 Image analysis of aggregate particles 44

3.2.1 Geographical location and mineralogy of aggregate 44

3.2.2 Image analysis of aggregate using the University of Illinois Aggregate Image Analyzer (UIAIA) 47

3.3 DEM modeling of aggregate particles 55

3.3.1 Quantification of the AI, FE Ratio, and ST Index by the UIAIA 55

3.3.2 DEM Modeling of Aggregate Particles 57

3.4 Conclusion 69

CHAPTER IV: GEOGRID MODELING 70

4.1 Introduction 70

4.2 Discrete element modelling using PFC3D 71

4.2.1 Overview of the Distinct Element Method and PFC3D 71

4.3 Physical laboratory testing of multiaxial geogrid ribs and results 83

4.3.1 Geogrid specimens used in this test. 83

4.3.2 Single rib tensile test - Modified ASTM D6637 84

4.4 Numerical model 89

4.4.1 Previous studies on DEM modeling of geogrids 89

4.4.2 Development of micromechanical parameters for geogrid model 91

4.4.3 Calibration results 94

4.4.4 Flexural rigidity of geogrids 97

4.4.5 Geogrid geometry generation 108

4.5 Conclusions 112

CHAPTER V: DEM SIMULATION OF CYCLIC LOAD TEST ON GEOGRID STABILIZED AND NON-STABILIZED BINARY MIXTURES 114

5.1 Introduction 114

5.2 Particle gradation 114

5.2.1 Previous studies 115

5.2.2 Determination of particle gradation 119

5.3 DEM Simulation of geogrid stabilized aggregate under cyclic loading 121

5.3.1 Cycling loading test setup 121

5.3.2 Preparation and cyclic loading test of geogrid stabilized and non-stabilized binary mixtures 124

5.4 Results and discussion 126

5.5 Conclusion 146

CHAPTER VI: CONCLUSIONS AND FUTURE WORK 148

6.1 Conclusions 148

6.2 Future Work 150

APPENDIX A: Angularity index calculation of a triangle 153

APPENDIX B: Calculation of a 24-sided polygon for image analysis purposes 156

REFERENCES.....159

LIST OF TABLES

Table 3.1 Mineralogy and aggregate reference group of aggregate samples used in the study (GDOT, 2016). 44

Table 3.2 Average AI and FE Ratio values of the different aggregate specimens. 54

Table 3.3 Average ST Index and FE ratio of four different aggregate specimens 54

Table 3.4 Summary of the results obtain from the AI analysis on multiple clumps with different amount of pebbles. 64

Table 3.5 Summary of AI and FE ratio of 3D printed clumps. 66

Table 4.1 Single rib tensile test results 87

Table 4.2 Summary of geogrid material and geometrical parameters obtained from physical testing. 93

Table 4.3 Summary of multiaxial geogrid DEM model geometrical properties 94

Table 4.4 Micromechanical parameters computed for modeling TX130S, TX140, and TX190L multiaxial geogrids. 94

Table 4.5 Flexural rigidity of TX190L. 101

Table 4.6 Flexural rigidity of DEM model of TX190L. 101

Table 4.7 Radius multiplier required for an equivalent second moment between the actual geogrid and the geogrid DEM model. 102

Table 4.8 Summary of flexural rigidity of TX190L 103

Table 4.9 Summary of the number of spheres per multiaxial geogrid specimen. 111

LIST OF FIGURES

Figure 2.1. Chart for the design of geogrid-reinforced unpaved structures (Giroud et al., 1985) 16

Figure 2.2 Tensar geogrid-reinforced base thickness for flexible pavements (Carroll and Hass, 1987) 18

Figure 2.3 Interaction diagram of normal and shear stress for failure of a strip footing (Milligan et al., 1989) 20

Figure 2.4 Shear strength conversion nomograph from COE design method (Tingle and Webster, 2003). 21

Figure 3.1 Geological map of the State of Georgia displaying the location of the different quarries (USGS, 2005). 45

Figure 3.2 Aggregate particles retained in the 25.4 mm sieve from each aggregate specimen. 46

Figure 3.3 UIAIA capturing the images of each particle to quantify their morphological properties. 48

Figure 3.4 Set of images captured by the UIAIA, and their respective binary images 48

Figure 3.5 Angularity Index results for each aggregate particle in each aggregate specimen from (a). Dalton, (b). Hitchcock, (c). Norcross, and (d). Walton Co. quarries . 51

Figure 3.6 Flat and Elongated Ratio results for each aggregate particle in each aggregate specimen from (a). Dalton, (b). Hitchcock, (c). Norcross, and (d). Walton Co. quarries . 52

Figure 3.7 Surface Texture index results for each aggregate particle in each aggregate specimen from (a). Dalton, (b). Hitchcock, (c). Norcross, and (d). Walton Co. quarries .53

Figure 3.8 . PFC3D visualization of a three-pebble and a two-pebble clump (Itasca, 2015). 58

Figure 3.9 Front view of the three-pebble clump used as the main unit for generating clumps of varying AI 60

Figure 3.10 Step-by-step computation of angularity on the projection of the top view of a four-pebble clump. 61

Figure 3.11 (a). Front, top, and side views of a seven-pebble clump. (b). Front, top, and side views of clump outlined with five polygons of equal side lengths. (c). 24-sided polygon outlining each view of the clump. 62

Figure 3.12 Variation of the top views of the main clump unit as additional spheres are added to change the AI of the clump 63

Figure 3.13 3-D printed clumps used to perform image analysis 65

Figure 3.14 UIAIA Image analysis on a 3D printed clump.....66

Figure 3.15 Computed (Image Analysis) and hand-calculated (Calculation) AI values of clumps 3D prints. 67

Figure 3.16 Angle of repose of a pile of (a.) spheres (b.) 3-pebble clumps, (c.) 5-pebble clumps, (d.) 6-pebble clumps, (e.) 9-pebble clumps, and (f.) 11-pebble clumps with equal coefficient of friction. 68

Figure 4.1 Relation of normal stiffness to piece normal stiffnesses for the linear model (Itasca, 2015) 74

Figure 4.2 Behavior and rheological components of the linear model (Itasca, 2015) 74

Figure 4.3 Contact plane coordinate system for 2D and 3D model (in tensor notation) (Itasca, 2015) 76

Figure 4.4 Parallel bond representation 79

Figure 4.5 Linear parallel contact method (Itasca, 2015) 80

Figure 4.6 Specimens of TX130S, TX140, and TX190L 84

Figure 4.7 Figure 4.7. TX130S, TX140, and TX190L specimens for single rib tensile testing 85

Figure 4.8 Single rib tensile test setup 86

Figure 4.9 Sample of the Force vs. Displacement curve of TX190L specimen, and its stiffness at 0.5% strain 88

Figure 4.10 Variability of the stiffness at 0.5% strain of TX190L specimen 88

Figure 4.11 DEM model of biaxial geogrid Presented by Konietzky et al., 2004..... 90

Figure 4.12 DEM model of biaxial geogrid Presented by Chen, et al., 2013..... 90

Figure 4.13 Single rib tensile test DEM simulation performed on a TX190L rib..... 95

Figure 4.14 Single rib extension simulation and experimental data for TX130S calibration 96

Figure 4.15 Single rib extension simulation and experimental data for TX140 calibration 96

Figure 4.16 Single rib extension simulation and experimental data for TX190L calibration 97

Figure 4.17 (a).TX190L specimen under compressive forces, (b). TX190L DEM specimen under compressive forces 98

Figure 4.18 Second moment of area equations for (a). geogrid specimen and (b).DEM model 101

Figure 4.19 Flexural rigidity evaluation of TX190L based on ASTM D7748..... 103

Figure 4.20 Flexural rigidity test simulation setup 104

Figure 4.21 (a). Isometric and (b). Side view of flexural rigidity simulation results for a geogrid model with λ = 1.14 105

Figure 4.22 (a). Side and (b). Isometric view of TX190L at initial state before applying a compressing force 106

Figure 4.23 Geogrid compression deformation results for geogrid specimens modeled with different radius multiplier values after 50,000 steps. 107

Figure 4.24 (a). Geogrid mesh drawn in Rhinoceros (b)..Geogrid modeled as a wall in PFC3D 109

Figure 4.25 (a). Geogrid CAD drawing (b). Geogrid PFC3D model visualization 110

Figure 4.26 TX190L DEM model visualized in PFC3D 111

Figure 5.1 Maximum observed packing of binary mixtures of spheres (McGeary, 1961) 116

Figure 5.2 Volume reduction ratio for different particle size ratios (PSR). (Fuggle et al., 2014) 117

Figure 5.3 Packing states of gravel-sand-fines with different gravel-to-sand ratios: (a) Large, (b) optimum, and (c) small. (Xiao et. al, 2012) 118

Figure 5.4 Idealized binary mixture configuration inside geogrid aperture in PFC.....120

Figure 5.5 DEM model setup with spheres 121

Figure 5.6 Graphical representation of a periodic boundary (O'Sullivan, 2011).....123

Figure 5.7 Particle movement in PBC (O'Sullivan, 2011) 124

Figure 5.8 (a.) Initial condition for a non-stabilized binary mixture – 50% and its (b.) cross-section prior to cyclic load application (c.) Initial condition for a geogrid stabilized binary mixture – 50% and its (d.) cross-section prior to cyclical load application 127

Figure 5.9 (a.) Final condition non-stabilized binary mixture – 50% and its (b.) cross-section after the application of 500 load cycles (c.) Final condition geogrid stabilized binary mixture – 50% and its (d.) cross-section after the application of 500 load cycles.....128

Figure 5.10 (a.) Initial condition for a non-stabilized binary mixture – 70% and its (b.) cross-section prior to cyclic load application (c.) Initial condition for a geogrid stabilized binary mixture – 70% and its (d.) cross-section prior to cyclical load application 129

Figure 5.11 (a.) Final condition for a non-stabilized binary mixture – 70% and its (b.) cross-section after the application of 500 load cycles (c.) Final condition for a geogrid stabilized binary mixture – 70% and its (d.) cross-section after the application of 500 load cycles 130

Figure 5.12 Surface displacement comparison between geogrid stabilized and non-stabilized binary mixtures – 50% after 500 loading cycles.....131

Figure 5.13 Surface displacement comparison between geogrid stabilized and non-stabilized binary mixture – 70% after 500 cycles 132

Figure 5.14 Interaction between (a.) lower and (b.) upper layer of binary mixture – 50% and multiaxial geogrid layer at 500 loading cycles.....134

Figure 5.15 Interaction between (a.) lower and (b.) upper layer of binary mixture – 70% and multiaxial geogrid layer at 500 loading cycles.....135

Figure 5.16 (a). Parallel bond forces and (b.) tensile and compressive forces developed within the geogrid layer for a binary mixture – 50% at 500 loading cycles.....137

Figure 5.17 (a). Parallel bond forces and (b.) tensile and compressive forces developed within the geogrid layer for a binary mixture – 70% at 500 loading cycles.....138

Figure 5.18 Porosity evolution for both binary mixture – 50% and binary mixture - 70% at the geogrid location.....140

Figure 5.19 Evolution of porosity reduction with respect to n_{Max} for both binary mixture – 50% and binary mixture - 70% at the geogrid location.....141

Figure 5.20 Porosity evolution of the particles underneath the geogrid layer location for a binary mixture – 50% 143

Figure 5.21 Evolution of porosity reduction with respect to n_{Max} for both binary mixture – 50% underneath the geogrid layer location.....144

Figure 5.22 Porosity evolution of the particles underneath the geogrid layer location for a binary mixture – 70% 145

Figure 5.23 Evolution of porosity reduction with respect to n_{Max} for both binary mixture – 70% underneath the geogrid layer location.....146

SUMMARY

The stabilizing effect of multiaxial geogrids on aggregate materials is largely influenced by the morphological properties of the aggregate, such as its size, angularity, and surface roughness, and the overall aggregate gradation. In order to evidence this phenomenon at the microscale level, a Discrete Element Method (DEM) model, which considered these properties was developed.

The morphological properties of different aggregate specimens across the State of Georgia were quantified, by utilizing the University of Illinois Aggregate Image analyzer (UIAIA). The indices obtained from this procedure, such as the Flat-and-Elongated (FE) ratio, the Angularity Index (AI), and the Surface Texture (ST) Index were used to model aggregate particles as clumps using the Particle Flow Code (PFC) 3D software.

DEM models for three different types of multiaxial geogrids (TX130S, TX140, and TX190L) were developed, by implementing the PFC3D parallel-bond contact method. These models were calibrated against physical data obtained from single rib tensile tests of multiple rib specimens from each geogrid type.

The stabilizing effect of multiaxial geogrids was assessed by performing simulations of cyclic load tests on binary mixtures with a particle size ratio of 2.1. Two binary mixtures, identified as binary mixture – 50% and binary mixture – 70%, were used in this study. The binary mixture – 50% had a D_{max} equal to 30 mm and a D_{min} equal to 14.3 mm, while the binary mixture – 70% had a D_{max} equal to 40 mm and a D_{min} equal to 20 mm. From the results obtained from the simulations, it was observed that the stabilized

binary mixture – 50% exhibited smaller surface deformations due to cyclic loading, in comparison to the unsterilized case; however, it was also observed that both geogrid stabilized and non-stabilized binary mixture – 70% exhibited significant surface deformations, and the magnitude of these deformations was the same for both binary mixture – 70% specimens with and without a multiaxial geogrid layer.

This DEM model was effective in providing an insight into the behavior of this composite system, since it permitted the examination of particle interlocking, and the development of tensile and compressive force chains within the multiaxial geogrid model. From these results, it was possible to visually determine that optimal interlocking existed between the binary mixture – 50% and the multiaxial geogrid model. It was also noticed that minor interlocking was developed between the binary mixture – 70% and the multiaxial geogrid model, which explained its poor performance and the development of the same amount of surface deformation between the specimens with and without a multiaxial geogrid layer.

Finally, it was evidenced that the optimum interaction between the binary mixture – 50% and the multiaxial geogrid layer hindered the surface deformation by 33% with respect to the non-stabilized case. Furthermore, no stabilizing benefit was observed for the case where the binary mixture – 70% was used.

CHAPTER I: INTRODUCTION

Since their invention in the late 1970's, and their introduction into the market in the early 1980's, geogrids have been used to stabilize the base and subbase aggregate layers in paved and unpaved roadways, reduce the amount of aggregate used for the construction of these structures, augment their service life, and reduce their construction cost (Koerner, 2009; Jenner, 2009).

Due to their ability to enhance the design and construction of roadways, a need to understand the key reinforcing mechanisms of geogrids in granular media arose from the moment they were introduce to the civil engineering community. Throughout these last three and a half decades multiple studies have taken place with the sole purpose of identifying those key reinforcing mechanisms and understanding them.

The first studies carried out to fulfill this purpose were focused on assessing the benefits of using geogrids as a granular reinforcement material, by either comparing the overall roadway surface deformation between reinforced and unreinforced sections (Haas et al., 1987; Chan et al., 1989; Webster, 1993), or by observing the stresses and strains developed in the different layers of the roadway section (Giroud et al., 1985). These studies were purely experimental and lacked the tools necessary to observe or predict the behavior and interaction of the individual grains inside the granular layer; therefore, the approach to study this matter focused on assessing these composite structures as a continuum material instead of a granular one.

From the studies carried out from the early 1980's through the early 2000's, many design methodologies for geogrid reinforced paved and unpaved roadways were proposed. These design methodologies manly focused on assessing the bearing capacity of the subgrade, by means of plasticity theory; specifying a type of aggregate capable of distributing the traffic load over a large area; and including a geogrid layer stiff enough to confine the aggregate, sustain the lateral forces developed inside the aggregate layer, and, in some cases, create a tension membrane effect (Giroud et al., 1985; Milligan et al., 1989; Tingle & Webster, 2003). However, it was not possible to reach a consensus on a widely accepted procedure to design geogrid reinforced roadways, because it was not clear which one of these methods comprised all the necessary components to develop an effective design, and avoided introducing multiple dependent variables to the problem that significantly affected the outcome (Perkins, 1997).

By the mid 2000's, Giroud and Han developed a new design methodology for unpaved geogrid reinforced roads and trafficked areas (Giroud and Han, 2004). This design methodology was motivated by the necessity of having a technique that yielded more accurate predictions than the previously proposed design methodology by Giroud in 1985 (Giroud and Han, 2004). This method was developed empirically, by using data obtained from different studies, but it provided an analytical component to the solution as well. The main differences between their newer method and the one previously proposed was that this method accounted for the interlocking between the geogrid and the aggregate, the in-plane aperture stability modulus of the geogrid, and the resilient modulus of the aggregate (Giroud and Han, 2004).

The Giroud and Han design method, and other studies carried out at the time became aware of the importance of size compatibility between the aggregate particles

and the aperture of the geogrid, in order to generate enough interlock, and thus develop a superior design methodology (Brown et al, 2007; Indraratna et al., 2012); however, these micromechanical process were difficult to observe and quantify, by only performing laboratory experimentation; there remained a need to look inside the aggregate, and specifically at the aggregate-geogrid interaction.

The power of computers rapidly grew, and by the mid 2000's, the first approaches to observe the interaction between geogrids and aggregate particles at the microscale were possible thanks to the Discrete Element Method (DEM), and powerful computing software dedicated to perform studies using such approaches. Most of these studies focused on observing the geogrid performance at different locations within the aggregate layer (Konietzky et al., 2004; Chen et al., 2012), or observing the development of force chains during geogrid pullout tests (Konietzky et al., 2004, McDowell et al., 2006, Stahl et al., 2014). These studies yielded important results useful to answer some of the questions regarding the key micromechanical parameters influencing the performance of geogrid-reinforced unpaved roads.

Recent DEM studies regarding geogrid/aggregate interaction have focused on modeling aggregate particles as closely as possible to their real counterparts; however, a DEM model that utilizes a methodology capable of quantifying the morphological properties of aggregate particles and the overall gradation of the aggregate specimen to effectively study their interaction, has not yet been developed. This knowledge gap between physical experimentation and numerical modeling has motivated the study of the interaction between aggregate particles and multiaxial geogrids, by utilizing the DEM software Particle Flow Code (PFC) 3D.

The first objective of this study is to develop a numerical model capable of representing the geogrid's physical behavior, the aggregate's morphology, and the interaction between these two materials. The second objective of this study is to use this numerical model to identify the optimum aggregate gradation for transportation applications for three types of multiaxial geogrids manufactured by Tensar International Corporation: TX130S, TX140, and TX190L.

This document is organized in the following order:

Chapter II presents a literature review of the relevant work performed on geogrid-reinforced aggregate materials since the late 1980's to the present.

Chapter III presents the study, quantification, and modeling of aggregate morphology.

Chapter IV describes the development of the geogrid model in PFC.

Chapter V presents the setup and results from the DEM cyclic loading simulation of geogrid-stabilized binary mixtures.

Chapter VI presents the conclusions, and the recommendations for future work of this study.

CHAPTER II: LITERATURE REVIEW

2.1 Introduction

The use of geogrids to improve the performance, and extend the service life of paved and unpaved roads, began in the early 1980's; however, a clear understanding of the mechanisms involved in enhancing the behavior of these structures was not available at that time. In an effort to better understand the reinforcing properties of geogrids and the parameters that controlled their optimal behavior, different studies began taking place in the late 1980's. From these studies, it was possible to identify some of the key parameters and main reinforcing mechanisms, which allowed geogrids to enhance the performance of granular materials; however, the lack of approaches to study the behavior inside the granular material, made the identification of these key parameters and reinforcing mechanisms incomplete.

From the mid 2000's until today, the fast proliferation of computer power, in conjunction with the Discrete Element Method (DEM), has provided the necessary tools for researchers to: model the behavior of geogrid-reinforced aggregate and observe its micromechanical behavior; compare the results obtained from these numerical simulations to the results obtained from physical experimentation; and draw conclusions about the main reinforcing mechanisms of geogrids from a micromechanical standpoint. This approach has provided valuable results, which match physical experimentation results, and has proven to be an ideal approach to fully study this subject.

The main objective of this chapter is to review the most relevant studies performed on geogrid-reinforced aggregate materials for the past thirty years, identify the main

parameters and mechanisms found responsible for providing the reinforcing effect, and demonstrate that aggregate morphology and aggregate gradation are key parameters that influences the optimal performance of geogrid-reinforced aggregate base layers in transportation applications and need to be further studied.

2.2 Early studies on geogrid-reinforced granular materials

The early studies regarding geogrid-reinforced aggregate materials, which included studies on paved roads, unpaved roads, railroads, airplane runways, and foundations, focused on assessing the benefit of including geogrids within these structures by observing their macroscale behavior under loading. These studies focused on comparing the surface rutting of geogrid-reinforced versus unreinforced structures; the influence of the geogrid location within the aggregate layer; the influence of the aggregate layer thickness; and the influence of the subgrade strength. After these comprehensive studies were concluded, reinforcement mechanisms for geogrid-reinforce aggregate base layers were theorized, and multiple design methodologies for these structures were proposed. A brief summary of the most influential studies, and their findings, is presented next.

2.2.1 Surface rutting of geogrid-reinforced structures

Hass and Carroll (1987) made a comparison between geogrid-reinforced and unreinforced aggregate base layers of varying thickness in flexible pavements. These geogrid-reinforced pavement test sections were built over weak and strong subgrade layers inside a large steel box. The geogrid layer location was varied within the aggregate base layer, in order to assess its impact on the performance of the pavement section. After testing six different pavement sections, all of them with varying subgrade strength, aggregate base layer thickness, or geogrid location, the authors drew conclusions about the impact that each one of those parameters had on the performance of the geogrid. With

regards to rutting of the surface of the roadway, the authors concluded that geogrids improved its performance by a factor of three, since the pavement section sustained three times more load than the unreinforced case before unacceptable rutting depths were observed on the surface of the road.

Chan et al. (1989), focused on studying the performance of flexible base pavements with geosynthetic-reinforced aggregate bases on pavement sections constructed on an open field. Comparative analyses were carried out on four different pavement sections, to assess the benefit of pre-rutting the aggregate and pre-stressing the reinforcement material. These results were also used to develop an analytical solution for this problem using a Finite Element Method (FEM) analysis. The study found that pre-stressing the geogrid layer slightly reduce the permanent deformation of the surface of the road as the number of loading cycles increased. It also identified that by pre-rutting the aggregate base layer and installing a geogrid layer in the middle of this one, the roadway section was able to sustain a rut 5 mm smaller than the same section with a pre-stressed geogrid layer after 100,000 cycles. The study concluded that geogrids delayed the formation of ruts in flexible pavements; however, the authors expressed that this highly depended on the quality and thickness of the aggregate base layer and the location of the geogrid.

Miura el at. (1990), studied the performance of geogrid-reinforced paved roadways built on weak clayey subgrades. For this study, laboratory experimentation, numerical simulations, and field investigations were performed. The laboratory experimentation focused on finding the optimal geogrid type and location for its installation, and determining the number of geogrid layers required for reaching the optimal performance of the section. The numerical simulation focused on modeling the behavior of the composite material, by using FEM analysis, in order to observe and understand the

reinforcing effect of the geogrid. Lastly, field investigations were carried out to test the efficacy of geogrid-reinforced paved roadways and report the amount of settlement observed. The results from the field investigation showed that the presence of a geogrid layer at the subgrade/aggregate base layer interface reduced the settlement of the road and rutting rate by 50% and 25% respectively after six months of service in comparison to an unreinforced section.

Webster (1993) assessed the performance of geogrid-reinforced runways for lightweight aircrafts. For the purpose of doing so, the author tested and compared the macroscale deformations of four runway lanes, which were constructed in a specific manner to accomplish the following: find the best location for geogrid placement, compare the different types of geogrids in the market at the time, and observe the influence that subgrade strength and aggregate thickness had on the performance of the system. The results of this study concluded that for airplane runways with an allowable surface rutting equal to 1”, geogrid reinforcement allowed them to sustain between 16.3 and 22.4 times more traffic than unreinforced runways.

Fanning and Sigurdsson (1996), performed laboratory experimentation on a geosynthetic-reinforced unpaved roadways constructed over a weak clayey organic silty subgrade. The road, which consisted of an aggregate layer that varied from 250mm to 500mm in thickness, was sub-divided into multiple test sections, and these were reinforced with different types of geotextiles and one type geogrid. The rut development rate and its profile observed on the surface of the geogrid-reinforced unpaved road section were monitored as the number of loading cycles increased. This study found that the inclusion of a geogrid layer improved the trafficability of the road, reduced the average rut depth by 80mm, and significantly slowed down the rut development and its depth.

Montanelli et al. (1997) studied geogrid-reinforced pavement sections, in order to develop an analytical solution for this problem. For the geogrid-reinforced section, a geogrid layer was placed in between the gravelly aggregate base and a sandy subgrade. It was observed that geogrid-reinforced sections performed significantly better than unreinforced ones, since rutting was reduced from 130 mm at 30,000 cycles to 60 mm at 50,000 cycles.

Leng and Garb (2002) studied the influence of aggregate base layer thickness and reinforcement type on unpaved roadways. This was accomplished by testing nine different sections with two different types of extruded polypropylene biaxial geogrids of varying stiffness (BX1 and BX2), and two different aggregate base layer thicknesses over weak subgrade. The study concluded that the inclusion of a geogrid layer in the aggregate base layer reduced the maximum vertical stresses at the subgrade/aggregate base layer interface, and improved the load distribution on the subgrade. In return, the rutting formation at the surface of the unpaved road decreased and the aggregate degradation slowed down. Furthermore, the study concluded that the stiffer the geogrid was, the less rutting formation would occur. The study demonstrated a surface deformation improvement of 20% to 30% for BX1 and BX2 respectively, with respect to the unreinforced case.

2.2.2 Geogrid optimum location

Several studies recognized that the placement of the geogrid layer within the aggregate was fundamental to obtain an optimal aggregate-reinforced road section. Several of these studies focus on this idea, so they tested road and runway sections with geogrid layers located either at the interface between the aggregate base layer and the

subgrade, or within the aggregate base layer. It was determined that for thin aggregate base layers, the optimum geogrid location was at the subgrade/aggregate base layer interface, (Hass and Carrol, 1987; Miura et al., 1990; Webster, 1993; Montanelli et al., 1997). It was also determined that for aggregate layers equal or greater than 250 mm in thickness, and constructed over stiff subgrades, the optimum geogrid location was at the middle of the aggregate base layer (Hass and Carrol, 1987; Webster 1991). Furthermore, it was determined that when geogrid layers are pre-stressed and installed in the middle of the aggregate base layer, they outperform the behavior of non-pre-stressed geogrid layers (Chan et al. 1989). Although this is the case, pre-stressing of polypropylene geogrids is not necessary, since these are stiff enough to reinforce the aggregate base layer without much deformation (Leng and Garb, 2002); moreover, quantifying the benefit of pre-stressing the geogrid is difficult, so this task could be problematic (Chan et al. 1989).

2.2.3 Ideal aggregate layer thickness

The reduction of the amount of aggregate required to construct an effective base layer was a common denominator in the early studies about geogrid-reinforced unpaved roadways. Multiple studies focused on calculating the aggregate base thickness reduction for geogrid-reinforced unpaved roads, by comparing the capacity of the geogrid-reinforced aggregate base layer against an unreinforced one of equivalent aggregate thickness (Hass and Carroll, 1987; Chan et al. 1989; and Webster 1993). These studies demonstrated that the inclusion of a geogrid layer at the subgrade/aggregate base layer interface allowed the reduction of the aggregate base layer thickness by 30% (Hufenus et al., 2006) to 50% (Hass and Carroll, 1987). These studies made it evident that geogrid-reinforced unpaved road sections with a thin aggregate layers showed a more prominent performance improvement; however, other studies argued that geogrids performed better on aggregate layers equal to 300 mm to 350 mm in thickness, since migration of fines only

occurred in a smaller percentage of the layer and did not affect the interparticle interaction of the aggregate (Fanning and Sigurdsson, 1996; Hufenus et al., 2006). Lastly, Fanning and Sigurdsson (1996) and Hufenus et al (2006) determined that the inclusion of geogrids in thicker aggregate sections of 500 mm and beyond, did not show appreciable improvement.

2.2.4 Optimum subgrade strength

Early studies indicated that subgrade strength played an important role in the performance of geogrid-reinforced structures, due to the fact that the reinforcing effect of geogrids was more prominent on weak subgrades; therefore, geogrids were rapidly identified as an optimum solution to construct roadways in weak subgrades (Miura et al., 1990).

In order to quantify the optimum subgrade stiffness at which geogrids performed better, multiple studies were performed on geogrid-reinforced road sections with varying subgrade strengths (Hass and Carroll, 1987; Miura et al., 1990, Webster, 1993, Montanelli et al., 1997). In most of these studies, the subgrade strength was presented as a California Bearing Ratio (CBR), and these ranged from 1% to up to 8%. These studies led to the conclusion that the structural contribution of the geogrid was much more appreciable on subgrade layers with a CBR values between 1%, and 5%. This conclusion was confirmed by a study performed by Barker (1987), which demonstrated that the reinforcing contribution provided by a geogrid layer on an aggregate base layer built on a highly stiff subgrade was negligible, and other aggregate reinforcing methods were preferable. Barker (1987) tested two 150 mm thick runway sections, which were built on a subgrade with a CBR equal to 27%. One section was reinforced with a geogrid layer and the other one with cement. The results showed that the runway section with the cemented

aggregate outperformed the section with the geogrid reinforcement by over 50% after 1000 cycles (Barker, 1987).

Although these studies identified the subgrade strength range for optimum geogrid performance, none of them explained the reason behind this phenomenon. Love et al., (1987) studied this problem as a foundation bearing capacity problem and noticed that the inclusion of a geogrid layer distributed the loads on the subgrade/aggregate base layer interface, and reduced the amount of shear stresses applied to the top of the subgrade. This load distribution improvement reduced the amount of deformation of the subgrade, and prevented vertical deformation of the aggregate base layer (Love et al., 1987). These conclusions suggested that the reinforcement impact of geogrids would only be noticeable on weak subgrades, due to the fact that stiff subgrades lack bearing capacity issues, and the load distribution provided by the geogrid is not essential for satisfactorily performance.

2.2.5 Geogrid reinforcing mechanisms

The reinforcement capacity of geogrids was attributed to different mechanisms, such as aggregate interlocking, aggregate confinement, subgrade confinement, and tensioned membrane effect (Giroud et al., 1985). Among most of these early studies, aggregate interlocking and aggregate lateral confinement were found to be the two main mechanisms most commonly used to describe the reinforcing properties of geogrids.

The first several studies, where aggregate interlocking and confining were presented as the main reinforcing mechanism of geogrids, did not offer any quantitative data to support this claim; instead, qualitative data was used for this purpose. Walls and Galbreath (1987) attributed the rehabilitation of a railway track, constructed on a weak clayey subgrade, to the capacity of a geogrid layer to interlock and confine the aggregate.

The authors were aware that properly sized geogrids would interlock adequately with the aggregate and provide an optimal performance, which was proven after the railway track remained functional three years after being rehabilitated (Walls and Galbreath, 1987). Hass and Carroll (1987) envisioned the interlocking and confinement effect of the geogrid, by depicting a pyramid made out of aggregate particles whose bottom layer was confined by the ribs of the geogrid and provided resistance to tension. This layer of reinforced aggregate particles allowed other aggregate particles to rest on top of them, interlock with particles around, and create a reinforced pyramid. Had the geogrid ribs not been confining the aggregate particles located at the bottom of the pyramid, the pyramid would have collapse due to its own weight (Hass and Carroll, 1987). Chan et al. (1989) did not have a precise concept of how geogrid reinforced aggregate; however, they believed that the strengthening of the aggregate layer occurred mainly because the aggregate particles were somehow hindered; therefore, a local reinforcement effect was created around the geogrid layer.

As time continued, new studies began exploring the importance of aggregate interlocking and confining, and exploring new methods to test their influence. The studies performed by Webster (1993), in which test sections with and without geogrid reinforcement were studied, provided insight into aggregate interlocking and confinement. Unreinforced test sections exhibited aggregate lateral flow failure at the interface between the aggregate and the subgrade; however, it was observed that for geogrid-reinforced sections, the lateral displacement of the aggregate was constrained, and this failure mode did not occur. This phenomenon was attributed to aggregate interlocking and confining inside the geogrid apertures (Webster, 1993).

This finding was later supported by the assessment performed by Fanning and Sigurdsson (1996) on the migration of fine particles into the reinforced aggregate base layer. This study observed that the migration of fine particles affected the capacity of aggregate particles to interlock with the geogrid and among themselves, which ultimately resulted in undesired performance of the test section (Fanning and Sigurdsson, 1996). This phenomenon was further demonstrated when a road test section, which was reinforced with a geogrid layer over a geotextile layer, and placed at the subgrade/aggregate base layer interface, was tested. The capacity of the geogrid to interlock and confine the aggregate was diminished tremendously by the geotextile, because the aggregate could not punch through the geogrid, which negatively affected the overall performance of the composite system (Hufenus et al., 2006).

Although it was observed that aggregate interlocking and aggregate confining were found to be some of the most important stabilizing mechanisms present in geogrid-reinforced unpaved roads, no research was carried at the time to study their micro-scale behavior and understand the parameters that controlled them, such as aggregate morphology and size compatibility. Instead a macro-scale approach was taken to understand and quantify the way geogrid-reinforced unpaved roads worked.

2.2.6 Design Methodologies

Multiple geogrid design methodologies for reinforcing unpaved roadways were developed after the introduction of geogrids into the market. Early design methodologies were based on data obtained from studies carried out since the late 1980's, and methodologies previously developed for the design and construction of geotextile-reinforced unpaved roadways. A brief summary of the main five design methodologies utilized for geogrid-reinforced paved and unpaved roads is presented next.

2.2.6.1 *Design of Unpaved Roads and Trafficked Areas with Geogrids (Giroud et al., 1985)*

This design methodology established by Giroud, Ah-Line and Bonaparte was developed from the effort of The Tensar Corporation to provide a design methodology for their state-of-the-art geogrids. This design methodology focused on determining the improvement of the performance of an unpaved roadway when this one was reinforced with geogrids, by quantifying the load distribution improvement on the subgrade/aggregate base layer interface.

Limited data from multiple studies at the time was used to develop a numerical elastic analysis capable of quantifying the geogrid/base interlock and describing the behavior of the subgrade, the aggregate base layer, and the geogrid. This approach was undertaken, in order to develop an analytical solution for the problem, which could then be used to generate design charts capable of determining the aggregate base layer thickness required for the optimum performance of these structures.

The main input parameters in this design methodology were the undrained shear strength of the subgrade, the number of passages of an axel load equal to 80kN, and the allowable rutting depth.

The numerical simulations based on elastic analysis were performed in different reinforced and unreinforced unpaved road section models. These models exhibited different failure scenarios, which distributed the vertical stresses to the subgrade/aggregate base layer interface at different angles. This load distribution was idealized as a pyramidal load distribution. Two unreinforced models, and three reinforced

models were studied to develop this method. The ratio between the angles formed by the stress distributions of reinforced and unreinforced cases, known as load distribution improvement ratio, were computed.

The load distribution improvement ratio determined the thickness of the aggregate layer required for geogrid-reinforced unpaved roads. This thickness ratio (R) was calibrated using a specific type of geogrid. For this case, Tensar geogrids SS1 or SS2, were used to calibrate the model. The chart developed by the authors to compute R is presented in Figure 2.1.

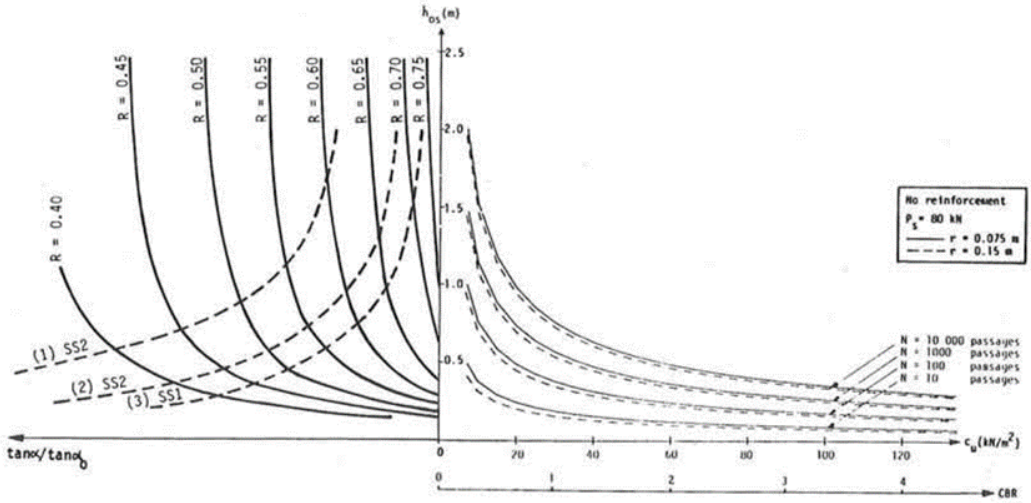

Figure 2.1. Chart for the design of geogrid-reinforced unpaved structures (Giroud et al., 1985)

The Procedure used to determine the aggregate thickness of the geogrid-reinforced aggregate base layer is as follows:

1. Using subgrade undrained shear strength, number of axel passages, and allowable rut depth, the thickness of the aggregate base layer for the unreinforced case was determined.

2. A geogrid type (SS1 or SS2) was selected.

3. The thickness ratio (R) at the intersection between the unreinforced aggregate base layer thickness and the geogrid type was selected, by using the chart in Figure 2.1.

4. The thickness ratio was multiplied by the unreinforced unpaved road thickness to obtain the geogrid-reinforced aggregate thickness.

This design considered the tension membrane effect, by reducing the reinforced aggregate layer thickness by 10%, when the allowable rut depth was greater than 0.15 meters.

2.2.6.2 *Geogrid Reinforcement of granular bases in flexible pavements (Carroll and Haas, 1987)*

The design method developed by Carroll and Haas emerged from their study on geogrid reinforced aggregate base layers in flexible pavements. In this study, the influence of the subgrade strength, the location of the geogrid, and aggregate base thickness was observed. The design methodology focused on modifying the AASHTO design specifications for pavement structures current at the time, in order to include the benefit of utilizing geogrids in the aggregate base layer of flexible pavements. The design of flexible pavements at the time relied on the structural number of each layer within the pavement section to calculate the robustness of the design.

This method set the structural number of the unreinforced and reinforced granular base layers equal to the ratio between the reinforced and unreinforced granular layer coefficients. This ratio expressed the effect of the geogrid on the structural capacity of the granular base layer; therefore, the higher this value was, the higher the layer coefficient of a geogrid-reinforced aggregate base was.

This design methodology pointed out that the layer coefficient ratio was the largest (equal to 2) when the reinforced aggregate base thickness was equal to 100 mm. As this thickness increased to 250 mm, the layer coefficient ratio decreased to 1.5. The authors also found that layer coefficient ratios for aggregate base layers equal or greater than 250 mm increased when the geogrid layer was placed at the midpoint of the aggregate base, instead of at the interface between the subgrade and the aggregate base. A chart calibrated for Tensar SS1 geogrid to determine the equivalent base thickness of the geogrid-reinforced aggregate base layer was developed by the authors and it is presented in Figure 2.2.

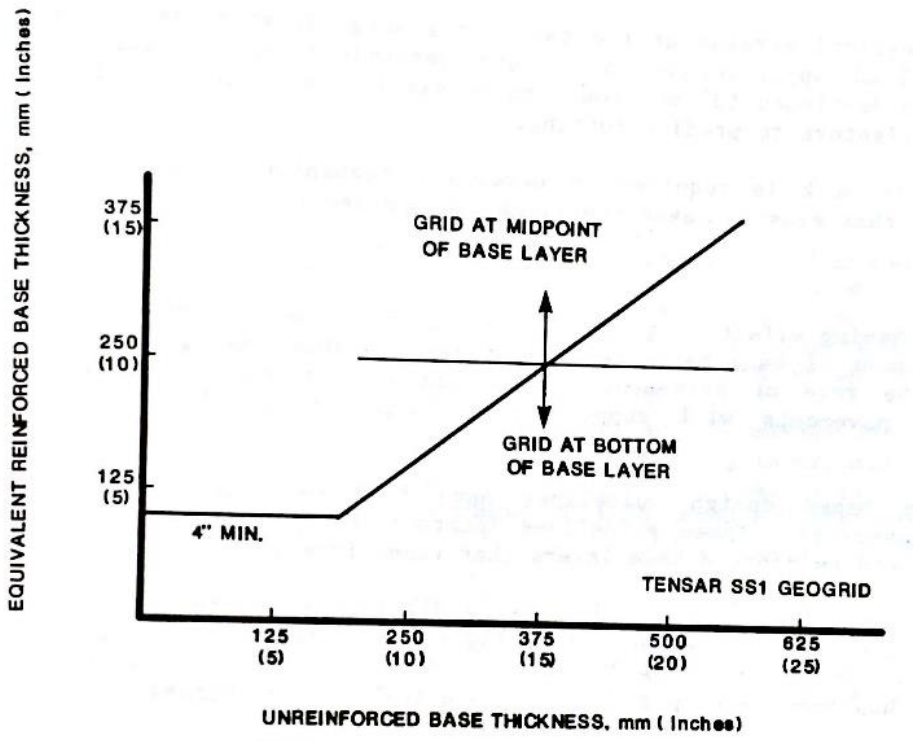

Figure 2.2 Tensar geogrid-reinforced base thickness for flexible pavements (Carroll and Hass, 1987)

2.2.6.3 *A New Approach to the Design of Unpaved Roads (Milligan et al., 1989)*

This approach focused on restraining the shear stresses generated at the interface between the aggregate base layer and the subgrade due to normal loads, which have a detrimental effect on the road. This design methodology deviated from the tension membrane effect concept, since the authors argued that this phenomenon only occured at large deformations that would exceed the allowable surface deformation of the road. Instead, this design methodology focused purely on shear load transfer through the geogrid layer.

This method theorized that shear stresses developed at the surface of the subgrade, due to normal loads applied at the top of the aggregate base layer, were sustained by a layer of geogrid. This geogrid layer became tensioned, and sustained those loads, when the mobilization of shear stress occurred. This assumption allowed the designer to assume that only vertical loads were transmitted to the subgrade.

This methodology calculated the undrained shear strength of the subgrade using the bearing capacity factor Nc from plasticity theory, which the authors related to the ratio between the shear stress under the aggregate base layer ($\pi\tau$), and the undrained shear strength of the subgrade (Su). This ratio was known as the shear strength factor of the unpaved road (αr). The relationship is presented in the diagram shown in Figure 2.3.

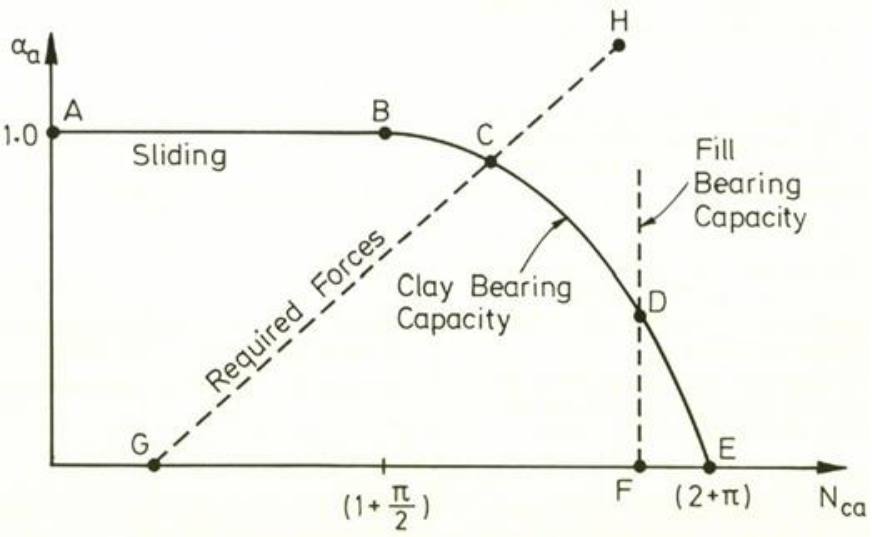

Figure 2.3 Interaction diagram of normal and shear stress for failure of a strip footing (Milligan et al., 1989)

The main objective of this design methodology was to find the Nc value for a specific shear strength ratio, and with this value calculate the maximum allowable traffic load above the aggregate base layer. For unreinforced paved sections, the Nc value changed according to the shear strength factor; however, for geogrid-reinforced unpaved roads, the value was assumed to be zero because the shear stress under the aggregate base layer was assumed to be carried by the geogrid layer. This assumption defaulted the Nc value to 2+π.

The authors recognized that the assumption that the geogrid sustained all the shear stress under the aggregate base layer depended on the surface of the reinforcement being rough enough. Furthermore, they recognize the importance of geogrid stiffness over geogrid tensile strength for roadway applications, due to the necessity of maintaining deformations of the aggregate base layer to a minimum, while being capable of sustaining the shear stresses at the bottom of the aggregate base layer.

2.2.6.4 *Corps of Engineers Design of Geosynthetic-Reinforced Unpaved Roads (Tingle and Webster, 2003)*

The Army Corps of Engineers (COE) developed a methodology for geotextile-reinforced unpaved roads in the early 1990's. This methodology was revised to develop a design methodology capable of designing geotextile and geogrid reinforced unpaved roadways. The army COE approach to design geotextile-reinforced unpaved roads focused on bearing capacity theory of soft undrained soils, due to the fact that often low-volume temporary roads are designed for poor subgrades.

The ultimate bearing capacity of the subgrade was determined by the product between the undrained shear strength (Referred as cohesion C) and the bearing capacity factor, Nc. The undrained shear strength in this method was reported as stress in pounds per square inch, as a California Bearing Ratio (CBR) in percentage, or as a Cone Index in mm per blow. The chart shown in Figure 2.3. was developed with this method to correlate cone index, CBR and shear strength.

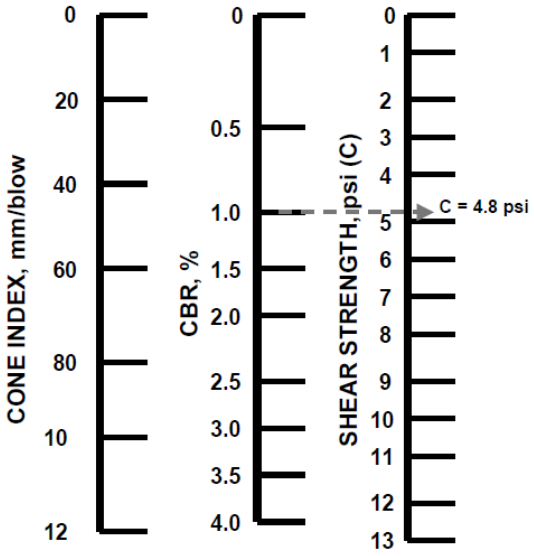

Figure 2.4 Shear strength conversion nomograph from COE design method (Tingle and Webster, 2003).

In foundation design, the bearing capacity factor, Nc, is calculated using plasticity theory and its dependent on the shape of the footing in contact with the soil. This design method assumes that the inclusion of a geosynthetic at the interface between the aggregate base layer and the subgrade modifies the load transfer geometry on the subgrade; therefore, a different Nc value needs to be used.

For the development of this method, an unpaved test roadway with four different sections was trafficked, and the rutting depth and the distortion of the subgrade on each one of these items was recorded. Section 1 was not reinforced, sections 2 and 3 were reinforced with a woven and a nonwoven geotextile respectively, and section 4 was reinforced with a geogrid over a geotextile. After the test was completed, Nc was back calculated for each section, by using the undrained shear strength of the soil, the ultimate bearing capacity of the subgrade, and the rut depth at the surface. The authors found that for the unreinforced, geotextile-reinforced, and geogrid-reinforced unpaved roadways, Nc values equal to 2.8, 3.6, and 5.8 had to be used to compute the subgrade bearing capacity respectively.

2.2.6.5 *Design Method for Geogrid-Reinforced Unpaved Roads (Giroud and Han, 2004)*

Most recently Giroud, with the collaboration of Han, revised the design methodology developed in 1985. This design method, which is the most current one, emphasizes the importance of aggregate-geogrid interlocking for aggregate base layer reinforcement, and points out that this mechanism does not occur when geotextiles are used for reinforcement. This methodology is suitable not only for designing geogrid-reinforced unpaved roads, but also geotextile-reinforced and unreinforced unpaved roadways. For geotextile-reinforced unpaved roads, the contribution of interlocking and in-

plane reinforcement stiffness is ignored, while for unreinforced unpaved roads, these two mechanism and the subgrade bearing capacity improvement is ignored.

This design methodology considers the stress distribution on the subgrade, the shear strength of the base coarse material and its resilient modulus, the interlock mechanism between aggregate and geogrids, and the geosynthetic in-plane stiffness (aperture stability modulus, J) for unpaved road design, while still considering the traffic volume, wheel load, tire pressure, subgrade strength, and rut depth as important parameters for the design.

This design methodology also specifies a minimum aggregate base layer thickness of 10 cm and a subgrade CBR value less than 5%. Differently from previous design methods, the CBR of the aggregate base layer and its resilient modulus is taken into consideration, in order to assess the angle of the pyramidal load distribution on the subgrade.

This method uses the stresses at the subgrade/aggregate base layer interface to determine the rut depth as a function of bearing capacity. The thickness of the aggregate layer depends on the bearing capacity of the subgrade, the number and intensity of the wheel loading, and the vertical stress distribution on the aggregate base. The benefits of using geogrids and the quantification of the aggregate-geogrid interlock are taken into consideration by using the geogrid aperture stability modulus, J, and an Nc value according to the reinforcement type. For unreinforced unpaved roads, the Nc value is equal to 3.14, while for geotextile and geogrid reinforced unpaved roads is 5.14 and 5.71, respectively.

2.2.6.6 *Remarks*

All five design methodologies previously presented take a large-scale approach to investigate and quantify the benefit of reinforcing the aggregate base layer with geogrids. These design methodologies regard the aggregate-geogrid composite as a continuum material that behaves as one structure, but do not emphasize the importance of geogrid-aggregate size compatibility for this assumption to hold true (Giroud et al., 1985; Carroll and Haas, 1987; Milligan et al., 1989; Tingle and Webster, 2003; Giroud and Han, 2004). None of these methodologies adopt a microscale approach to study this size compatibility between the aperture size of the geogrid and the aggregate diameter; even though, most of them recognize that the reinforcement capacity of geogrids is owed to the ability of the aggregate particles to interlock with the geogrid layer (Giroud et al., 1985; Carroll and Haas, 1987; Milligan et al., 1989; Giroud and Han, 2004). Therefore, if particle diameter is not compatible with the geogrid aperture size, interlocking will not occur, and the reinforcement effect of the geogrid layer is lost.

Furthermore, all these design methodologies specify the usage of aggregate materials for the base layer; however, design parameters to take into account the size, angularity, and surface roughness of the aggregate particles, which are fundamental for the optimum mechanical behavior of aggregate materials, are not present in any of them. Examples of this are Giroud et al. (1985) and Milligan et al (1989). For Giroud et al. aggregate base layer thickness reduction is dependent on the angle at which the loads are distributed on the subgrade; however, a design parameter regarding the ability of aggregate particles with higher angularity or surface roughness to change this angle and improve the load distribution on the subgrade is not presented. For Milligan et al., the shear stress under the aggregate base layer is totally sustained by the geogrid layer; however, this assumption is questionable, since the roughness of this layer depends on

the capacity of the aggregate particles to interlock, slip, and rotate. No parameters to take into consideration the morphological properties of the aggregate, and their impact in the toughness of this layer, exist.

2.3 Current studies on geogrid-reinforced granular materials

After the mid 2000's the research approach diverged from understanding the macroscale behavior of geogrid-reinforced unpaved roads, and focused on understanding the mesoscale and microscale behavior of the interaction between aggregate particles and geogrids. The new research approach can be categorized into two main groups: physical experimentation of geogrid reinforced aggregate material, and numerical simulation of the interaction between geogrids and granular materials.

The physical experimentation focused on understanding the importance of the geogrid material and its geometrical properties for optimum performance of geogrid reinforced unpaved roads, and determining the optimum geogrid location. The numerical simulations focused on validating these findings and gaining deeper understanding of the key parameters that influenced optimum geogrid reinforcement, by looking at the microscale response of the system.

2.3.1 Laboratory experimentation

Size compatibility between geogrids and aggregates, understand the importance of aperture geometry for optimal stress distribution on the subgrade, identifying the importance of the stiffness of the geogrid for achieving optimum geogrid reinforcement, and identifying the zone of influence of geogrids within aggregate layers and their optimum location were the main focus of the following studies.

2.3.1.1 *Size compatibility*

Brown et al. (2007) performed a comprehensive study to assess the use of geogrids for railway ballast reinforcement, and one of their main goals of this study was to determine the optimal geogrid aperture size compatible with railway ballast. Brown et al. (2007) found that for ballast with a particle mean size diameter equal to 50 mm, a geogrid layer with an opening size ranging from 60 mm to 80 mm was necessary for optimal compatibility. From these findings the authors concluded that a geogrid aperture size to particle size ratio ranging from 1.4 to 1.6 for railway applications was needed for optimal geogrid/ballast size compatibility. Indraratna et al. (2012), studied this topic as well, but instead of adopting a large scale approach, they focused on the meso scale, by studying the geogrid aperture size and ballast mean diameter compatibility on a large direct shear box apparatus. For this study the authors used a railway ballast with a mean particle diameter equal to 35 mm, and multiple types of geogrid with aperture sizes ranging from 20.8 mm to 88 mm, to perform direct shear test. This study indicated that the optimum geogrid aperture size required to enhance the interface shear strength was found between 1.15 D_{50} and 1.3 D_{50}. Furthermore, the authors concluded that geogrid/ballast interlock only occurs when the ratio between geogrid aperture size and ballast mean diameter ranges from 0.9 D_{50} to 2.5 D_{50}; outside this range, no interlock occurs.

2.3.1.2 *Importance of aperture geometry for optimal stress distribution on the subgrade*

During this time, the geogrid aperture geometry evolved from a square to a triangular opening, with the objective to improve the load distribution on the subgrade. This multiaxial geogrid was named triaxial geogrid. Although this novel geogrid was expected to perform better than its predecessor, due to its capacity to provide resistance at 360^{o}, it was necessary to assess it performance. Abu-Farsakh and Chen (2011) and Abu-Farsakh et al. (2012), compared the load distribution between biaxial and triaxial

geogrids installed in a crushed limestone aggregate layer, using a cyclic plate load, and inside a large triaxial chamber, respectively. The results of both studies concluded that triaxial geogrids outperformed biaxial geogrids in distributing the load on the subgrade; even though, their mechanical properties were similar. Therefore, the load distribution improvement was concluded to come from the triangular shape of triaxial geogrids. Qian et al. (2011 & 2012) assessed the load distribution enhancement of triaxial geogrids and compared the results to the load distribution of unreinforced aggregate base layers. This study concluded that the traffic benefit ratio between unreinforced and reinforced aggregate base layers with triaxial geogrids could increase by a factor of up to 13. This traffic benefit ratio depended on the mechanical properties of the geogrid material. Furthermore, this study concluded that triaxial geogrids reduced the vertical stresses on the subgrade layer and distributed the load more uniformly over the subgrade. Lastly, Qian et al. (2013), also performed large scale triaxial tests on aggregates of uniform size using biaxial and triaxial geogrids. This study yielded similar results as the previous four studies, and concluded that triaxial geogrid produced lower vertical permanent deformations in comparison with biaxial geogrids.

2.3.1.3 *Importance of geogrid stiffness*

One of the main material properties that commonly appears in the literature, and is regarded as the responsible for the better performance of triaxial geogrid, is the stiffness of the geogrid. Higher geogrid tensile modulus, or geogrid stiffness, allows for the development of most of the geogrid strength at relative small deformations (Nazzal, 2007), which would definitively influence the load distribution on the subgrade and the development of vertical permanent deformations (Brown et al, 2007). Qian et al. (2011 & 2012) argue that the load distribution properties of triaxial geogrids increased as the robustness, thickness, and mechanical properties of the geogrid increase. Abu-Farsakh

and Chen (2011) and Abu-Farsakh et al. (2012) also conclude that the tensile modulus of the geogrid controlled the load distribution characteristics of geogrid, and as this one increased, the performance of the aggregate base layer improved as seen in their results. Finally, Brown et al. (2007), investigated this matter more rigorously, and concluded that the relationship between geogrid stiffness and tensile strength was not linear. Since the reinforcing characteristics of the geogrid depend on its stiffness, and not on its tensile strength, increasing the tensile strength of the geogrid to improve its reinforcing capacity is impractical (Brown et al., 2007).

2.3.1.4 *Geogrid zone of influence*

Brown et al. (2007) observed that at higher overburden stress the likelihood of the ballast particles to interlock with the geogrid increased, while under low overburden stresses the geogrid resisted compaction and inhibited interlock. This study observed that this behavior was more pronounced when stiff geogrids were used. Brown et al. (2007) concluded from these observations, and the settlement of the ballast layer after 30,000 cycles, that the optimal geogrid location for reinforcing railway ballast was 50 mm above the sub-ballast layer.

Schuettpelz et al. (2009) studied the influence of the geogrid layer on granular media by observing the increment of the modulus of the aggregate, by using geophysical methods. P-wave velocities of reinforced and unreinforced granular layers were recorded and compared, and it was found that the P-wave velocities increased when geogrids were in place. Since P-wave velocity increases when particles are pushed against each other, this phenomenon indicated that geogrids confined the particles and increased the stiffness of the layer. The study found that at 75 mm from the surface, the stiffness of the aggregate layer increased the most, while surface deformation decreased the most. Furthermore,

geogrid located at 150 mm from the surface did not influence the stiffness of the layer and its reinforcement contribution was negligible. The authors performed FEM simulations of the reinforced layers to observe the shear strain and particle rotation within the aggregate layer to find the zone of influence of the geogrid. They observed that particle rotation surrounding a geogrid layer located 50 mm from the surface was only between 2.5 and 5 degrees, and as soon as this location changed, the particle rotation at shallow depths increased. From these findings, the authors concluded that the zone of influence of geogrids was between 30 mm to 40 mm above and below the geogrids. Furthermore, the study concluded that the zone of influence of the geogrid depended on the geogrid stiffness and the ability of soil to interlock with the geogrid. The authors acknowledged that it was necessary to perform this type of study with different aggregate gradations, because this would cause a change in the influence zone due to the fact that interlocking was controlled by the compatibility between the geogrid and the aggregate. They also recognized that DEM would be a more appropriate method to study this problem instead of FEM.

Indraratna et al. (2013) studied the lateral displacement of ballast in geogrid reinforced layers. For this study a modified cubical triaxial apparatus was used. This apparatus consisted of a wall with five independent movable plates used to record the lateral movement of the specimen under loading. The authors studied the lateral spread of the ballast and the ballast degradation with the layer spread index, which they developed. This index increased as the vertical displacement and particle degradation decreased. The study concluded that the optimum location of the geogrid layer was at 65 mm above the subballast layer, since the lateral spread reduction index was the greatest. The study also concluded that the geogrid influence zone varied from 160 mm (4.6 D50)

to 225 mm (6.45 D50) above and below the geogrid layer depending on the geogrid location.

2.3.2 Numerical simulations using the Discrete Element Method (DEM)

The necessity to observe the micromechanical interactions between geogrids and aggregate led to the implementation of different numerical methods such as the finite element and the discrete element methods. Due to the characteristics of this problem, the Discrete Element Method (DEM) was identified as the most effective method to study this phenomenon. Throughout the last twelve years, a number of studies have focused on understanding the mechanical response of these composite materials, the optimal simulation of particle morphology, and the interaction and size compatibility between geogrids and aggregates. A brief summary of the main findings in each one of these areas is presented next.

2.3.2.1 *Understanding the micromechanical response between geogrids and granular materials*

Konietzky et al. (2004), performed the first 3D DEM simulation to study the interaction between geogrids and aggregate. The main idea of this study was to study the effects of interlocking under static and dynamic loads. The geogrid model used in this study, which consisted of 31,000 parallel bonded spheres, was calibrated using stiffness and strength data obtained from single rib tensile test, single junction test, and in-plane rotation test. The effects of interlocking under static loads were studied by performing pullout test on a box with three different constant surcharge loads, while for the dynamic case, studies were performed via triaxial compression tests on geogrid reinforced particles. This study did not consider particle morphology, and spheres were use throughout the study. From the pullout test, it was observed that the maximum number of

contacts and shear forces develop at the location of the geogrid, which indicated the presence of interlocking. From the triaxial test, it was observed that large force chains were developed at the geogrid location, these extended 10 cm above and below the geogrid, and vertical deformations were significantly reduced in comparison to the unreinforced case. The reductions in vertical displacement were attributed to particle confining provided by the geogrid due to interlocking.

McDowell et al. (2006) presented a more comprehensive study on the interaction between geogrids and aggregates using 3D DEM analysis. This study focused on understanding the behavior of geogrid reinforced railway ballast taking into account particle shape. The authors focused on performing pullout tests on statically loaded particles on a large box. These particles were modeled as two-sphere clumps to study the influence of particle shape on particle-geogrid interlocking. The results from this study showed the importance of simulating particle shape, in order to achieve agreement between physical testing and numerical simulations; however, this agreement was only observed for low confining stresses. The explanation for this phenomena was that at high stresses particle crushing occurred; however, this study did not considered particle crushing in their model. The study was able to observe interlocking between ballast and geogrids using DEM, and it concluded that even though interlocking was observed, its response was delayed due to the roundness of the clump; therefore, modeling the angularity of the particles was found to be critical for a satisfactory response.

Tutumluer et al. (2010) used DEM to assess the importance of aggregate morphology in geogrid-aggregate interlocking. The modeling of the particles was performed using the angularity index (AI), flat and elongation (FE) ratio, and surface texture (ST) index obtained from image analysis using the University of Illinois Aggregate

Image Analyzer (UIAIA), and a DEM software capable of simulating particles as polyhedrons called BLOKS3D. Direct shear tests were performed on unreinforced and geogrid reinforced aggregate specimens. The study concluded that geogrids increase the shear strength of the aggregate by providing confinement and constraining the movement of the particles. Furthermore, the authors argue that image analysis aided DEM model has a potential to quantify the individual effects that affect optimum aggregate/aperture size ratio. Although this study puts a lot of effort into modeling aggregate particles as close as possible to their physical counterparts, the geogrid is modeled as a rigid element, which cannot represent the real behavior of geogrids.

Ferellec and McDowell (2012) continued with the study of geogrid reinforced ballast performed by McDowell et al. (2006). This time the authors focused on the importance of modeling the shape of ballast particles, in order to obtain agreeable results with physical experimentation. Ballast particles were modeled using clumps of 55 spheres. Geogrid pullout test were performed using these type of clumps, and it was observed that the contact forces surrounding the geogrid were much higher with respect to pullout test performed implementing spheres only. This study also focused on developing a more accurate geogrid model, by using multiple layers of bonded spheres to create its geometry. These additional layers allowed the geogrid to exhibit a deformation, which agreed more closely to the deformation of real geogrids. Furthermore, the geogrid model was calibrated using data obtained from single rib extension and aperture rotation tests on geogrids. Although the ballast particles and the geogrid were meticulously modeled, the author concluded that the increment of pullout forces was not as pronounced as the results from physical experimentation. The reason for this phenomena was still attributed to the roundness of the clump, which was concluded by McDowell et al. (2006).

Stahl, et al. (2014) develop a more geometrically-simplistic geogrid model to study the interaction between geogrids and aggregate particles with different gradations. The geogrid was developed by bonding chains of spheres of slightly different diameters. This model was calibrated using single rib tensile tests, geogrid junction strength and aperture stability similarly to Konietzky et al. (2004). The aggregate particles were modeled using clumps, and were calibrated against the size and sphericity index of sub-rounded aggregate particles. This geogrid model was calibrated by performing geogrid pullout test; however, the results from the model did not exactly match the results from physical experimentation. The authors argued that the random nature of particle packing was the cause of this behavior. This study concluded that the maximum pullout stresses observed were very small compare to the maximum possible tensile strength of the geogrid; therefore, since the geogrid did not develop large strains, geogrid stiffness was more critical than geogrid tensile strength for reinforcement purposes. Furthermore, pullout resistance depends mainly on the effect of soil particle interlocking with the transverse ribs. This is not the case for other studies, which could suggest that usage of sub-rounded particles induced this type of behavior.

Ngo et al. (2014) studied the behavior of geogrid stabilized ballast with the presence of fouled coal, in order to investigate the impact of the small particles of fouled coal in the reinforcement effect of geogrids. To do this, a mixture of clumps, which represented ballast particles, and small spheres, which represented the fouled coal, were used to perform a DEM simulation of direct shear test on geogrid reinforced ballast. According to the authors a reasonable agreement between physical experimentation and DEM simulations of direct shear tests of geogrid reinforced coal fouled ballast exist; however, at horizontal displacements between 15 mm and 30 mm, discrepancies on stress-displacement curves occur. The authors associated these discrepancies with

particle crushing, which was not taken into account for this study. McDowell et al. (2006) and Ferellec and McDowell (2012) experienced a similar behavior on their geogrid pullout test, but these studies related this behavior to clump roundness. This study concluded that smaller particles reduced the capacity of the larger clumps to interlock with geogrid, because the smaller particles clogged the geogrid-ballast interface. Geogrid/ballast interlocking was measured by quantifying the amount of straining of the geogrid. The geogrid strained 0.4% less in the case where the presence of small particles existed than in the case were only ballast particles were used.

More recently Jas et al. (2015) compared the behavior between multiaxial and biaxial geogrids on unpaved roads using DEM. The modeling of both geogrids and aggregate clumps followed the approach presented by Stahl, et al. (2014). The study focused on studying unpaved roads modeling a weak subgrade with low stiffness particles, and using clumps of different sizes to simulate the aggregate. A cylindrical wall that acted as a wheel was used as the loading mechanism in this study. Although, this was a clever approach, it was not very computationally efficient, since several months were required to model ten passes of this wheel. This study found that the application of the wheel load caused the junctions of biaxial geogrids to rotate and transmit forces and moments to the ribs outside the loaded area; however, multiaxial geogrids confined the particles and created a circular load distribution. This underscored the ability of multiaxial geogrids to distribute loads more efficiently. This study also showed that geogrids presented tension under the wheel load and compression outside that area. Furthermore, they observed that forces on the geogrids did not surpass 0.7 kN/m for biaxial and 0.3 kN/m for multiaxial, and strains were on the order of 0.5%; therefore, this study provided sufficient evidence to validate the claim of multiple physical studies that concluded that geogrid stiffness is the most critical parameter to obtain the least amount of vertical permanent deformations.

(Brown et al, 2007; Qian et al., 2011 & 2012; Abu-Farsakh and Chen, 2011; Abu-Farsakh et al., 2012)

2.3.2.2 *Optimal simulation of particle morphology*

The necessity to model particle morphology accurately to obtain meaningful results was recognized since the introduction of DEM; therefore, multiple studies have only focused on finding the best approach to do this.

Jensen et al. (1999) focused on clustering disks on 2D DEM simulations, in order to model particles capable of interlocking among themselves. This study observed that by clustering individual particles, the particle rotation was significantly reduced; therefore, the shear strength of the specimen increased. This approach was identified to be ideal for modeling angular sands. Shamsi and Mirghasemi (2012) investigated the influenced of particle clumping as well, but their study was performed using 3D DEM simulations. Angular, sub-angular, rounded, and spherical particles were used in this study. DEM triaxial compression test simulations were performed using specimens consisting of multiple clumps of different angularities and surface roughness. The study concluded that as clump angularity and surface roughness increased, the mobilized friction angle increased. Furthermore, the study found that the augmentation of these two morphological properties increased the shear strength and dilation of the specimen. Zhou et al. (2013) performed similar DEM simulations, but instead of using spheres to model the particles and their morphological properties, polyhedrons were used. The angularity of these polyhedrons was modified by increasing or decreasing the amount of vertices that formed the particle. DEM triaxial compression simulations were performed using polyhedrons with different angularity, friction coefficient, and aspect ratio. The study determined that peak

and residual strength of the specimen increased as the aspect ratio of the particles and their friction coefficient increased.

These findings were also observed in different studies, which focused mainly on developing efficient and accurate methodologies for clumping spheres to obtain realistic particle behavior.

Lu and McDowell (2007), used DEM to simulate railway ballast and compared the differences in the results obtained from implemented spherical particles versus clumps as ballast. The roundness of the particle was taken into consideration in this study to observe the impact of multiple particles with different angularities on the response of the test. It was observed that clumps provided a realistic load-deformation response, because these particles were able to interlock and hinder particle rotation. This study observed that although clumps provided a more realistic response, the density of the clumps was affected by the individual particles that comprised the clump; therefore, errors in the particle inertia were identified.

Ferellec and McDowell (2010) developed a method to model ballast realistically in DEM, by using a surface of points obtained from scanning a real ballast particle. This surface was populated with a specific amount of spheres depending on the desired particle resolution; however, the efficiency of the model decrease as the amount of spheres per clump increased. The particle overlap within the clump generated inaccurate mass distribution within the clump, and thus incorrect moments of inertia. The authors found that by maintaining the mass of the spheres equal, the mass distribution within the clump remained constant, and incorrect moments of inertia were avoided.

Chen et al. (2012) focused on understanding the force distribution on different aggregate gradations and finding the dominant particle size in the aggregate structure that carried the most forces. Clumps were modeled using the approach from Lu and McDowell (2007) and their size ranged from 0.075 mm to 16 mm. The authors found that large particles tended to carry the largest contact forces because they had the largest amount of contacts. They also concluded that the addition of smaller clumps reduced the amount of air voids, increased the contacts per particle, and decreased the amount of forces taken by the large particles; however, the bigger particles continued transferring most of the contact forces.

Chen et al. (2013) continued to study the importance of aperture shape for geogrid-reinforced ballast. This time the focus was shifted back to geogrid pullout tests under static loads. The geogrid and ballast models remained the same as Chen et al. (2012). Their study was able to determine that geogrids with triangular apertures outperformed geogrids with square apertures, by providing more particle confinement and geogrid ballast interaction. Furthermore, it was observed that aperture geometry was more influential than rib cross-sectional shape and junction profile for optimum interaction between geogrids and ballast.

Xiao et al. (2014) investigated the simulation of unbounded aggregate materials in DEM with polyhedron particles, which were modeled using morphological parameters obtained from image analysis. Six different types of aggregate gradations and twenty-one different blends of the same gradation, but different amount of crushed particles were used. Triaxial compression test data from physical experimentation was used to calibrate the DEM model. The results from these triaxial simulations were successful in reproducing the shear strength behavior observed in the physical experimentation. The author

concluded that image analysis aided DEM simulations had potential to be used as a tool to optimize the selection of aggregate for different transportation applications.

Finally, Chen et al. (2014) continued their work to obtain a realistic interaction response between geogrids and aggregates. In order to do that, four clumps with the number of spheres ranging from 2 to 8 were used to evaluate pullout forces and assess geogrid-clump interlocking. Some of these clumps contained the same number of spheres, but their arrangement was modified to simulate rounded and flaky particles. The angle of repose of these particles was representative of the angle of repose of the ballast, which was used to characterize the benefit of angularity among the four particles. It was observed that out of all four particles, the 8-sphered clump with smaller spheres on its outside, seemed to be the most represented clump of real ballast particles. The smaller spheres around the clump were effective for modeling the particles' angularity. The study concluded that accurate representation of angularity and surface texture is key to develop a model response that closely represents the behavior of real ballast particles.

2.3.2.3 *Interaction and size compatibility between geogrids and granular materials*

Multiple studies focused on obtaining the optimum geogrid/particle interaction and characterizing the zone of influence of geogrids.

McDowell et al. (2006) observed that aggregate-geogrid optimum size compatibility occurred at a geogrid aperture to aggregate mean size ratio equal to 1.4, after performing pullout test on geogrids with different aperture sizes, while maintaining the aggregate size constant. Qian et al. (2011) continued to use the modeling approach presented by Tutumluer et al. (2010), and studied the optimum geogrid apertures size for railway ballast by performing cyclic load tests on geogrid reinforced ballast. Their study

focused on the physical laboratory results obtained by Brown et al (2007). Due to the complexity of the model only 40 loading and unloading cycles were modeled, and the vertical deformations of the specimen were observed. The authors concluded that for a 65 mm geogrid aperture size, the most optimal interaction was achieved with a ballast particle with a mean size equal to 40 mm, which is equal to a geogrid aperture to aggregate size ratio of 1.625. The results of the simulations agreed with the results presented by Brown et al. (2007).

Konietzky et al. (2004), placed three layers of geogrid, spaced 15 cm apart from each other, inside a model of a triaxial chamber. The authors observed from these simulations that the contact forces developed in the chamber extended from the geogrid towards the following geogrid layer. This zone of influence was measured to extend 10 cm above and below each geogrid layer. The development of this zone of influence was attributed to particle interlocking above and below the geogrid. Chen et al. (2012), used the approach developed by McDowell et al. (2006) and Ferellec and McDowell (2012) to model ballast and geogrids, in order to study the physical results obtained by Brown et al. (2007) as well. For their study confined and unconfined tests were performed. The confined test consisted of loading confined clumps by a railway sleeper on a large box, while the unconfined tests consisted of loading unconfined clumps with a railway sleeper also on an apparatus developed by Brown et al. (2007) known as the Composite Element Test (CET). This study concluded that the optimal geogrid location depended on the confining state of the ballast, since the optimal geogrid location was determined to be 100 mm and 50 mm from the base for the confined and the unconfined cases, respectively. Lastly, the authors concluded that geogrid aperture shape is a key parameter to determine the optimal performance of geogrids. Triangular apertures were found to provide more reinforcement benefit than square apertures, by observing the vertical deformation

obtained with each type of geogrid, while maintaining the micromechanical parameters of both specimens equal. Lastly, Chen et al. (2014) concluded that the reinforcement zone of geogrid reinforced ballast lies approximately 75 mm above and below the geogrid, after performing pullout test under static loads, while modifying the angularity of the clumps representing railway ballast.

2.4 Closing thoughts

Although the studies previously presented have focused on specific topics imperative for the understanding of geogrid reinforcement of granular materials for transportation applications, such as aggregate and ballast, the large majority of these studies lack geogrid/particle gradation considerations. It is clear that geogrids alone, cannot deliver their reinforcing effect unless they achieve an optimum interlock with granular materials. In order to obtain this optimum reinforcing capacity, optimum aggregate gradation, particle angularity and surface roughness, needs to be determined. This study will the focus on these considerations for three different types of multiaxial geogrids: TX130S, TX140 and TX190L.

CHAPTER III: STUDY, QUANTIFICATION, AND MODELING OF AGGREGATE MORPHOLOGY

3.1 Intoduction

Aggregate is a granular material, which consist of multiple individual particles that have different sizes, shapes and, textures. These morphological properties are classified in three categories known as form, roundness, and surface texture (Barrett, 1980), and describe the eccentricity or platiness, angularity, and roughness of a particle respectively. The macroscale behavior of this material, such as its shear strength and tendency to permanently deform under compressive loads, depends on the microscale interaction between its particles (Cho 2006; Kwon et al, 2015). These microscale interactions are inherently dependent on particle morphology, due to the fact that eccentricity, angularity, and roughness hinder particle rotation, slippage, and rearrangement, and induce particle interlocking (Cho et al, 2006; Guo and Su, 2006). Therefore, to fully understand the behavior and interaction between aggregate and other geomaterials, such as geogrids, aggregate needs to be studied as a discrete granular material, taking into consideration its morphological properties, instead of a continuum material, which is the common approach.

Due to the fact that laboratory experimentation cannot provide complete insights regarding the microscale interaction between aggregate particles, and the influence of their morphological properties, it is necessary to implement a numerical method capable of doing this. The discrete element method (DEM), proposed by Cundall and Strack (1979), is the ideal approach to study these microscale interactions, because it has the

capacity to replicate particle movement, determine interparticle contact forces, replicate and modify aggregate morphological properties, and isolate the contribution of each one of these, by using Newton's laws of motion and contact mechanics

The commercial code Particle Flow Code 3D (PFC3D), developed by Itasca and initially released in 1994, is a software capable of implementing DEM, and it is widely used to model the behavior of granular materials. This software uses two main components denominated walls and spheres, which can be used to create multiple scenarios for coarse soil and rock testing. Walls are used to simulate containers or boundaries, while spheres are used to simulate soil particles. Overlapping of multiple spheres to create complex shaped elements, known as clumps, is possible in this software as well. Clumps are useful elements that allow the investigation of the influence of particle angularity and eccentricity, which is impossible to do with the implementation of smooth spheres. Furthermore, the contact behavior between the different elements can be modified to investigate different contact scenarios.

In order to accurately simulate aggregate particles with their actual morphological properties in PFC3D, it is necessary to quantify them, and develop a method to specify them in the model. Multiple studies have been carried out in the past with the purpose of quantifying these parameters, by performing image analysis on the projection of the particle. Some of these analyses have focused on performing computational geometry on two-dimensional (2D) projections of the particle, to mimic classical techniques of quantifying aggregate morphology, and measure sphericity, surface roughness, and roundness by this method (Zheng and Hryciw, 2015); some others have focused on defining new parameters based on the difference between the outline of a circle and the particle's 2D projection, as well as the number of corners and their sharpness, to quantify

the shape and angularity (Sukumaran and Ashmawy, 2001). More rigorous studies have focused on conducting three-dimensional (3D) image analysis on two orthogonal images of the same aggregate particle to determine the longest, intermediate, and shortest dimensions of both projections and quantify the elongation, flatness, sphericity, and roundness of the particle (Kuo et al., 1996). This 3D approach allows an analysis capable of better characterizing the morphological properties of the overall particle, instead of just one of its projections.

Most recently the University of Illinois developed an aggregate image analyzer capable of quantifying the eccentricity, angularity, and roughness of a particle. The University of Illinois Aggregate Image Analyzer (UIAIA) captures three orthogonal images of each aggregate particle, converts them into a binary image (black and white), and performs three different calculations on each one of them to compute the Flat and Elongation (FE) ratio, the Angularity Index (AI) and the Surface Texture (ST) Index. The FE Ratio provides an index value capable of describing the particle's eccentricity, the AI provides an index value capable of describing the particle's angularity, and the ST Index provides an index value capable to describe the surface roughness of the particle. The procedure to determine the FE Ratio, AI, and ST Index, and the mathematical reasoning behind them, is discussed in detail in Rao et al., (2001), Rao et al., (2002), and Pan and Tutumluer (2006), respectively. The UIAIA is used to study and quantify the morphological properties of aggregate locally available in the State of Georgia, and the mathematical reasoning used to calculate these values, is used to model the aggregate particles utilized throughout this study.

3.2 Image analysis of aggregate particles

3.2.1 Geographical location and mineralogy of aggregate

In order to have a notion of the morphological properties of the aggregate locally available, aggregate samples from four different quarries across the State of Georgia were collected. A geological map of the State of Georgia displaying the locations of the four quarries from which aggregate was obtained, are presented in Figure 3.1.

These four quarries are found in different locations within the Piedmont and Appalachian Plateau regions, and they exhibit a slightly different mineralogy. Table 3.1 summarizes the mineralogy of the four different types of aggregate used in this study, and their group reference number assigned by the Georgia Department of Transportation (GDOT).

Table 3.1 Mineralogy and aggregate reference group of aggregate samples used in the study (GDOT, 2016).

Source Location	Mineralogy	Aggregate Group
Dalton	Limestone	I
Hitchcock	Mylonitic Gneiss/Amphibolite	II
Norcross	Granite Gneiss/Amphibolite Gneiss	II
Walton County	Biotite Gneiss	II

A specimen from each aggregate sample was collected and sieved through sieves with opening sizes ranging from 50.8 mm (2 in) to 6.33 mm (1/4 in). Aggregate particles retained in the 25.4 mm (1 in), 19 mm (3/4 in.) and 10 mm (3/8 in.) sieves were selected to undergo image analysis and quantify the morphological properties of these four types

of aggregate. Figure 3.2 presents aggregate particles retained in the 25.4 mm sieve from each aggregate specimen.

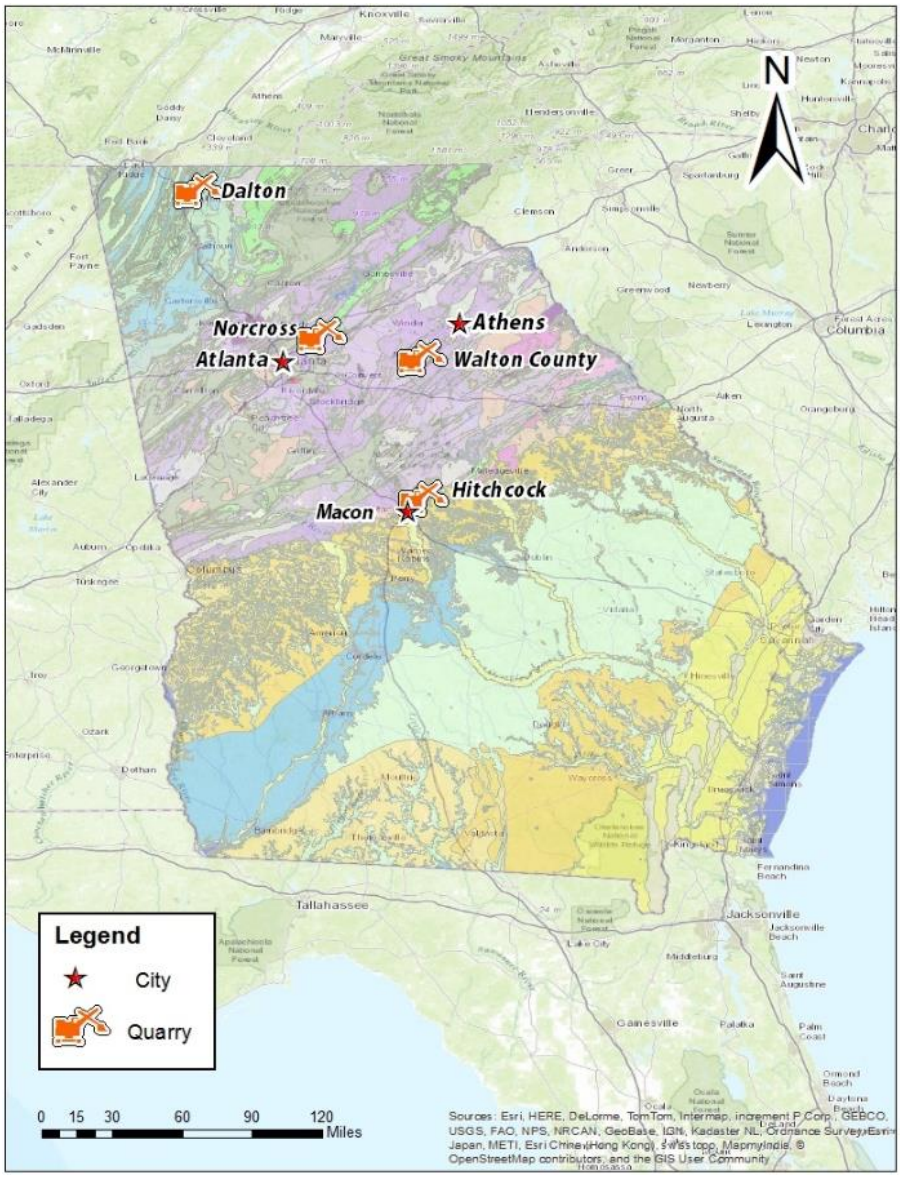

Figure 3.1 Geological map of the State of Georgia displaying the location of the different quarries (USGS, 2005).

Dalton Specimen

Hitchcock Specimen

Norcross Specimen

Walton County Specimen

Figure 3.2 Aggregate particles retained in the 25.4 mm sieve from each aggregate specimen.

3.2.2 Image analysis of aggregate using the University of Illinois Aggregate Image Analyzer (UIAIA)

The image analysis of the aggregate specimens was conducted on multiple aggregate particles of each specimen. Each aggregate particle was placed on the conveyor belt of the UIAIA and passed in front of three cameras positioned at 90^{o} from each other, to capture images of their front, side, and top faces. Figure 3.3 shows the UIAIA in the process of capturing the images of the aggregate particles, and Figure 3.4 presents example images captured by the UIAIA and their binary image representation.

The Angularity Index (AI), and the Flat and Elongated (FE) Ratio of each specimen were determined by performing image analysis on particles retained in the 25.4 mm, 19 mm and 10 mm sieves. The Surface Texture (ST) Index of each specimen was determined by performing image analysis on particles retained in the 25.4 mm sieve. The values obtained for AI, FE Ratio, and ST Index for each aggregate particle of each specimen are displayed in Figure 3.5, Figure 3.6 and Figure 3.7, respectively.

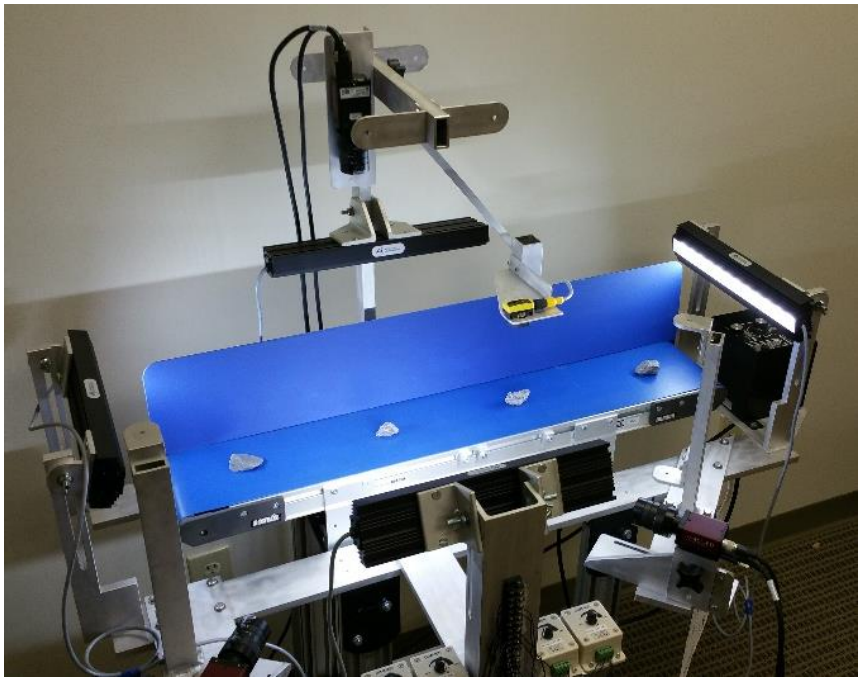

Figure 3.3 UIAIA capturing the images of each particle to quantify their morphological properties.

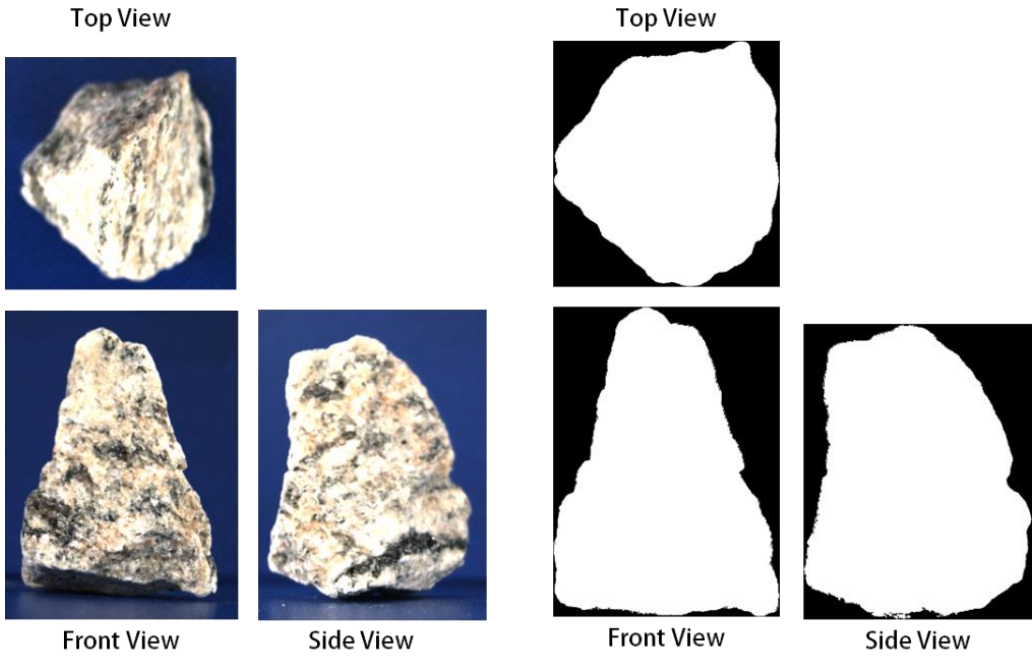

Figure 3.4 Set of images captured by the UIAIA, and their respective binary images

Figure 3.5 displays the AI values of the aggregate particles in each specimen. From this figure it is evident that the AI of these particles varies significantly within each specimen; however, this variation is not dependent on the size of the aggregate particle. The coefficient of variation of the AI for particles retained in the 25.4 mm, 19 mm, and 10 mm sieves ranges from 18.5% to 24.3%, 17.4% to 20.4%, and 18.4% to 22.2% respectively across all four specimens. The overall coefficient of variation of the AI for the Dalton, Hitchcock, Norcross, and Walton County specimens is 20.2%, 22.4%, 23.7% and 23.7%, respectively. Another characteristic noticeable in the analysis is that as the size of the aggregate particle increases, the AI decreases for all the specimens except for the Dalton specimen. This phenomenon could be attributed either to the smaller particles becoming more angular than the larger ones during the crushing process at the quarry, or that as the aggregate particle size is reduced, the accuracy of the UIAIA decreases and the AI is overestimated. The average AI for the aggregate specimens obtained from Dalton, Hitchcock, Norcross, and Walton County specimens are 443, 494, 551, and 446 degrees respectively.

Figure 3.6 displays the FE ratio values of the aggregate particles in each specimen. From this figure it is apparent that the FE ratio of the particles within each specimen vary significantly; however, just like in the case of the AI, the variation is not dependent on the size of the particle. The coefficient of variation of the FE Ratio for particles retained in the 25.4 mm, 19 mm, and 10 mm sieves ranges from 24.6% to 31.5, 20.2% to 32.9%, and 25.6% to 32.0% respectively across all four specimens. The overall coefficient of variation of the FE ratio for the Dalton, Hitchcock, Norcross, and Walton County specimens are 17.9%, 27.7%, 24.7% and 30.1% respectively. The FE ratio of the particles appear to remain constant as the particle size decreases. The average FE Ratio

for the aggregate specimens obtained from Dalton, Hitchcock, Norcross, and Walton County specimens are 2.8, 3.1, 2.4, and 2.4, respectively.

Figure 3.7 presents the ST Index values of the aggregate particles in each specimen. Aggregate particles retained in the 25.4 mm sieve were used to study the ST index of each of the aggregate specimens. The purpose behind this was to obtain reliable ST Index values, since it was observed in previous analysis that as the particle size decreased, the ST index variation tremendously increased and the values obtained showed an unrealistic surface roughness. The overall coefficient of variation of the ST Index for the Dalton, Hitchcock, Norcross, and Walton County specimens are 28.2%, 43.0%, 23.0%, and 25.8% respectively. The average ST Index for the Dalton, Hitchcock, Norcross, and Walton County specimens are 2.8, 3.1, 2.4, and 2.4 respectively.

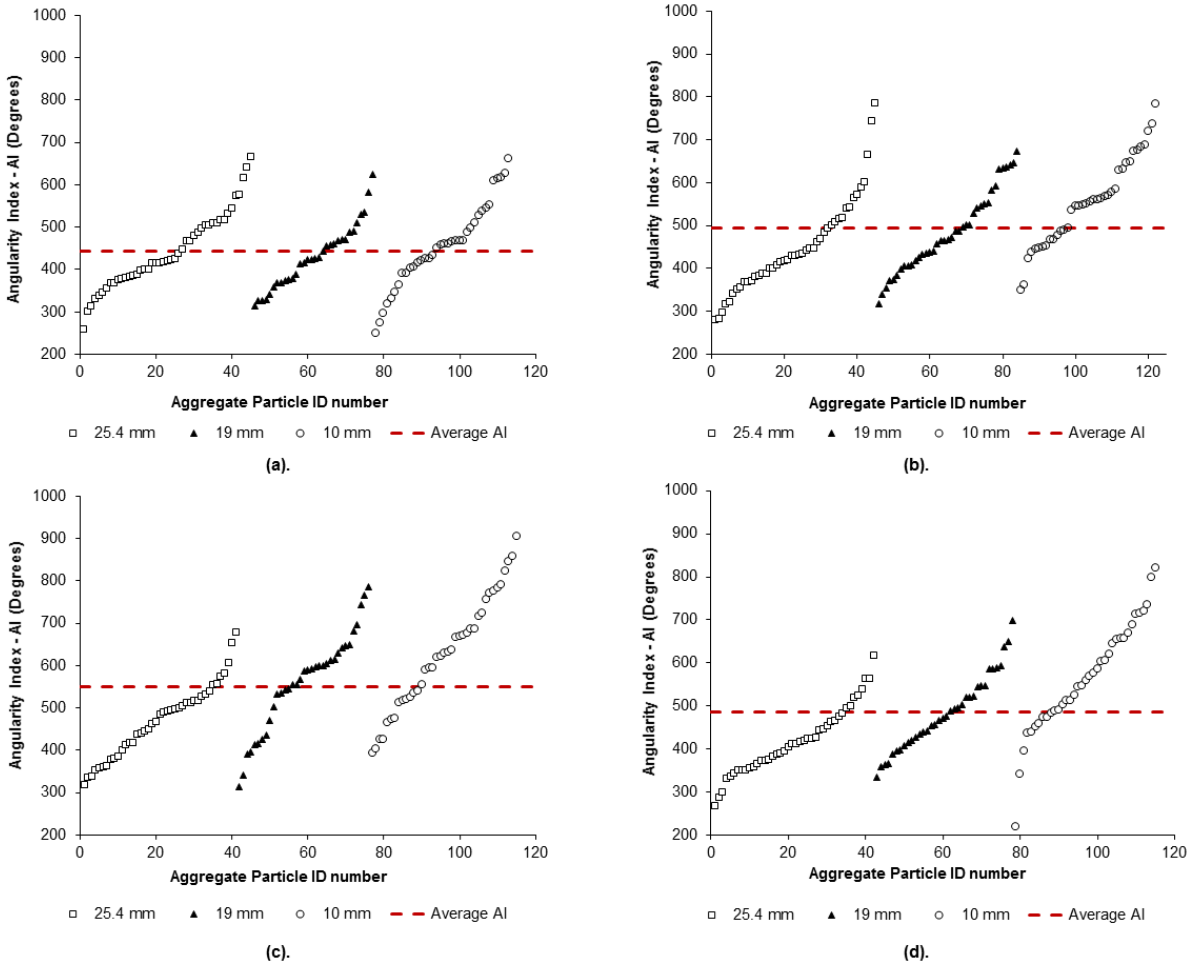

Figure 3.5 Angularity Index results for each aggregate particle in each aggregate specimen from (a). Dalton, (b). Hitchcock, (c). Norcross, and (d). Walton Co. quarries

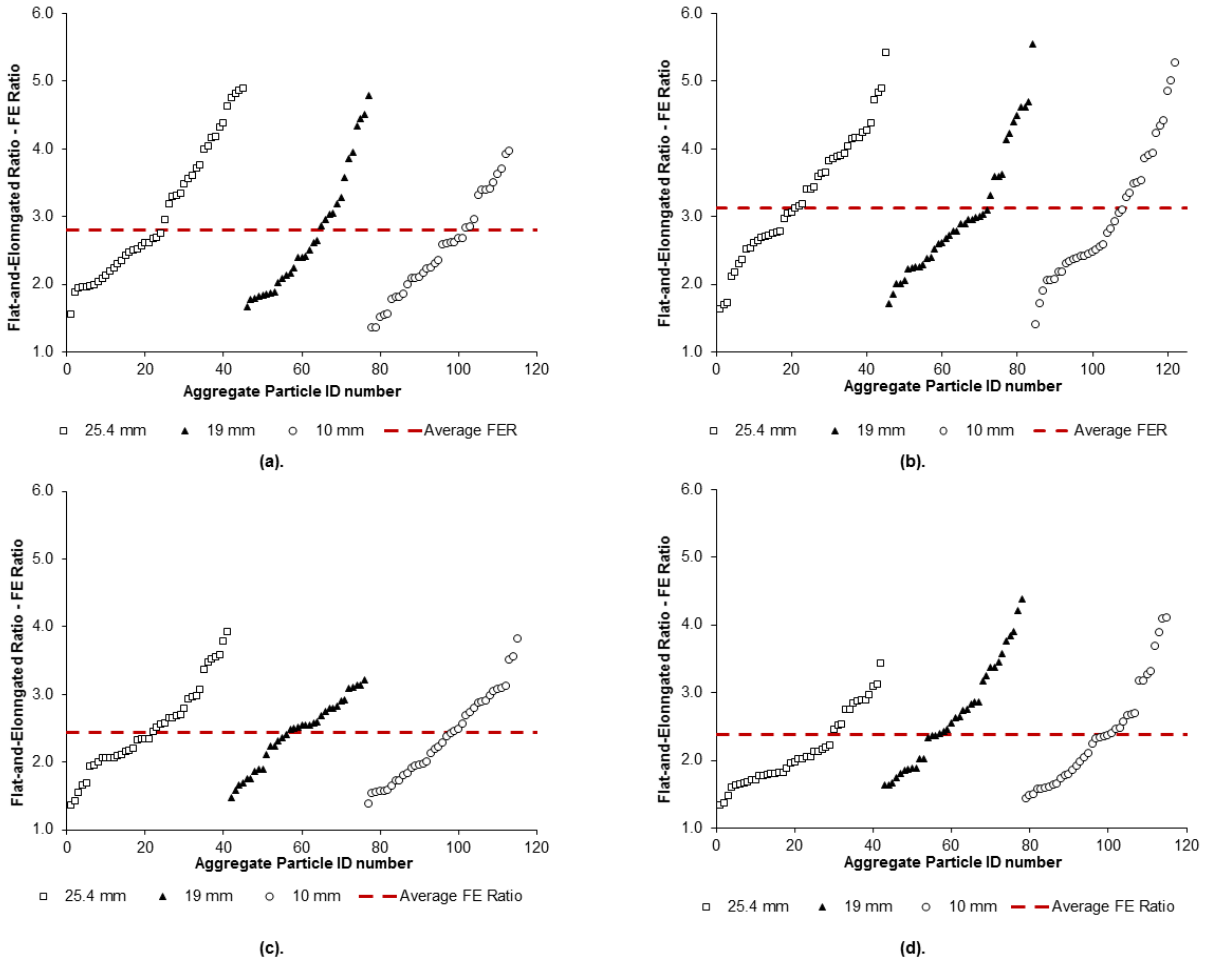

Figure 3.6 Flat and Elongated Ratio results for each aggregate particle in each aggregate specimen from (a). Dalton, (b). Hitchcock, (c). Norcross, and (d). Walton Co. quarries

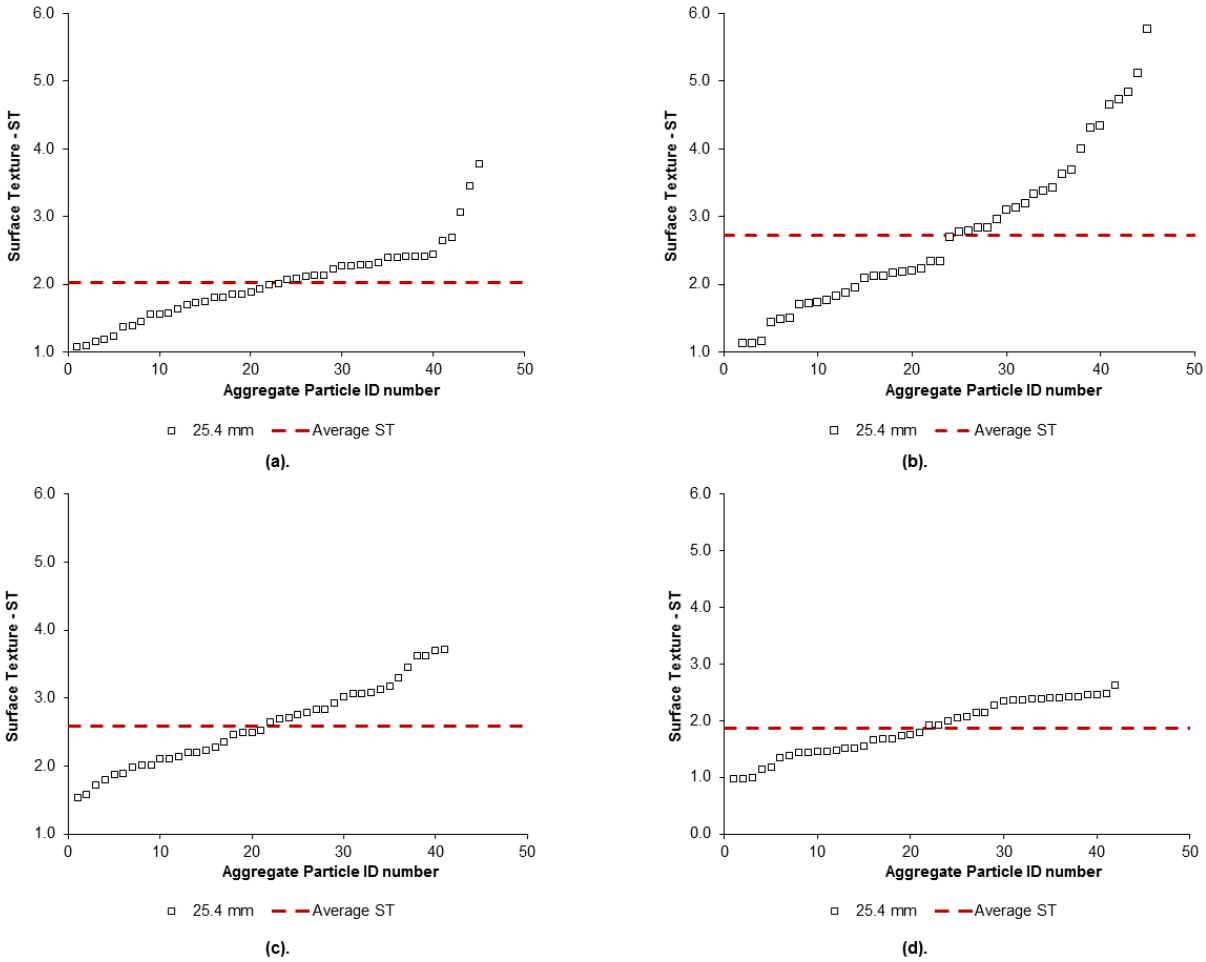

Figure 3.7 Surface Texture index results for each aggregate particle in each aggregate specimen from (a). Dalton, (b). Hitchcock, (c). Norcross, and (d). Walton Co. quarries

A summary of the image analysis results obtained from the four different aggregate specimens is presented in Table 3.2 and Table 3.3.

Table 3.2 Average AI and FE Ratio values of the different aggregate specimens.

Site	No. Aggregate Particles	Angularity Index (Degrees)			FE Ratio (mm/mm)		
		Average	σ	COV	Average	σ	COV
Dalton	113	443	90	20.2%	2.8	0.50	17.9%
Hitchcock	122	494	111	22.4%	3.1	0.93	29.7%
Norcross	115	551	130	23.7%	2.4	0.60	24.7%
Walton	115	486	115	23.7%	2.4	0.72	30.1%

Table 3.3 Average ST Index and FE ratio of four different aggregate specimens

Site	No. Aggregate Particles	Surface Texture (ST)		
		Average	σ	COV
Dalton	45	2.0	0.57	28.2%
Hitchcock	45	2.7	1.17	43.0%
Norcross	41	2.6	0.60	23.0%
Walton	42	0.9	0.48	25.8%

The quantification of the morphological properties of these aggregate specimens is fundamental to achieve a representative Discrete Element Method (DEM) model, which closely simulates the actual aggregate behavior. These, now quantified, parameters are the main framework to develop discrete elements, which are capable of doing so, and are explained in the next section.

3.3 DEM modeling of aggregate particles

3.3.1 Quantification of the AI, FE Ratio, and ST Index by the UIAIA

In order to study the influence of aggregate morphology on the stabilizing capabilities of multiaxial geogrids using DEM, discrete elements that exhibit the same angularity, surface roughness, and size of the actual aggregate particles needed to be modeled. This objective can be achieved by using the AI, FE Ratio, and ST Index results obtained in the previous section; however, in order to effectively apply these parameters to the aggregate model, it is necessary to understand the logic used by the UIAIA to quantify them.

The AI of aggregate particles is determined in the following fashion:

- Orthogonal images from the front, side, and top of the aggregate particle are captured.
- These three color images are converted into binary images, in order facilitate the identification of the particle outline.
- The outline of each binary image is traced with a 24-sided polygon of equal side length.
- The angles at the vertices (α) of these twenty-four lines are computed.
- The relative change in angel at each vertex (β) is calculated by computing the difference between the current and subsequent vertex angle α. This value is always positive.
- A frequency distribution of the β values is defined in 10^0 intervals from 0-10 to 170-180.
- The angularity (A) of each side of the particle is computed by using the formula

$$A = \sum_{e=0}^{170} e \cdot P(e)$$

where e = 0, 10, 20, 30… 170 for class intervals equal to 0-10, 10-20, 20-30… 170-180, and P(e) is the probability that β has a value in the range of e to e+10.

- The AI is determined by computing the weighted average of the angularity of each image with respect to their areas.

Rao et al., (2002) explain the complete procedure used by the UIAIA to quantify the Angularity Index of aggregate particles in detail. A simplified step-by-step procedure showing the AI calculation of the triangular face of a particle with the shape do a pyramid is presented in Appendix A.

The FE Ratio is calculated by taking the binary images of the three orthogonal faces of the aggregate particle and determining the longest segment of a particle. After the longest segment is found, the dimension that is perpendicular to this one is computed. The six dimensions recorded (two from each side) are sorted, and the maximum and minimum dimensions are determined. Finally, the FE Ratio is determined by the ratio between the maximum to the minimum dimension. Rao et al., (2001) explain the complete procedure used by the UIAIA to determine the FE Ratio in detail.

Lastly, the ST Index is determined by performing an image processing technique called erosion and dilation. This technique adds pixels to the boundary of the aggregate particle on a binary image by dilation, and removes pixels from this boundary by erosion. These two process increase and decrease the area of the aggregate particle in the image, and this process occurs for a specific number of cycles. The percent change in area of pixels on each image is computed. The ST Index is finally determined by calculating the weighted average of the surface texture calculated on each image with respect to particle

image area on each image. Pan and Tutumluer (2005) explain the complete procedure used by the UIAIA to compute the ST Index.

3.3.2 DEM Modeling of Aggregate Particles

3.3.2.1 *Clumps Properties Used for Modeling of Aggregate Morphology*

The next step to model aggregate particles with their morphological properties is to create DEM particle arrangements able to increase or decrease their AI, FE Ratio and ST Index by controlling the amount of protuberances around them, their size, and their surface friction.

PFC3D allows the user to generate these type of particle arrangements with an element known as a clump. A clump is a rigid body that consists of *n* number of spheres called pebbles. The surface of the clump is defined by the position and the radius of each one of these pebbles, and this surface acts as one entity. Clumps obey the equations of motion; therefore, these objects are able to translate, rotate, and interact with other clumps or spheres. Clumps require their mass, the position of their centroid, and their inertia tensor to be specified in order to function. The mass of the clump is specified by providing a density value (ρ) for either all of the clumps in the model, or a specific group of them, while the centroid of the clump and the inertia tensor is either automatically calculated by PFC3D, or input by the user. Lastly, clumps can be generated by either creating one clump at the time or by creating a clump template, which can then be reused. This template can be constructed by either specifying the radius and positon of each individual pebble within the clump, or by importing a surface mesh from a Computer Aided Design (CAD) software as a *.stl* file (Itasca, 2015). Figure 3.8 displays the PFC3D visualization of a three-pebble and two-pebble clump (Itasca, 2015).

Clumps can be arranged to mimic the AI of an aggregate particle by adding or removing pebbles on the surface of the clump. This addition or subtraction of pebbles would change the angles of the vertices of the line outlining the clump, and thus the AI. Clumps can also be arranged in a specific way to model the FE Ratio of an aggregate particle, by maintaining the ratio of the largest side to the smallest side of the clump constant. Since clumps are created using a template, the proportion of the largest to the smallest dimension is kept unchanged by increasing or reducing the size of the clump; therefore, the FE Ratio would not change. Lastly clumps can mimic the ST Index of an aggregate particle by increasing or decreasing the friction coefficient (μ) of the surface of the clump.

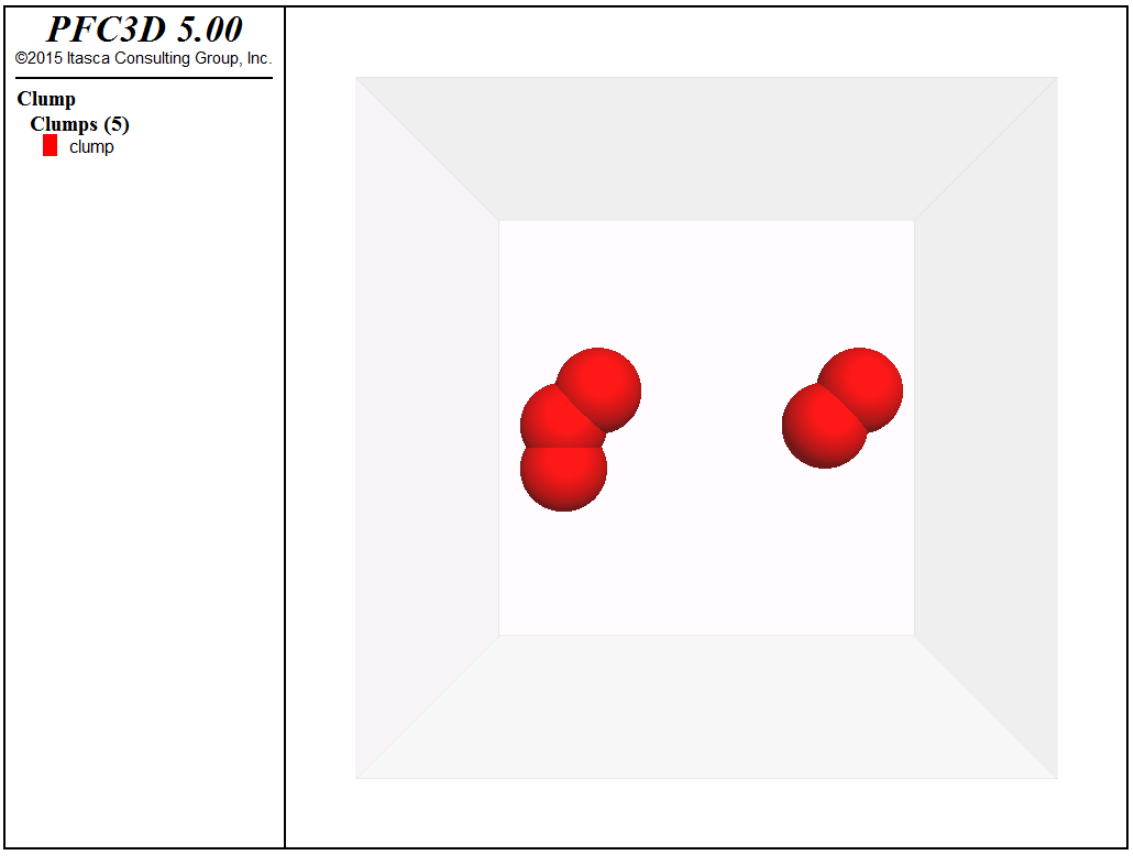

Figure 3.8 . PFC3D visualization of a three-pebble and a two-pebble clump (Itasca, 2015).

3.3.2.2 *Modeling aggregate morphology with clumps and results*

Clumps aimed to simulate the AI of real aggregate particles were developed by employing a clump with a varying amount of pebbles. The clump was initially modeled as a three-pebble clump, with one larger pebble in the middle and two smaller pebbles at the top and bottom of the main pebble. A schematic of this clump is presented in Figure 3.9. Since the AI calculation depends on the relative change of the angles at the vertices of the polygon that outlines the image of the aggregate particle, smaller additional pebbles were allocated to the mid-section of the middle pebble of the clump to create multiple peaks, force a pronounced relative change of angle, and thus change the AI of the clump.

In order to corroborate that the inclusion of smaller pebbles at the mid-section of the main pebble provided significant changes of the AI of the clump, hand calculations to compute the angularity of the front, top, and side views of the clump were performed following the same approach used by UIAIA. The process began by drawing the projection of one of the faces of the three-pebble clump previously discussed, in this case the top face, to which smaller pebbles to its mid-section had already been added (Figure 10a). Subsequently, a large polygon was drawn inside the large pebble, and triangles were drawn inside the smaller pebbles (Figure 10b). It is important to emphasize that the length of the sides of the polygon and the triangles were kept equal, since this is an important consideration taken by the UIAIA. The procedure outlined in Appendix B was used, in order to confirm that the sides of the different polygons were equally long. Next, the extra lines found at the intersection between the triangles and the polygon were removed to create one single 24- sided polygon (Figure 10c), and the angles at its vertices were computed (Figure 10d). The change of the angle was calculated for every pair of angles at the vertices, and the angularity of this projection was determined. This procedure is

carried out on each projection of the clump face, since the angularity of each face is necessary to calculate the AI of the clump. Figure 3.11 presents a schematic explaining the generation of the projections of each face of the clump, and process of developing the 24-sided polygon from these projections. These hand calculations were performed on clumps consisting of three to eleven pebbles, in order to observe the change in AI as the amount of pebbles increased. Figure 3.12 presents nine different variations of the top projection of each of these clumps. These clump projections were developed in AutoCAD to assure an accurate geometry. The summary of the results obtained from these analyses are presented in Table 3.4.

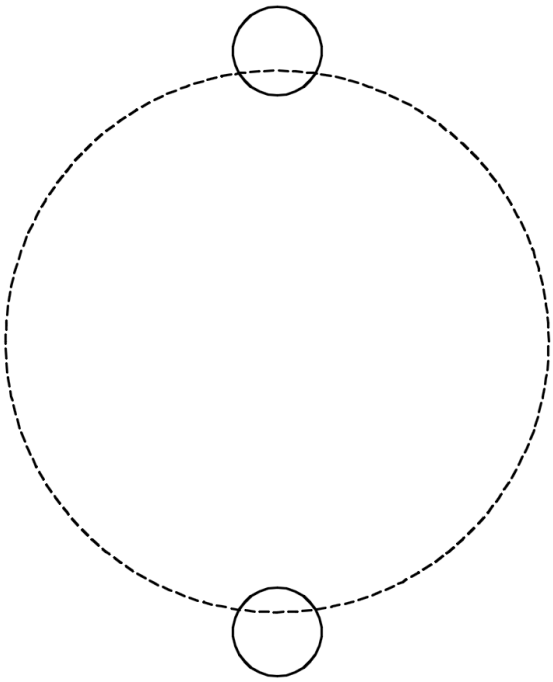

Figure 3.9 Front view of the three-pebble clump used as the main unit for generating clumps of varying AI

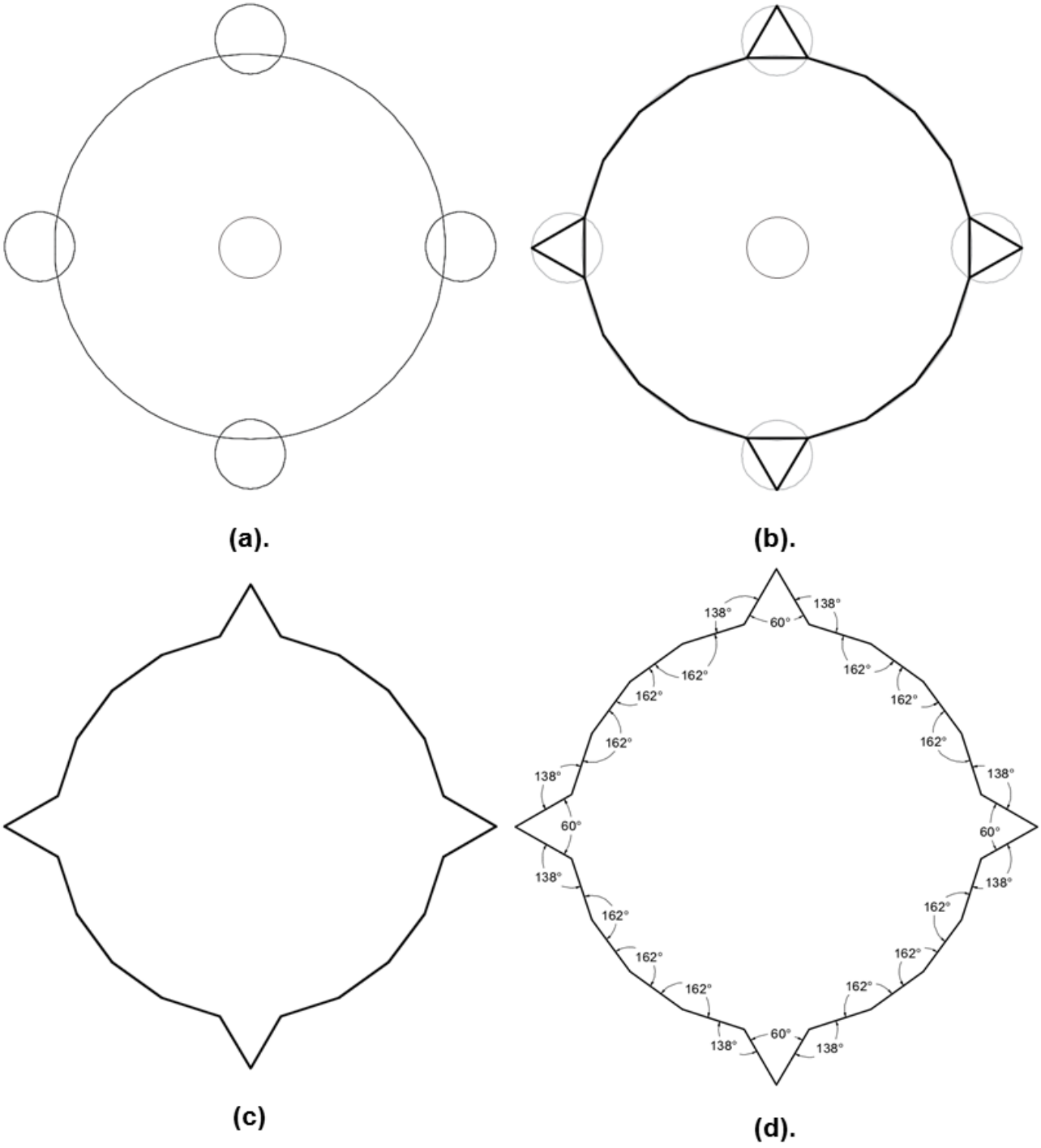

Figure 3.10 Step-by-step computation of angularity on the projection of the top view of a four-pebble clump.

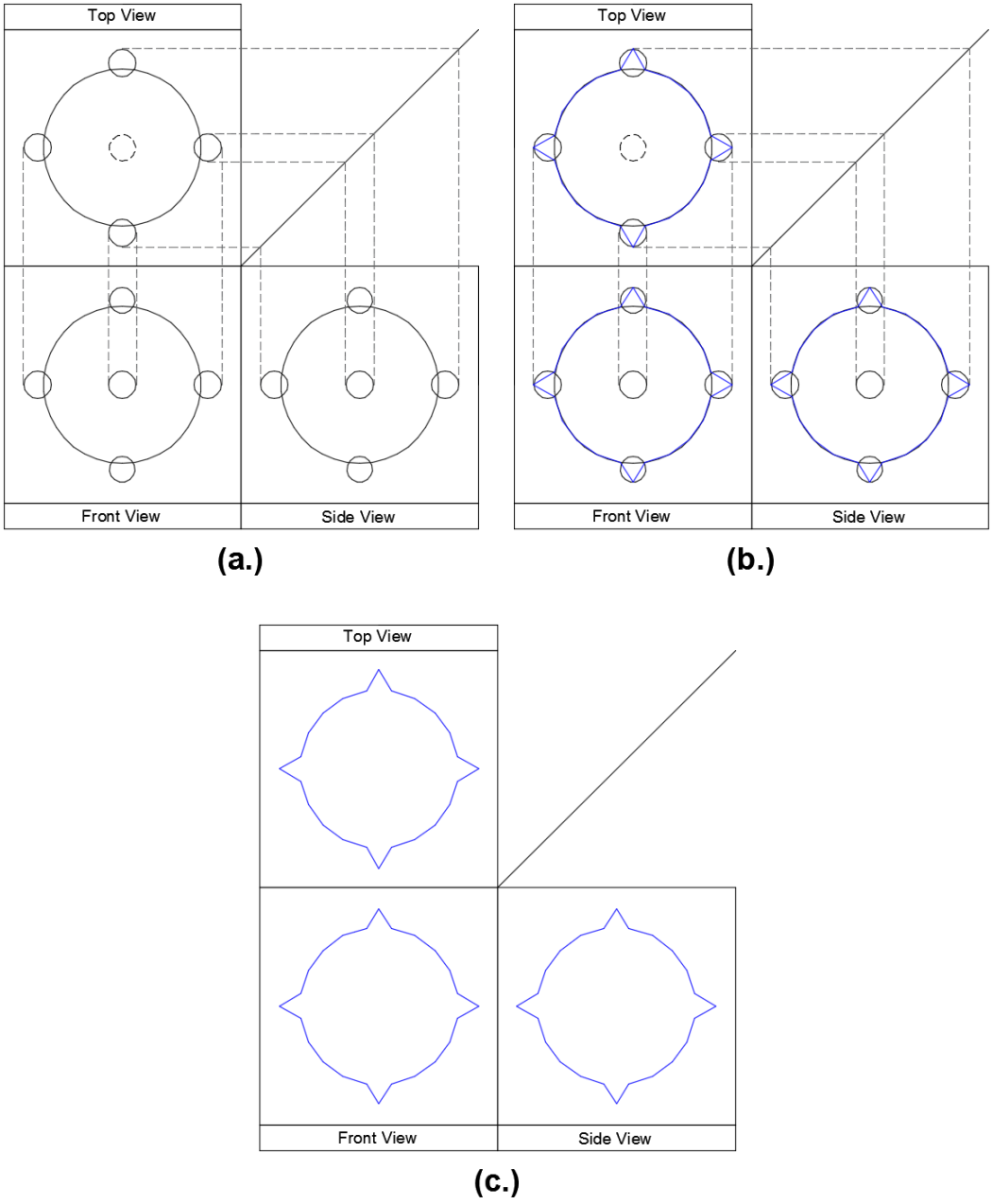

Figure 3.11 (a). Front, top, and side views of a seven-pebble clump. (b). Front, top, and side views of clump outlined with five polygons of equal side lengths. (c). 24-sided polygon outlining each view of the clump.

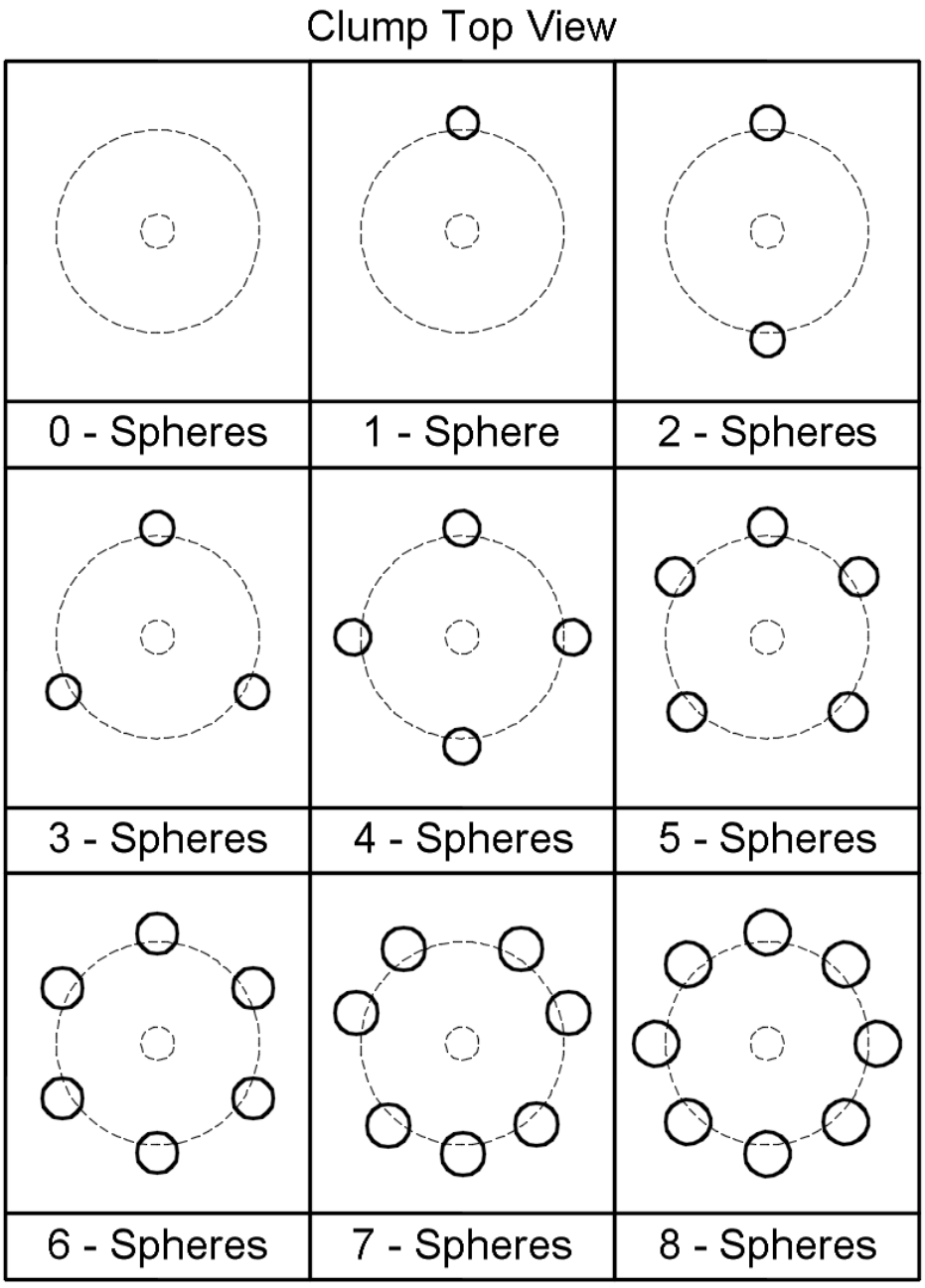

Figure 3.12 Variation of the top views of the main clump unit as additional spheres are added to change the AI of the clump

Table 3.4 Summary of the results obtain from the AI analysis on multiple clumps with different amount of pebbles.

No. Pebbles	Area			Angularity			AI
	Top (cm^2)	Front (cm^2)	Side (cm^2)	Top Deg.	Front (cm^2)	Side (cm^2)	(cm^2)
3	3.11	3.17	3.17	0	360	360	242
4	3.13	3.17	3.20	180	360	540	361
5	3.17	3.17	3.25	360	360	720	482
6	3.21	3.20	3.20	540	560	540	547
7	3.26	3.25	3.25	720	720	720	720
8	3.32	3.21	3.21	900	560	540	669
9	3.39	3.22	3.26	1,200	600	720	846
10	3.48	3.27	3.24	1,180	680	660	848
11	3.59	3.29	3.29	1,280	720	720	918

Although Rao et al., (2002) specified that the maximum value that can be calculated for the angularity projection of a particle is 720º, it evident that the UIAIA can calculate higher angularity values. The reason behind this is that for a triangle that is positioned on a straight line, the maximum angle that can be obtained from its corner to this line is 180º; however, when this triangle is not positioned on a straight line, like in the case of any of these clumps, this angle can be grater, and therefore the Angularity can reach a value greater than 720º. Since some of these angularity values were greater than the maximum value specified by the literature of the UIAIA, it was important to verify the accuracy of the calculation of the AI for these nine clumps. To do this, it was necessary to perform an actual image analysis on the clumps; therefore, 3D models of the nine different clumps were printed to conduct image analysis on them and validate the results. Figure 3.13 presents the 3D prints of all nine clumps.

3.3.2.3 *Image analysis of 3D printed clumps and results*

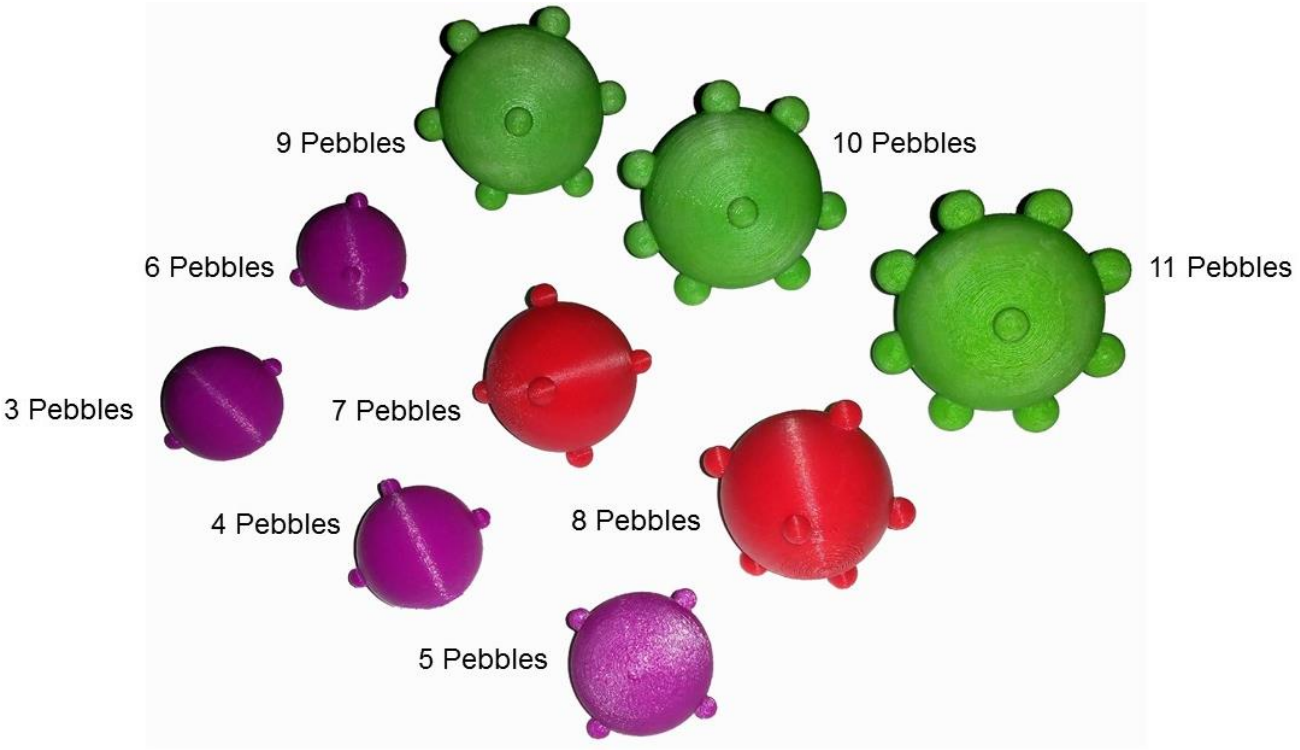

Figure 3.13 3-D printed clumps used to perform image analysis

The process by which image analysis was performed on the 3D prints of the clumps was slightly different than in the case for the actual aggregate particles. Since only one 3D print of each clump was available for this process, the images were taken manually, instead of by using the conveyor belt. Thirty-nine images of each clump were capture as the clump was placed in different positions in front the cameras. Figure 3.14 presents the image analysis procedure conducted on a seven-pebble 3D printed clump.

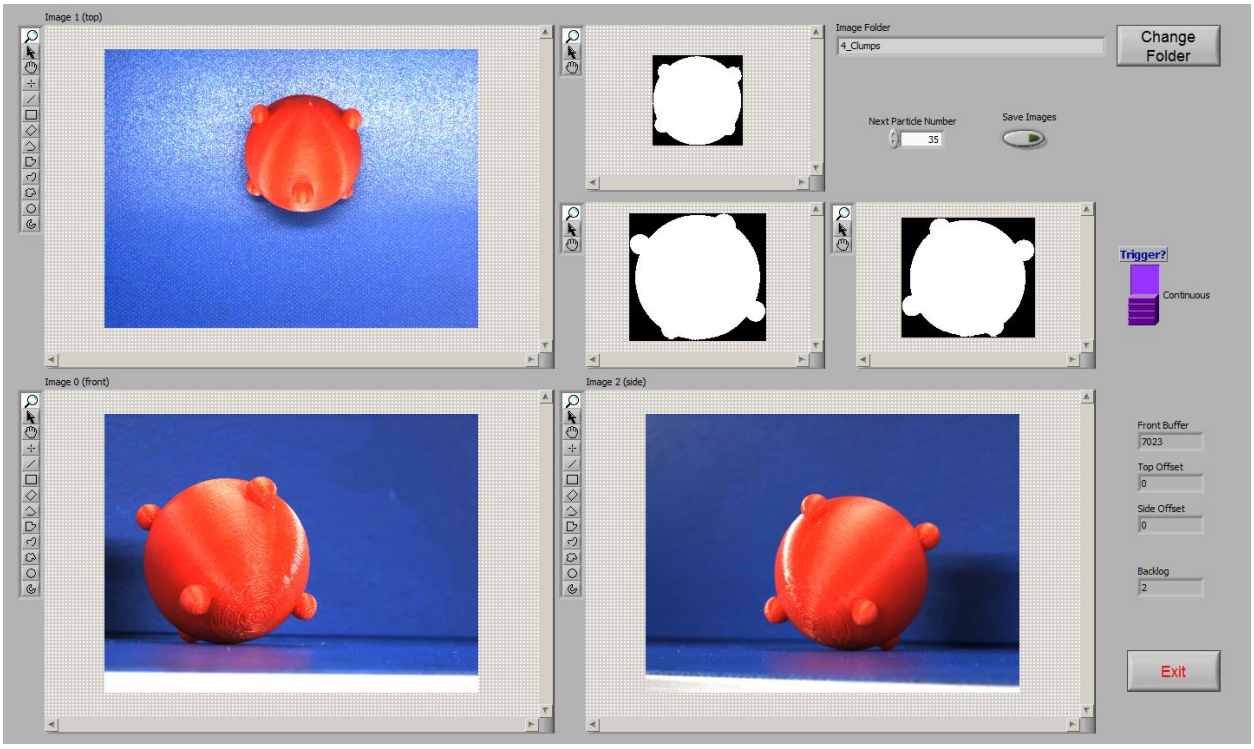

Figure 3.14 UIAIA Image analysis on a 3D printed clump

This procedure was performed on all the 3D prints of the clumps, and a summary of the AI and FE ratio results obtained from the UIAIA are presented in Table 3.5.

Table 3.5 Summary of AI and FE ratio of 3D printed clumps.

No. Pebbles	No. Particles Tested	Angularity Index (AI) (Degrees)			Flat- and-Elongation Ratio (mm/mm)		
		Avg.	σ	COV (%)	Avg.	σ	COV (%)
3	39	314	98.9	31.5	1.91	0.13	6.6
4	40	309	92.0	29.7	1.42	0.12	8.3
5	41	439	115.1	26.2	1.47	0.10	7.0
6	39	640	97.9	15.3	1.92	0.13	6.7
7	39	647	94.6	14.6	1.72	0.08	4.8
8	39	813	112.3	13.8	1.62	0.07	4.3
9	40	878	57.7	6.6	1.58	0.08	4.9
10	39	971	111.1	11.4	1.57	0.04	2.6
11	40	1051	73.6	7.0	1.65	0.06	3.4

In order to determine the difference in the AI results calculated by hand and by the UIAIA, the values computed were plotted against the values obtained by the UIAIA. A satisfactory agreement between the results obtained from both procedures was observed. Furthermore, it was observed that the inclusion of additional pebbles at the mid-section of the clump effectively increases the AI of the clump. The results are illustrated in Figure 3.15.

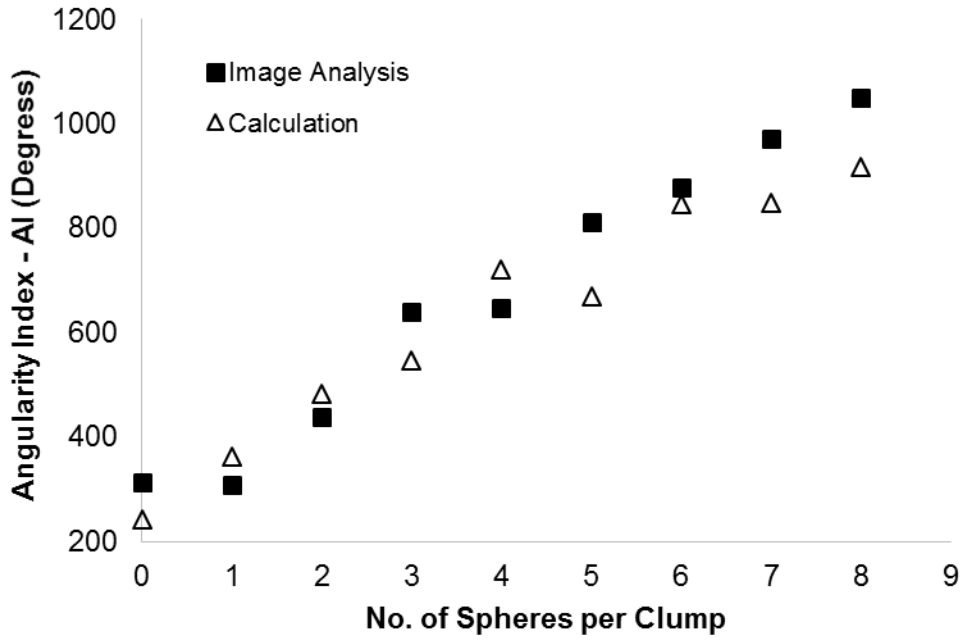

Figure 3.15 Computed (Image Analysis) and hand-calculated (Calculation) AI values of clumps 3D prints.

The results from both procedures do not perfectly match due to the fact that some of the projections of the clumps could not be satisfactorily broken into 24 sided polygons of equal length. Nevertheless, these results exhibit an acceptable agreement between the hand-calculated values for AI and the ones computed by the UIAIA, and can be used for studying the influence of aggregate morphology in the stabilizing capabilities of multiaxial geogrids.

Lastly, in order to visualize the influence of the AI on the shear strength of the clumps, clumps with different amount of pebbles located inside of a hopper were dropped from a height of 60 cm, to observe their angle of repose. Clumps with one, three, five, six, nine, and eleven pebbles were used for these simulations. The friction coefficient of the clumps' surface was kept constant at 0.7, in order to isolate the contribution of the amount pebbles in the clump. The angle of repose obtained from these simulations were equal to 22^{o}, 26^{o}, 28^{o}, 32^{o}, 34^{o}, and 36^{o} for clumps with one, three, five, six, nine, and eleven pebbles respectively; therefore, it can be concluded that as the AI of the clumps increased, the angle of repose increase as well. Figure 3.15 show the clump heaps obtained from each simulation and their respective angle of repose.

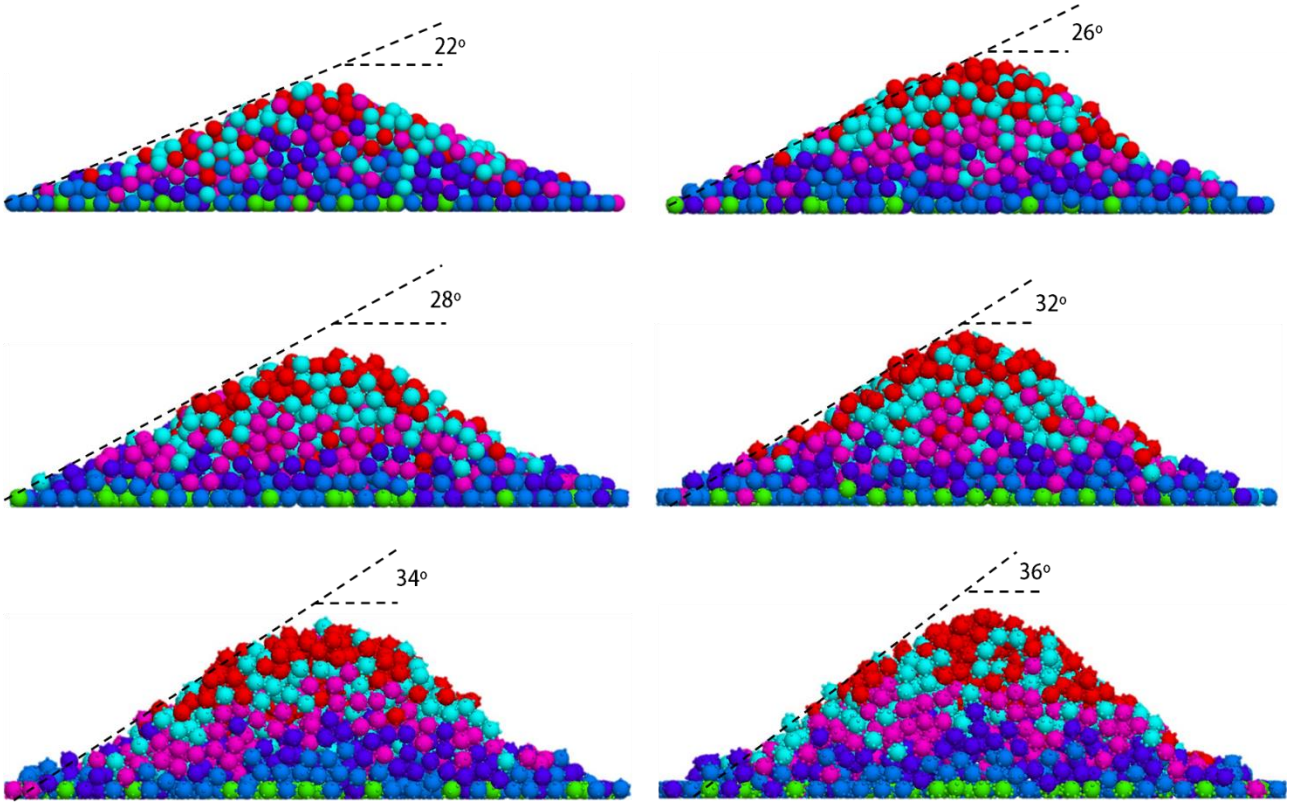

Figure 3.16 Angle of repose of a pile of (a.) spheres (b.) 3-pebble clumps, (c.) 5-pebble clumps, (d.) 6-pebble clumps, (e.) 9-pebble clumps, and (f.) 11-pebble clumps with equal coefficient of friction.

3.4 Conclusion

Image analysis was performed on four different specimens of aggregate across the State of Georgia using the University of Illinois Aggregate Image Analyzer (UIAIA), in order to assess the aggregate locally available. The Flat-and-Elongated (FE) ratio, the Angularity Index (AI), and the Surface Texture (ST) Index were calculated. A DEM model using PFC3D was developed, in order to simulate aggregate particles with clumps. Nine different clumps, with different amount of pebbles each, were developed, in order to simulate aggregate particles with different AI. Hand calculations were performed to calculate the AI of these clumps. Three-dimensional (3D) prints of each clump were fabricated, in order to corroborate the AI of these clumps. The results obtained from this procedure exhibit an acceptable AI agreement between the hand-calculated values versus the ones obtained by the UIAIA. Aggregate heap simulations using different clumps with the same coefficient of friction were also performed, in order to observe the rise in angle of repose due to the change in AI. These simulations were effective in demonstrating that as the AI increases the angle of repose of the clumps increase. These results indicate that the clumps developed in this study are suitable for the study of the influence of aggregate morphology in the stabilizing capabilities of multiaxial geogrids

CHAPTER IV: GEOGRID MODELING

4.1 Introduction

The successful study of the interaction between geogrids and aggregate materials at the microscale level has been achieved utilizing the Discrete Element Method (DEM) since the early 2000's. Throughout this time, the majority of the studies focused on this matter have developed and calibrated geogrid models based on different physical laboratory testing results and modeling considerations.

In order to determine the optimum aggregate gradation between multiaxial geogrids and aggregate, it is necessary to develop a geogrid DEM model capable of studying this matter at the microscale level, which includes the pertinent parameters required to accurately represent the physical behavior of multiaxial geogrids.

This chapter focuses on three main topics. The first one focuses on performing laboratory single rib tensile test on TX130s, TX140, and TX190L specimens, in order to determine the geogrid material and geometrical properties necessary to develop a representative geogrid DEM model. The second one focuses on utilizing these material and geometrical properties to compute the micromechanical parameters required to develop a geogrid DEM model using the parallel bond contact method available in the Particle Flow Code (PFC) 3D, and calibrating this model to the results obtained from the physical testing. Lastly, the third one focuses on developing the overall geometry of the TX130s, TX140, and TX190L specimens that will be used in the DEM model.

4.2 Discrete element modelling using PFC3D

Before the discussion and development of a DEM model of multiaxial geogrids continues, a brief explanation of the main idea behind this method, and the different contact models utilized for this problem, and available in PFC3D, are presented.

4.2.1 Overview of the Distinct Element Method and Particle Flow Code (PFC) 3D

In 1979, Cundall and Strack introduced the distinct-element method, which was an efficient and novel numerical model capable of studying the behavior of granular media and determining the non-linear interaction between large numbers of particles by simplifying the geometry of the grains to a two-dimensional assembly of disks. These disks predicted the behavior of stressed granular materials, by tracing the movements of the individual particles. These movements occurred from the application of forces at the boundary of the granular material, which propagated as a function of the physical properties of the disks.

The method computed the velocities and accelerations of the disks due to the external forces, utilizing Newton's second law to determine the overall motion of the assembly. The force-displacement law at the contacts was utilized to describe the contact forces developed between a particle and its neighbors during a very small increment of time, known as time step, in which the velocities and accelerations of the disks were assumed to be constant.

These disks were modeled as rigid bodies unable to deform; however, they were allowed to overlap. The overlap, which was small in comparison to the disk diameter, represented the contact force developed between two disks.

In order to determine the overall movement of the disks and the contact force development at the boundary between disks, the method switched back and forth between the analysis to calculate the motion of the disks and contact forces between them.

PFC 3D is a distinct-element modeling framework, which utilizes and expands the method developed by Cundall and Strack (1979) to determine the movement and interactions between particles of finite size and mass. PFC3D deviates from the approach of using disks to study the behavior of granular materials, and instead implements the use of spheres. The expansion of the method to study three-dimensional effects of granular material behavior allows PFC3D to investigate problems where 3D effects play an important role, such as the interlocking of aggregate particles with geogrids.

In addition to spheres, PFC 3D implements another component to their model called walls. Walls are utilized to apply velocity at the boundary of the granular material with the purpose to confine or compact the granular material. Walls do not obey the laws of motion dictated by Newton's second law, and instead they move and interact with spheres according to the user's specifications.

PFC3D includes multiple contact models, which govern the response between the different elements in PFC3D. These contact models can be modified, in order to investigate different scenarios.

In order to model multiaxial geogrids, spherical particles require to be bonded in a triangular shape. The bond of particles can be attained by using the linear parallel bond contact method found in PFC3D. An explanation of the linear contact and linear parallel bond methods are presented in the following section.

4.2.1.1 *Linear elastic contact model*

The linear contact model allows the interaction between two spheres or clumps through an infinitesimal interface. This interface only transfers interparticle forces through the application of compressive forces, and it is unable to transmit tension or resist relative rotation. The total contact force in this contact model is obtained by adding the linear and dashpot forces developed at this interface.

The behavior of the elements under this model can be described as linear elastic and frictional. Also, particle slippage behavior is determined by the Coulomb frictional model, which depends on the particle friction coefficient μ.

The determination of interparticle forces takes place in PFC3D by using a force-displacement law (Hook's law). To achieve this, particle contact is envisioned as a spring, which contains values for normal and shear stiffness assigned by the user. The displacement of the spheres, which is determined by their velocity and the length of the time step, is multiplied by the normal and shear stiffness values of the sphere, in order to compute interparticle forces. Furthermore, the interaction between multiple spheres using this contact model is portrayed as the interaction between multiple springs connected in series as it can be observed in Figure 4.1. Figure 4.2. describes the behavior of two spheres under the linear contact model.

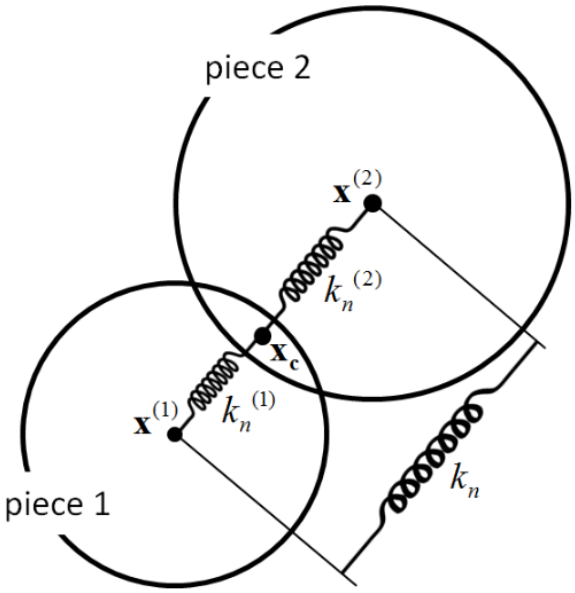

Figure 4.1 Relation of normal stiffness to piece normal stiffnesses for the linear model (Itasca, 2015)

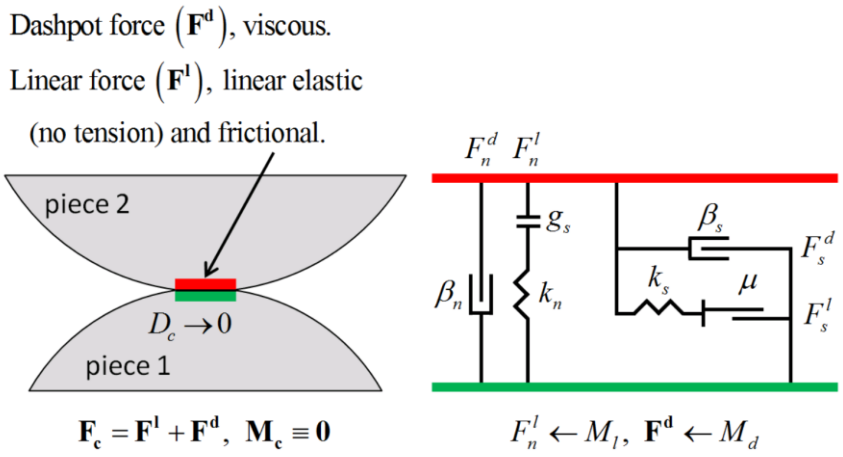

Figure 4.2 Behavior and rheological components of the linear model (Itasca, 2015)

The equations to determine the total linear and shear forces at the interface between two spheres are the following:

$$F_c = F^l + F^d, \quad M_c \equiv 0$$

$Where\ F_c\ is\ the\ total\ contact\ force, F^l\ is\ the\ linear\ force, and\ F^d is\ the\ dashpot\ force.$

$$F^l = -F_n^l \cdot \hat{n}_c + F_s^l$$

$$F^d = -F_n^d \cdot \hat{n}_c + F_s^d$$

$Where\ -F_n^l\ is\ the\ normal\ linear\ force, -F_n^d\ is\ the\ normal\ dashpot\ force, and\ \hat{n}_c\ is\ the\ unit\ vector\ on\ the\ n\ axis\ in\ the\ nts\ coordinate\ system\ for\ tensor\ notation.$

$F_n^l\ and\ F_n^d\ are\ used\ when\ the\ tensile\ component\ of\ the\ contact\ is\ active. Since\ the\ linear\ contact\ model\ does\ not\ tranfer\ tensile\ forces, these\ values\ are\ equal\ to\ zero.$

$$F_s^l = F_{ss}^l \hat{s}_c + F_{st}^l \hat{t}_c$$

$Where\ F_s^l\ is\ the\ the\ total\ linear\ force, F_{ss}^l\ is\ the\ linear\ shear\ force\ component\ in\ the\ s\ access, F_{st}^l\ is\ the\ linear\ shear\ force\ in\ the\ t\ axis, and\ \hat{s}_c\ and\ \hat{t}_c\ are\ the\ unit\ vectors\ on\ the\ s\ and\ t\ axis.$

The contact plane coordinate system used by to describe the behavior of the linear and shear forces is presented in Figure 4.3.

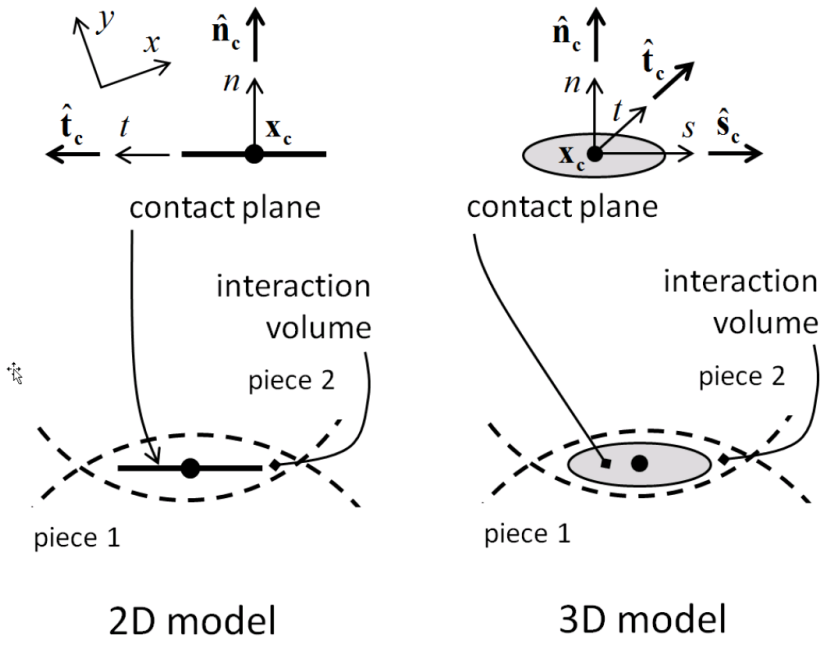

Figure 4.3 Contact plane coordinate system for 2D and 3D model (in tensor notation) (Itasca, 2015)

The process by which contact forces and particle motion are determined is the following:

1. The linear force is updated. In cases where the gap between the parties g_S is greater than zero, the linear force is zero. If not, the following logic applies:

$$F_n^l = \begin{cases} \begin{cases} k_n g_s, & when\ g_s < 0 \\ 0, & otherwhise \end{cases} \\ \min\left(\left(\left(F_n^l\right)_0 + k_n \cdot \Delta\delta_n\right), 0\right) \end{cases}$$

$where\ \left(F_n^l\right)_0 is\ the\ linear\ force\ at\ the\ beginning\ of\ the\ timestep, k_n is\ the\ contact\ normal\ stiffness, and\ \Delta\delta_n\ is\ the\ relative\ ball\ displacement\ accumulation.$

2. The shear force is updated:

$$F_s^* = \left(F_s^l\right)_0 - k_s \Delta\delta_s$$

$Where\ \left(F_s^l\right)_0\ is\ the\ shear\ forece\ at\ the\ begining\ of\ the\ timestep, k_s\ is\ the\ contact\ shear\ stiffness, and\ \Delta\delta_s\ is\ the\ change\ in\ relative\ ball\ shear\ displacmenet\ accumulation.$

3. Update the shear strength of the interface:

$$F_s^\mu = -\mu F_s^l$$

$Where\ F_s^\mu\ is\ the\ shear\ strength\ of\ the\ interface, \mu\ is\ the\ contact\ friction\ coefficient, and\ F_s^l\ is\ the\ shear\ force\ at\ the\ contacts.$

4. Update the shear force:

$$F_s^l = \begin{cases} F_s^*, & \|F_s^*\| \le F_s^\mu \\ F_s^\mu \left(\dfrac{F_s^*}{\|F_s^*\|}\right), & Otherwise \end{cases}$$

$Where\ F_s^*\ is\ the\ shear\ force\ excerted, F_s^\mu\ is\ the\ shear\ strength\ ot\ the\ contact, and\ \|F_s^*\|\ is\ the\ shear\ force\ magnitude.$

5. Update the slip state of the contact.

$$s = \begin{cases} true, & \left\|F_s^l\right\| = F_s^\mu \\ false, & otherwise \end{cases}$$

6. Update the linear force according to the dashpot mode:

$$F_n^d = \begin{cases} F^*, & dashpot\ mode\ \{0,2\} \\ \min\left(F^*, -F_n^l\right), & dashpot\ mode\ \{1,3\} \end{cases}$$

$$Where, \qquad F^* = \left(2\beta\sqrt{m_c k_s}\right)\dot{\delta_n}, \qquad and\ m_C = \begin{cases} \dfrac{m^1 \cdot m^2}{m^1 + m^2}, & for\ ball - ball\ case \\ m^1, & for\ ball - wall\ case \end{cases}$$

$Also, \beta\ is\ the\ critical\ damp\ ratio\ specified\ by\ the\ use, m^b is\ the\ mas\ of\ the\ body, \delta_n\ is\ the\ relative\ normal\ translational\ velocity\ and\ F^*\ is\ the\ entire\ dashpot\ force.$

7. Update the shear force according to the dashpot behavior mode:

$$F_s^d = \begin{cases} \left(2\beta\sqrt{m_c k_s}\right)\dot{\delta_s}, & s = false \\ 0, & s = true \end{cases}$$

4.2.1.2 *Linear parallel-bond contact model*

The linear parallel bond contact model behaves similarly to the linear contact model; however, this contact model allows particles to develop bonds between them and act together. The idea behind this contact model is to simulate the case where a bond develops between two grains of soil due to development of cementitious material between them. Thanks to the bond that develop between the grains, the parallel bond contact model, allows for the development of tensile forces and rotational moments (Itasca, 2015).

The bond created between the spheres lays at the circular interface between the spheres (Figure 4.4), and it is represented by multiple linear elastic springs with normal and shear stiffness distributed on this area; therefore, this model not only specifies the normal and shear stiffness of the contact, but also the normal and shear stiffness of the bond.

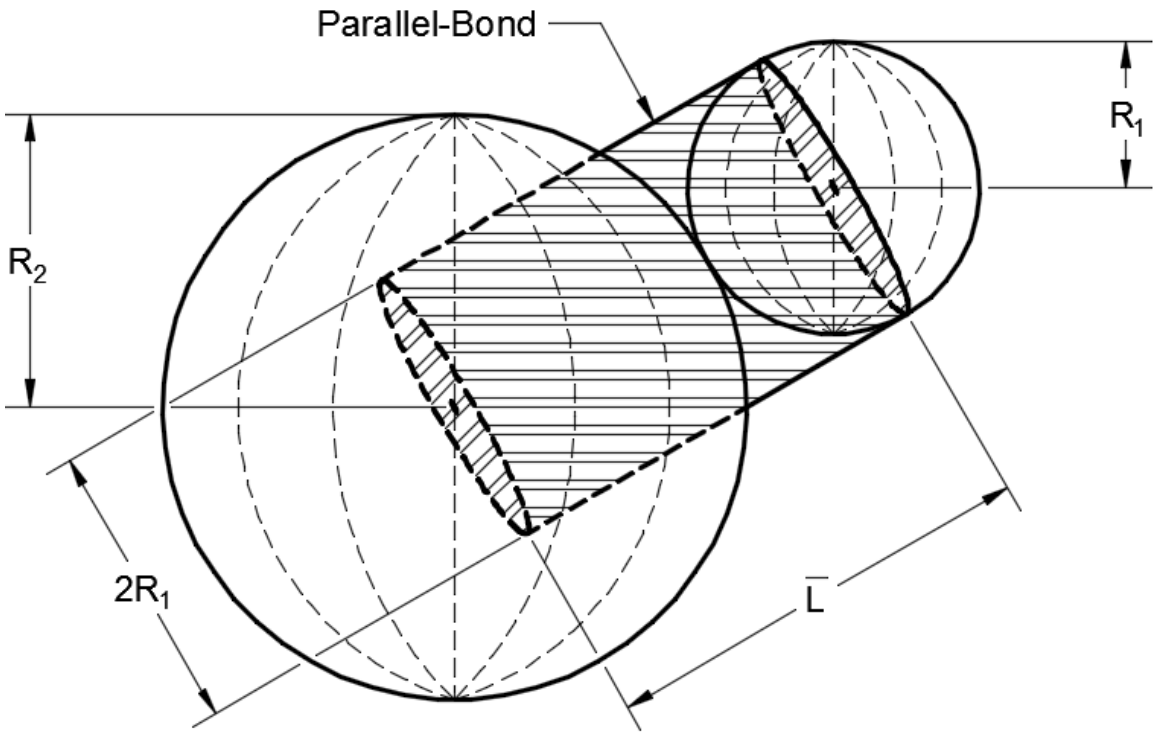

Figure 4.4 Parallel bond representation

The linear parallel contact model acts in parallel with the linear contact model. A graphical representation of this behavior is shown in Figure 4.5. This coupling of these two methods is necessary to study the behavior of cemented grains. This feature allows the

parallel bond model to default to the linear contact model as soon as the parallel bond breaks, and determine the behavior of the spheres using the linear contact model, since the elements in the model cannot carry tensile forces or transmit moments anymore. Lastly, the bonds between the particles are represented as springs, which act in parallel with the springs that represent the linear component of the linear contact model.

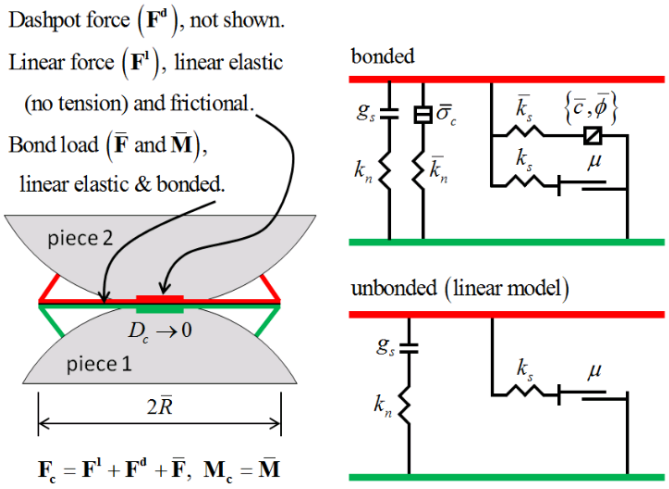

Figure 4.5 Linear parallel contact method (Itasca, 2015)

The equations to determine the total parallel-bond normal and shear forces at the interface between two spheres are the following:

$$F_c = F^l + F^d + \bar{F}, \quad M_c = \bar{M}$$

$Where\ \bar{F}\ is\ the\ paralle-bond\ force, and\ \bar{M}\ is\ the\ parallel-bond\ moment.$

The parallel-bond force ($\bar{F}$) is resolved into normal ($\bar{F}_n$) and shear forces ($\bar{F}_s$), while the parallel-bond moment ($\bar{M}$) is resolved into torsional ($\bar{M}_t$) and bending moment ($\bar{M}_b$).

$$\bar{F} = -\bar{F}_n \hat{n}_c + \bar{F}_s$$

$$\bar{M} = \bar{M}_t \hat{n}_c + \bar{M}_b$$

The parallel-bond shear force and bending moment occur at the interface between the two spheres. The interaction is predicted by the following:

$$\bar{F}_s = \bar{F}_{ss} \hat{s}_c + \bar{F}_{st} \hat{t}_c$$

$$\bar{M}_b = \bar{M}_{bs} \hat{s}_c + \bar{M}_{bt} \hat{t}_c$$

The processes by which contact forces, particle motion, tensile forces, and rotational moments are determined is presented next:

1. The cross-sectional bond properties are updated:

   Contact Radius:

$$\bar{R} = \begin{cases} \min(R^1, R^2), & ball - ball \\ \bar{R} = R^{(1)}, & ball - wall \end{cases}$$

$$Where\ R^{(1)} and\ R^{(2)}\ are\ the\ ball\ radius$$

   Contact Area:

$$\bar{A} = \pi \bar{R}^2$$

Moment of inertia:

$$\bar{I} = \frac{1}{4}\pi \bar{R}^4$$

Polar moment of inertia:

$$\bar{J} = \frac{1}{2}\pi \bar{R}^4$$

2. The normal force is updated:

$$\bar{F}_n \coloneqq \bar{F}_n + \bar{k}_n \bar{A} \Delta\delta_n$$

$$\Delta\delta_n = Relative\ normal - displacement\ increment$$

3. The shear force is updated:

$$\bar{F}_s \coloneqq \bar{F}_s + \bar{k}_s \bar{A} \Delta\delta_s$$

$$\Delta\delta_s = Relative\ shear - displacement\ increment$$

4. The torsional moment is updated:

$$\bar{M}_t \coloneqq \bar{M}_t - \bar{k}_s \bar{J} \Delta\theta_t$$

$$Where: \Delta\theta_t = Relative\ twist - rotation\ increment$$

5. The bending moment is updated:

$$\bar{M}_b \coloneqq \bar{M}_b - \bar{k}_n \bar{I} \Delta\theta_b$$

$$Where: \Delta\theta_b = Relative\ bend - rotation\ increment$$

6. The normal and shear stresses are updated:

$$\bar{\sigma} = \frac{\bar{F}_n}{\bar{A}} + \bar{\beta}\frac{\|\bar{M}_b\|}{\bar{I}}\bar{R}$$

$$\bar{\tau} = \frac{\bar{F}_s}{\bar{A}} + \bar{\beta}\frac{\|\bar{M}_t\|}{\bar{J}}\bar{R}$$

$$Where: \bar{\beta} = Moment - contribution\ factor$$

The bond automatically breaks if any of these stresses surpass the normal or shear bond strength.

4.3 Physical laboratory testing of multiaxial geogrid ribs and results

4.3.1 Geogrid specimens used in this test.

Three different types of Tensar multiaxial are used in this study: TX130S, TX140, and TX190L. TX130S and TX140 have rib length equal top 33 mm and 40 mm, respectively, and are mainly used in roadway applications. TX190L has a rib length equal to 60mm, and it is mainly used in railway applications. Figure 4.6 presents specimens of each type of multiaxial geogrid used in this study.

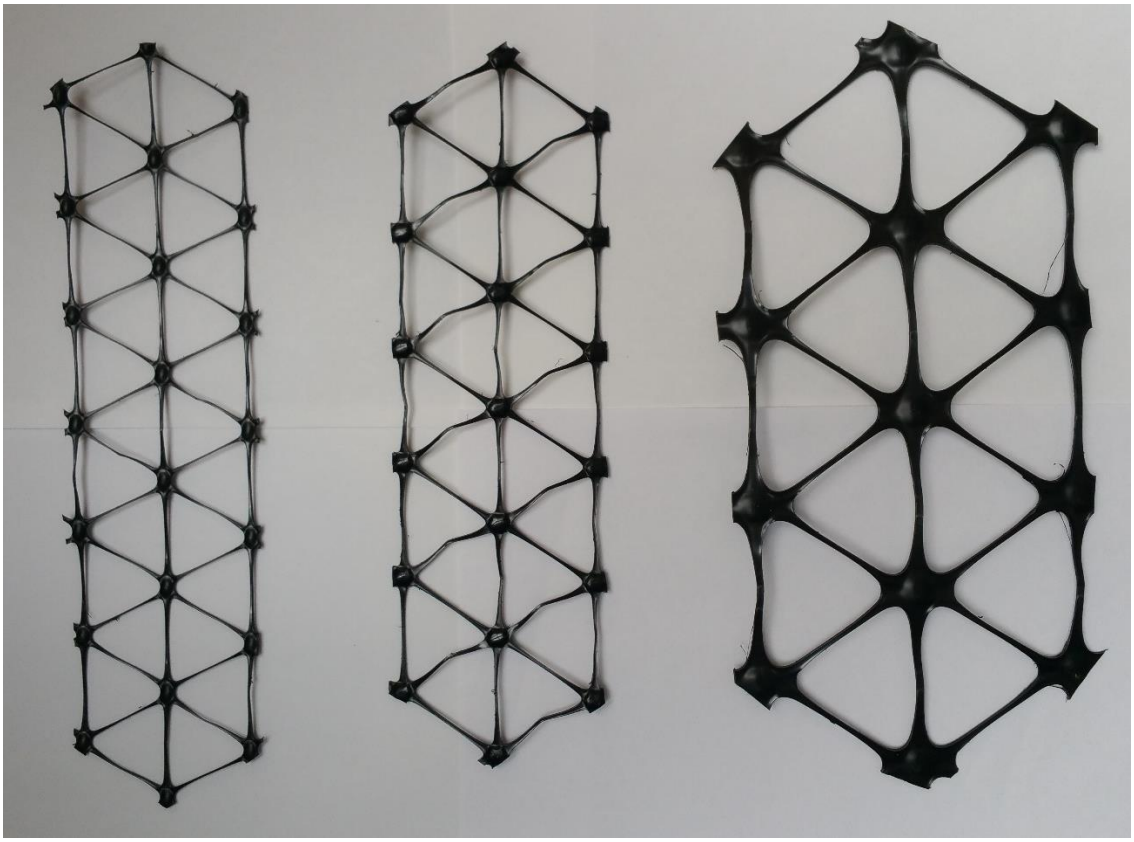

Figure 4.6 Specimens of TX130S, TX140, and TX190L

4.3.2 Single rib tensile test - Modified ASTM D6637

In order to determine the physical micromechanical parameters necessary to develop a representative DEM model of the geogrid in PFC3D, the single rib tensile test was performed on multiple specimens of each geogrid type. Since the approach used for this study focused on calibrating the geogrid model beginning at the rib level, a modified ASTM D6637 procedure was used as a reference to determine the stress-strain behavior of a single geogrid rib.

4.3.2.1 *Procedure*

Ten rib specimens from each geogrid type were obtained from different locations within the roll. The length, thickness, and height of each rib was recorded, before the test was performed. The junctions of each rib were placed between two bolt washers before locating them inside the jaws of the axial load frame, to avoid stress concentrations at the joint and premature failure at this location. Three specimens from each geogrid type, and their test setup, are presented in Figure 4.7. and Figure 4.8., respectively.

Figure 4.7 TX130S, TX140, and TX190L specimens for single rib tensile testing

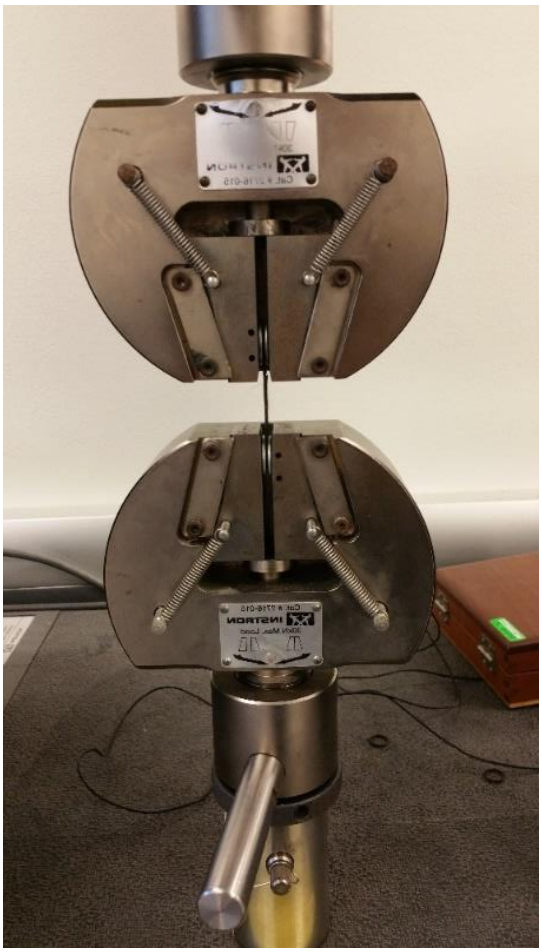

Figure 4.8 Single rib tensile test setup

After each specimen was placed in the load frame, an extension rate equal to 0.06 mm/sec was applied to each specimen until rupture of the rib occurred. The results from this test yielded force and extension data, which was later used to calculate the stiffness of the each specimen. The results of the test are summarized in the following section.

4.3.2.2 *Results*

The stress-strain behavior of multiaxial geogrids presented an undefined elastic region as can be observed in Figure 4.9. Due to this behavior, the elastic modulus and stiffness of the geogrid was specified by an arbitrary point in the Force vs. Extension curve.

Since Tensar reports the radial stiffness of multiaxial geogrids at 0.5%, and several studies have indicated that multiaxial geogrids mobilize their reinforcement capabilities at strains on the order of 0.5% (Jas et al., 2015), this study based the stiffness and modulus of elasticity of TX130S, TX140, and TX190L on this value.

Average stiffness values equal to 189 kN/m, 194 kN/m, and 451 kN/m were found for TX130S, TX140, and TX190L, respectively; however, significant variability was observed among these specimens. As an example, the variation of the stiffness of TX190L is presented in Figure 4.10. The standard deviation and the coefficient of variation of the data obtained were calculated, in order to assess the variability of the results. Standard deviation values equal to 707 mPa, 707 mPa, and 398 mPa were calculated for TX130S, TX140, and TX190L respectively. Coefficient of variation values equal to 13%, 12%, and 7% were obtained for TX130S, TX140, and TX190L respectively. Although discrepancies in the data obtained exist, the coefficient of variation for all three specimen indicate that this variation is not extremely high; therefore the data was considered appropriate for use. A summary of the results obtained from single rib tensile test of all three multiaxial geogrids is presented in Table 4.1

Table 4.1 Single rib tensile test results

TX type	No. of Trials	Max. Axial Load (N)	Avg. Load at Breakage (N)	Avg. Stiffness (kN/m)	Avg. Modulus (mPa)	STD (mPa)	COV (%)
TX130S	10	484	440	189	5,434	707	13
TX140	11	467	449	194	5,724	707	12
TX190L	10	1,230	1,136	451	5,782	398	7

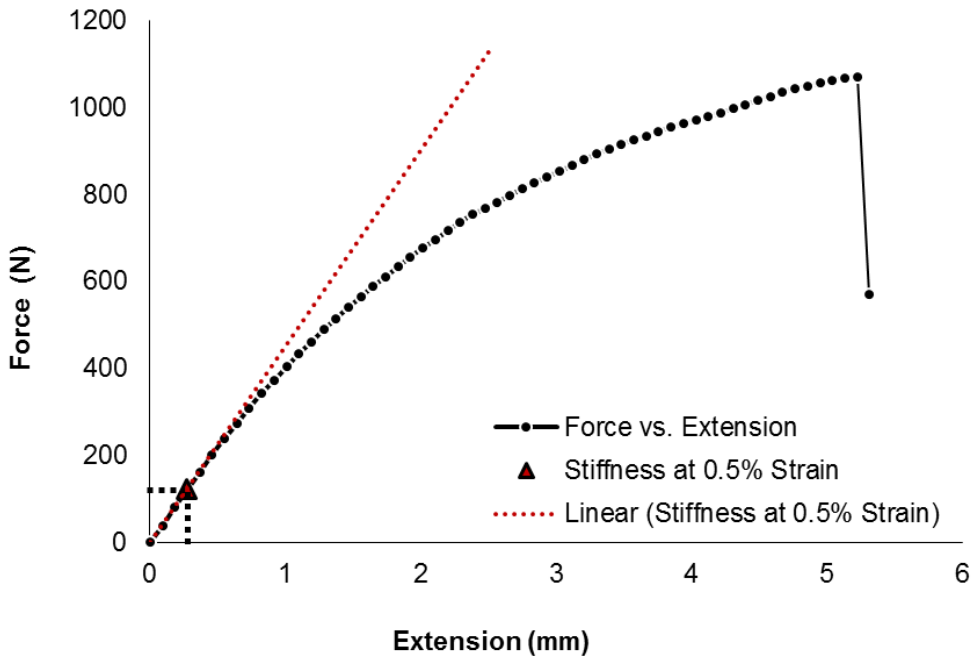

Figure 4.9 Sample of the Force vs. Displacement curve of TX190L specimen, and its stiffness at 0.5% strain

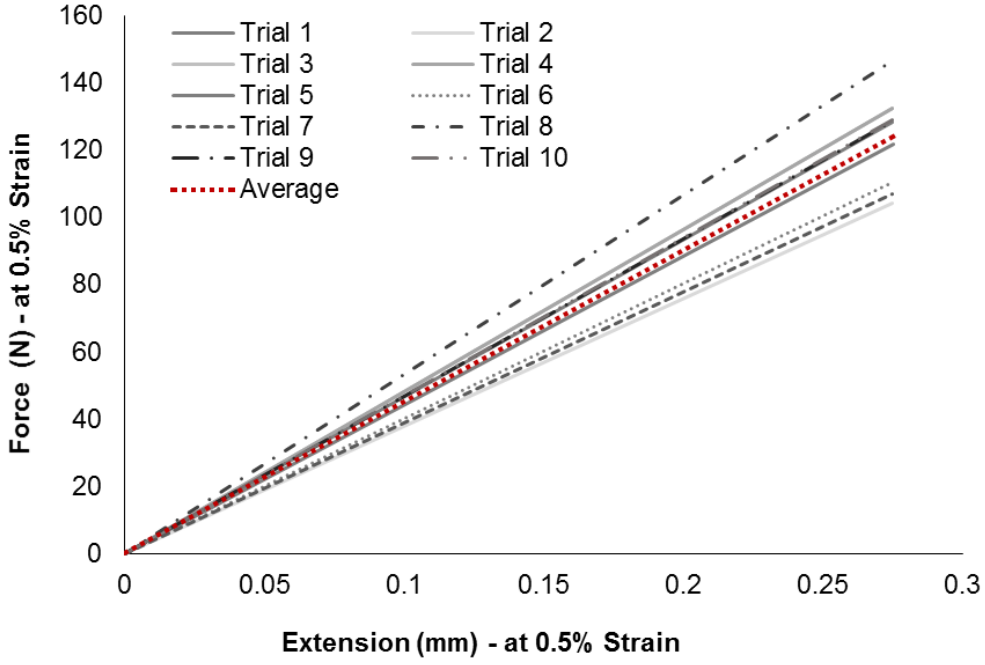

Figure 4.10 Variability of the stiffness at 0.5% strain of TX190L specimen

4.4 Numerical model

4.4.1 Previous studies on DEM modeling of geogrids

Multiple studies have focused on three-dimensional modeling of geogrids in DEM. Some studies used rigid elements to simulate the geogrid (Tutumluer et al., 2010; Qian et al, 2011; Chen, 2013), while others focused on utilizing the parallel-bond contact model to bond different sphere arrangements and generate the geogrid geometry. (Konietzky et al., 2004; McDowell et al., 2006; Ferellec and McDowell, 2012; Stahl, et al.; 2013; Ngo et al., 2014)

Most of these studies calibrated their geogrid models with data obtained from geogrid single rib tensile test (ASTM D6637) (McDowell et al., 2006; Ngo et al., 2014). Other studies performed a more rigorous model calibration, and included data from single junction test (GRI GG2), and in-plane rotation test (GRI GG9) (Konietzky et al., 2004; Ferellec and McDowell, 2012; Chen, et al., 2013; Stahl, et al.; 2013).

The majority of these studies performed DEM models of biaxial geogrids, and only a few of them modeled multiaxial geogrids (Chen, et al., 2013; Jas et al. 2015). The authors of these studies made sure to develop simple geogrid models, in order to avoid unreasonable computational times; however, a couple of studies focused on developing precise geogrid models to obtain the closest results to the real behavior of them (Konietzky et al., 2004, and Chen, et al., 2013). These later studies modeled the geometry of geogrids with arrangements of multiple chains spheres spreading horizontally and vertically to provide a varying width and rib height as it can be observed in Figure 4.11. and Figure 4.12.

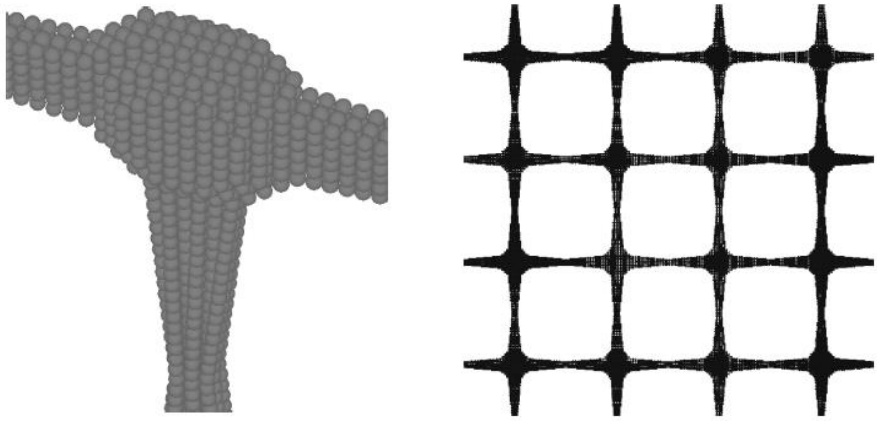

Figure 4.11 DEM model of biaxial geogrid Presented by Konietzky et al., 2004

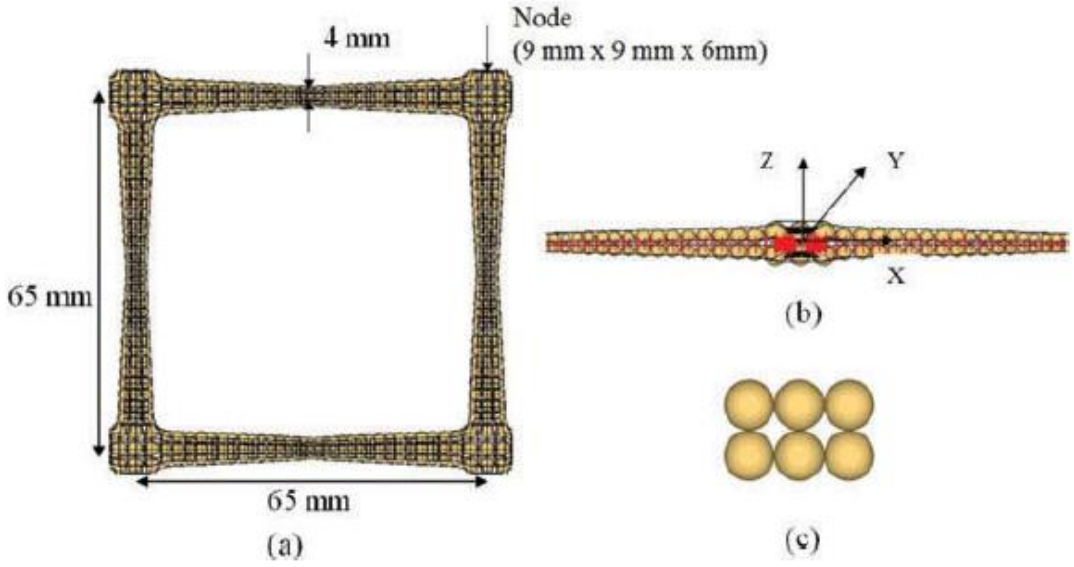

Figure 4.12 DEM model of biaxial geogrid Presented by Chen, et al., 2013

These models, although very detailed and accurate, were found to be very computationally demanding, and the acquisition of results was found to be slow.

Due to this limitation this study focused on simplifying the geogrid geometry, and modeling the geogrid ribs as a chain of spheres connected to a larger sphere at its end to simulate the geogrid junction.

4.4.2 Development of micromechanical parameters for geogrid model

In order to develop a satisfactory geogrid DEM model, it is imperative to understand the mechanics of parallel bonds and how sphere's contact and bond stiffnesses interact. A step-by-step explanation is presented next.

- Spheres using the Linear contact model or the Linear Parallel-Bond contact model interact as springs in series or in parallel. This behavior can be expressed mathematically in the following form:

$$K = \begin{cases} \left(\sum_{i=1}^{n} \frac{1}{k^i}\right)^{-1} = \frac{k}{n} \quad \dots (Series) \\ \sum_{i=1}^{n} k^i = nk \quad \dots (Parallel) \end{cases}$$

- Spheres under the Linear contact model interact among themselves in series; however, spheres under the Linear-Parallel bond interact among themselves in parallel as previously shown in Figure 4.5. The equivalent stiffness due to parallel bonds and sphere contacts in a chain of spheres can be computed using the following equations, where n refers to the number of spheres in the chain:

$$K_{Parallel\ bond} = \left(\frac{A\bar{k}_n}{n}\right),\ K_{Ball\ contacts} = \left(\frac{k_n}{2n}\right)$$

- The overall stiffness of the chain of spheres is determined by adding the contribution of contact and bond stiffnesses (Itasca, 2015):

$$K = \left(\frac{A\bar{k}_n}{n}\right) + \left(\frac{k_n}{2n}\right)$$

- According to the documentation in PFC3D, the overall stiffness of a linear elastic member is identical to the young modulus of the material (E), its cross-sectional area (A), and its length (L) (Itasca, 2015):

$$K \equiv \frac{k_n}{2n} = \frac{\mathrm{EA}}{\mathrm{L}} \therefore k_n = \frac{2n \cdot EA}{L}$$

- The equivalent normal stiffness of parallel bond $(\bar{k}_n)$ can be obtained from substituting k_n into the equation for K:

$$\bar{k}_n = \left(K - \frac{k_n}{2n}\right) \cdot \frac{n}{A}$$

  It is important to note that K is obtained from physical testing at a 0.5% strain, while $k_n/2n$ is obtained from the material modulus of elasticity, and its initial cross-section and length.

- The shear modulus of this chain of spheres is approximated, by using the relationship between the elastic modulus, Poison's ration, and shear modulus for homogeneous isotropic materials.

$$G = \frac{E}{2 \cdot (1 + \nu)}$$

- According to the documentation in PFC3D, the bond shear stiffness of linear-parallel bonds is identical to the shear modulus of the segments that comprised the chain of spheres (Itasca, 2016):

$$\bar{k}_s \equiv \frac{G}{2 \cdot r}$$

The geogrid material and geometrical properties obtained from physical testing were used in conjunction with the equations presented previously to develop a numerical model for each geogrid type. Table 4.2. summarizes the multiaxial geogrid rib stiffness obtained from physical testing and the geometrical properties of the rib.

Table 4.2 Summary of geogrid material and geometrical parameters obtained from physical testing.

TX Type	δ @ 0.5%	F @ 0.5%	K @ 0.5%	A	L	E	v	G
	m	N	N/m	m^2	m	Pa	-	Pa
130S	1.75E-04	33.02	1.89E+05	1.28E-06	3.63E-02	5.16E+09	0.42	1.82E+09
140	1.85E-04	35.98	1.94E+05	1.30E-06	3.84E-02	5.55E+09	0.42	1.95E+09
190L	2.75E-04	124.05	4.51E+05	4.06E-06	5.33E-02	5.69E+09	0.42	2.00E+09

Although the cross-sectional area of the geogrid rib is rectangular, the geogrid DEM model was developed using a circular rib cross-sectional area. In order to model the geogrid as closely as possible to reality, the geometry of the cross-section area was changed to a circle, but its area value was not changed. Table 4.3. summarizes the geometrical properties of the multiaxial geogrid rib DEM model.

Table 4.3 Summary of multiaxial geogrid DEM model geometrical properties

TX Type	A m^2	Rib Radius m	Radius Mult. -	Rib Length m	No. Spheres (n) -
130S	1.28E-06	6.37E-04	1.00	0.0319	25
140	1.30E-06	6.44E-04	1.00	0.0386	30
190L	4.06E-06	1.14E-03	1.00	0.0546	24

By utilizing the physical material and geometrical properties, as well as the geometrical properties determined for the model, the micromechanical parameters to simulate the geogrid, such as the normal and shear contact and bond stiffnesses, were determined. Table 4.4. summarizes these parameters for all three geogrid types.

Table 4.4 Micromechanical parameters computed for modeling TX130S, TX140, and TX190L multiaxial geogrids.

TX Type	k_n N/m	k_S N/m	Bond k_n Pa/m	Bond k_S Pa/m
130S	9.06E+06	1.02E+07	1.48E+11	8.00E+09
140	1.13E+07	1.13E+07	1.49E+11	8.76E+09
190L	2.17E+07	2.17E+07	1.11E+11	9.53E+09

4.4.3 Calibration results

In order to calibrate the geogrid model and corroborate that its response agreed with the actual geogrid response, a single rib tensile test simulation was performed with PFC3D. A single geogrid rib from each geogrid type was modeled as a chain of spheres. Each rib model was subjected to a tensile force as show in Figure 4.13.

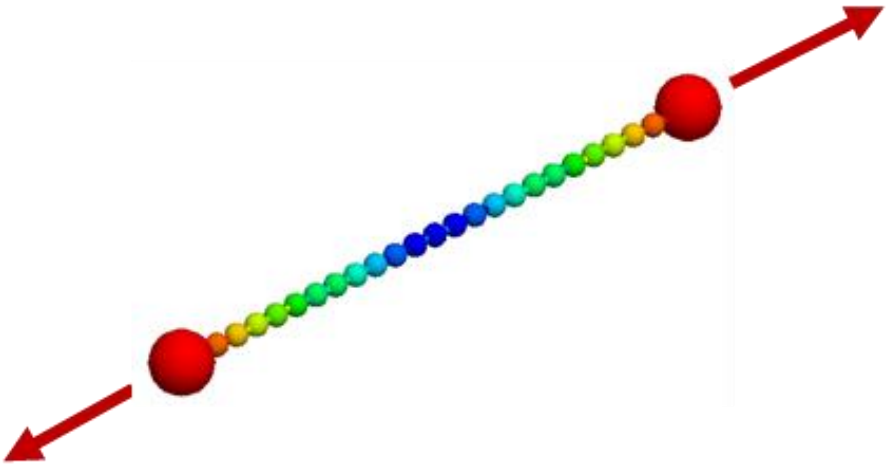

Figure 4.13 Single rib tensile test DEM simulation performed on a TX190L rib.

This tensile force was applied to the rib by specifying the velocity of the spheres in the extremities of the rib. This velocity was set to 0.005 m/s and pulled for 50,000 steps. The tensile force on the rib simulation was determine by adding the bond forces every 1,000 steps. The extension, or displacement of the extremities, of the rib was calculated by determining the position of one of the spheres at the rib extremity and calculating the movement every 1,000 steps with respect to its initial position. This displacement was multiplied by two, in order to take into consideration the extension of the other half of the rib. The single rib extension simulations against experimental data for TX130S, TX140, and TX190L are presented in Figure 4.14., Figure 4.15, and Figure 4.16, respectively.

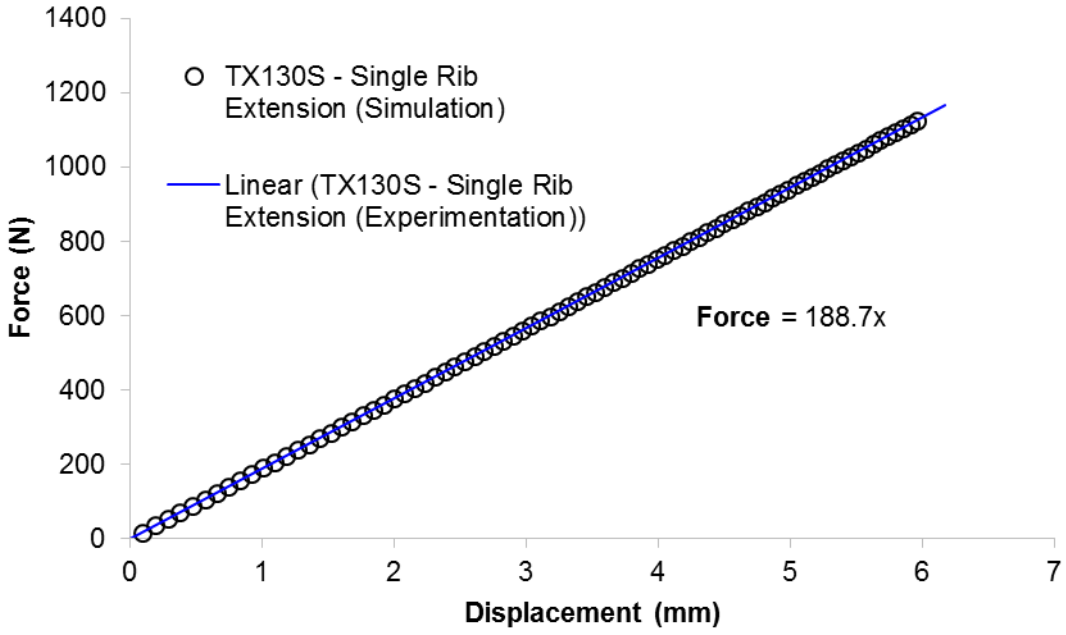

Figure 4.14 Single rib extension simulation and experimental data for TX130S calibration

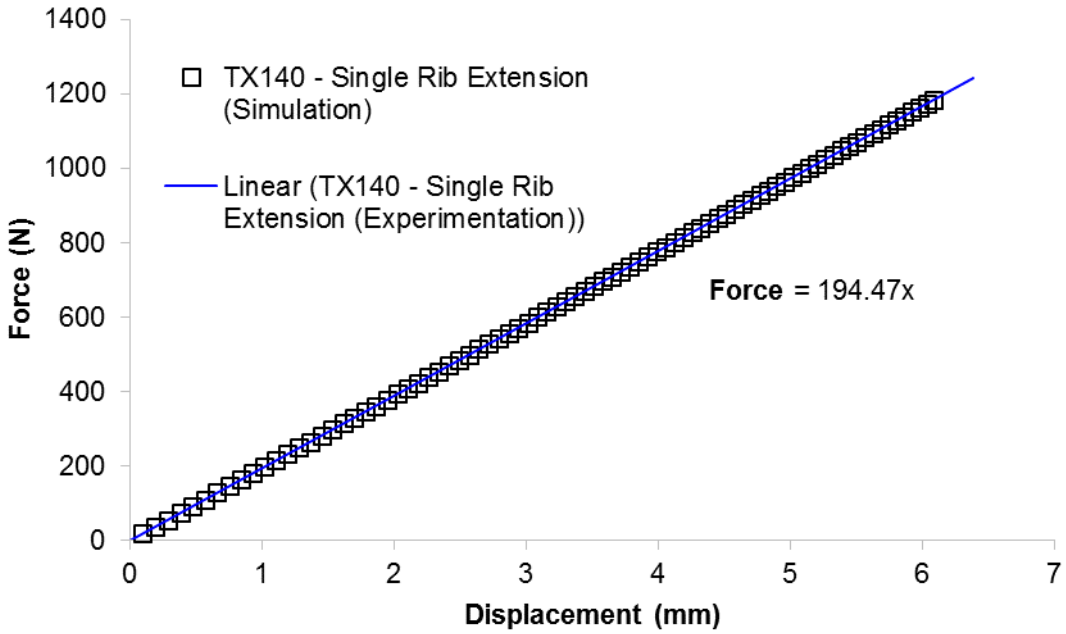

Figure 4.15 Single rib extension simulation and experimental data for TX140 calibration

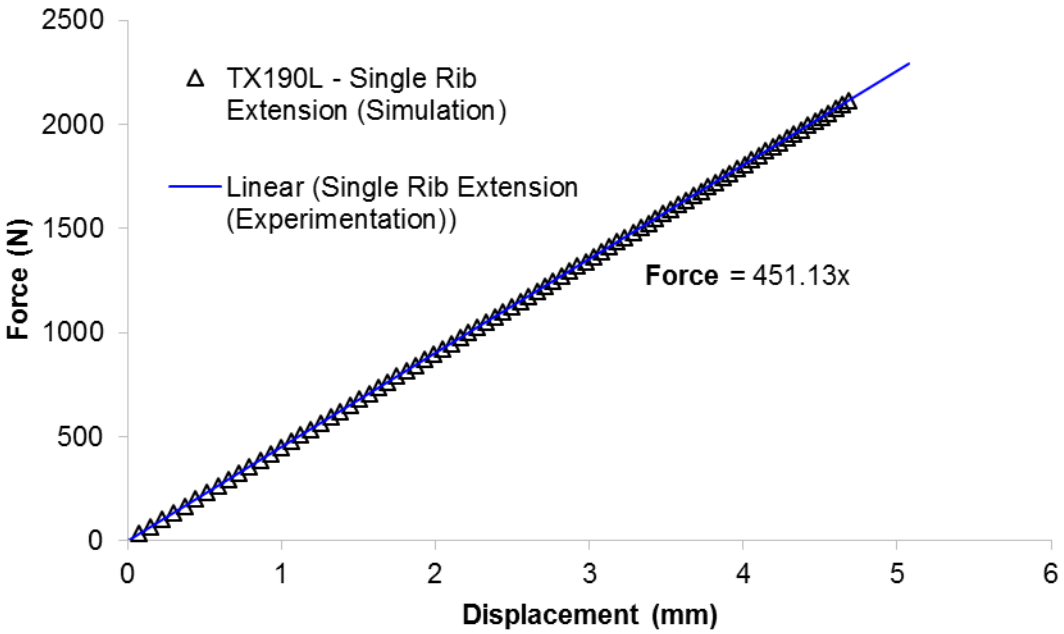

Figure 4.16 Single rib extension simulation and experimental data for TX190L calibration

As can be observed, the DEM model of the geogrid ribs represented the actual geogrid rib behavior accurately.

4.4.4 Flexural rigidity of geogrids

Multiple studies have demonstrated that geogrid stiffness is an essential parameter to obtain a favorable load-deformation response at the surface of geogrid-reinforced unpaved roads. Load-deformation response of single geogrid ribs is a practical indicator of geogrid stiffness; however, this response only evaluates in-plane stiffness of the material. Geogrid out-of-plane stiffness, or flexural rigidity, is another geogrid property, which evaluates the out-of-plane deformation of geogrids under their own mass, when these are extended over the edge of a planar surface. This test is performed following the guidelines of ASTM D7748. Although this test is only performed on geogrids for

manufacturing quality control purposes, it is a useful qualitative indicator to assess the DEM model of multiaxial geogrids.

In order to demonstrate the usefulness of this test for geogrid modeling, a compressive force is applied to a TX190L physical specimen as well as a numerical specimen as illustrated in Figure 4.17.

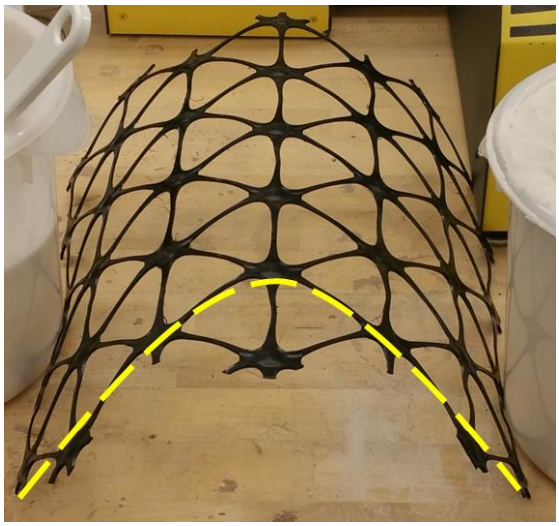

(a).

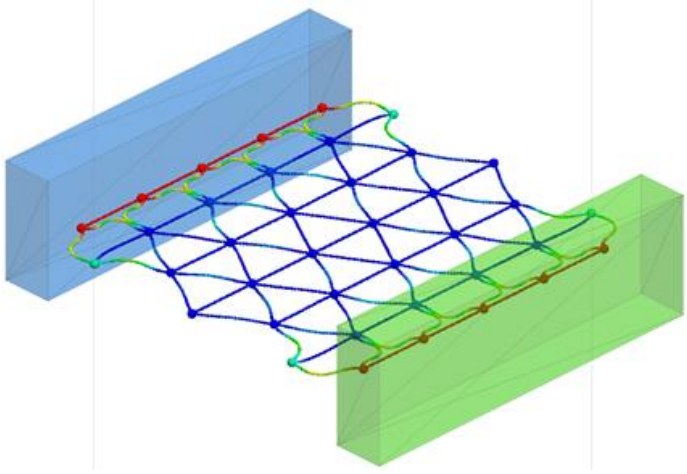

(b).

Figure 4.17 (a).TX190L specimen under compressive forces, (b). TX190L DEM specimen under compressive forces

As soon as the physical specimen is compressed, it tends to ach and remain in that position; however, as soon as the numerical model is compressed, an in-plane deformation occurs, and no aching occurs. This qualitative test evidences that it is necessary to calibrate the flexural rigidity of the geogrid model, in order to obtain a realistic geogrid response under compression.

In order to calibrate the flexural rigidity of the geogrid, it is necessary to understand the behavior of the physical model. Geogrid ribs under compressive forces can be envisioned as slender columns pinned at the geogrid joints, which buckle once the compressive forces are high enough; however, as soon as this compressive force is released, these columns return to their original shape. It has been well stablished that the buckling of columns is driven by the flexural rigidity of the member, which depends on the material properties of this one, such as the modulus of elasticity (E), and its geometrical properties, such as the second moment of area (moment of inertia) (I) (Gere and Goodno, 2009).

The behavior of geogrid ribs under compression can be explained by column bucking, so in order to modify the behavior of the geogrid model, the flexural rigidity has to be changed. Since the modulus of elasticity of the geogrid cannot be modified due to the fact that all three multiaxial geogrid specimens are manufactured using polypropylene, the only variable that can be modified is the second moment of area.

The second moment of area is a geometrical property of the member as described before, and it depends on the cross-sectional area shape. Previous studies have shown that it is necessary to model the geometry of the geogrid precisely in order to have a more realistic deformation; however, these models do so by increasing the amount of spheres

on the rib cross-section, which in return decreases the time step significantly and slows down the simulation. Due to this drawback, a different approach has to be taken in order to solve this issue.

In order to modify the cross-sectional area of the geogrid without compromising the efficiency of the model, or modifying the modulus of elasticity of the material, the moment of inertia was artificially increased by adjusting the cross-sectional area of the bond using the PFC parameter radius multiplier(λ). The function of the radius multiplier is to increase, or decrease, the radius of the parallel-bond, to simulate instances where the cementitious material bonding two particles is larger than the radius of the particle.

The implementation of this method increases the flexural rigidity of the geogrid, but does not change its axial behavior, because the new parallel-bond radius is used to determine the contact normal stiffness. As the radius multiplier increases, the bond normal stiffness decreases and the single rib tensile extension behavior remains unchanged.

In order to calibrate the second moment of area of the DEM model to the second moment of area of the actual geogrid specimen, the second moment of area of the geogrid specimen was determined, and from this, the radius multiplier required to obtain an equivalent radius for the DEM model cross-section was determined. The equations used to compute the second moment of area of the geogrid and the model are presented in Figure 4.18. The results for the second moment of area of the physical geogrid and the DEM model in the x and y axis are presented in Table 4.5., Table 4.6., respectively. The radius multiplier required to obtain an equivalent cross-sectional radius for the TX190L model is presented in Table 4.7.

$$I_x = \frac{bh^3}{12} \; ; \; I_y = \frac{hb^3}{12}$$

$$I_r = \frac{\pi}{4} r^4$$

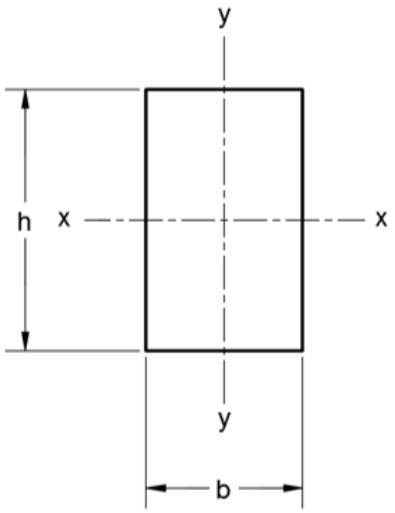

(a)

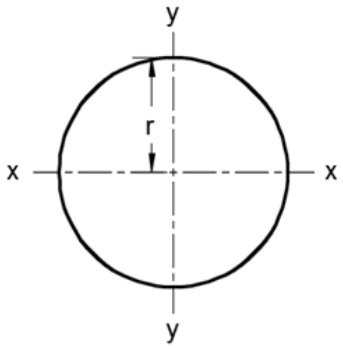

(b).

Figure 4.18 Second moment of area equations for (a). geogrid specimen and (b).DEM model

Table 4.5 Flexural rigidity of TX190L.

TriAx 190L						
b m	h m	I_x m^4	I_y m^4	E pa	EI_x $N\text{-}m^2$	EI_y $N\text{-}m^2$
1.4E-03	2.8E-03	2.7E-12	7.0E-13	5.78E+09	1.6E-02	4.04E-03

Table 4.6 Flexural rigidity of DEM model of TX190L.

TriAx 190L - DEM Model					
r m	I_x m^4	I_y m^4	E pa	EI_x $N\text{-}m^2$	EI_y $N\text{-}m^2$
1.14E-03	1.31E-12	1.31E-12	6.96E+09	9.12E-03	9.12E-03

Table 4.7 Radius multiplier required for an equivalent second moment between the actual geogrid and the geogrid DEM model.

Radius Multiplyier			
rx	ry	r_mul x	r_mul y
m	m	-	-
1.30E-03	9.27E-04	1.14	0.82

Column buckling occurs on the axis with the smallest second moment of area; therefore, a single geogrid rib will buckle on the y-y axis (in-plane). However, by looking at the actual deformation of the geogrid, it can be observed that the buckling of multiple braced geogrid ribs occurs in the x-x axis (out of plane). This behavior occurs due to the fact that a complete geogrid specimen does not act as a single column, but instead as a group of braced beams, due to the fact that single ribs are jointed together and these extend in all directions at 60^{o} from each other. Due to this behavior, the radius multiplier (λ) for the second moment of area in the x-x axis is used to scale up the cross-sectional area of the geogrid DEM model.

To assess the increment of the geogrid's flexural rigidity due to the implementation of the radius multiplier on the parallel-bond, a DEM simulation to qualitatively determine the flexural rigidity of geogrids as described in ASTM D7748 was performed. To determine the amount of geogrid hexagons required for the geogrid specimen to deflect by 41.5^{o}, four trials to compute the flexural rigidity of TX190L were performed as seen in Figure 4.19. The results from this test are summarized in Table 4.8.

Figure 4.19 Flexural rigidity evaluation of TX190L based on ASTM D7748

Table 4.8 Summary of flexural rigidity of TX190L

Trials	No. Overganging Hexagons	Length Overhanging cm	Flexural Rigidity mg-cm
1	3	42	2.44E+06
2	3	42	2.44E+06
3	4	56	5.79E+06
4	4	56	5.79E+06
Average	3.5	49	4.12E+06

The DEM model to test the flexural rigidity of multiaxial geogrid consisted of a specimen, which was made of four hexagons, and two boxes made from six wall elements. The first hexagon of the geogrid was placed between the two boxes and allowed to deform due to its weigh under gravity. The geogrid specimen was held between the two boxed,

as seen in Figure 4.20., by the friction developed between the walls and the specimen; however, this one was allowed to move in case its own weight pulled it out completely from between the two boxes.

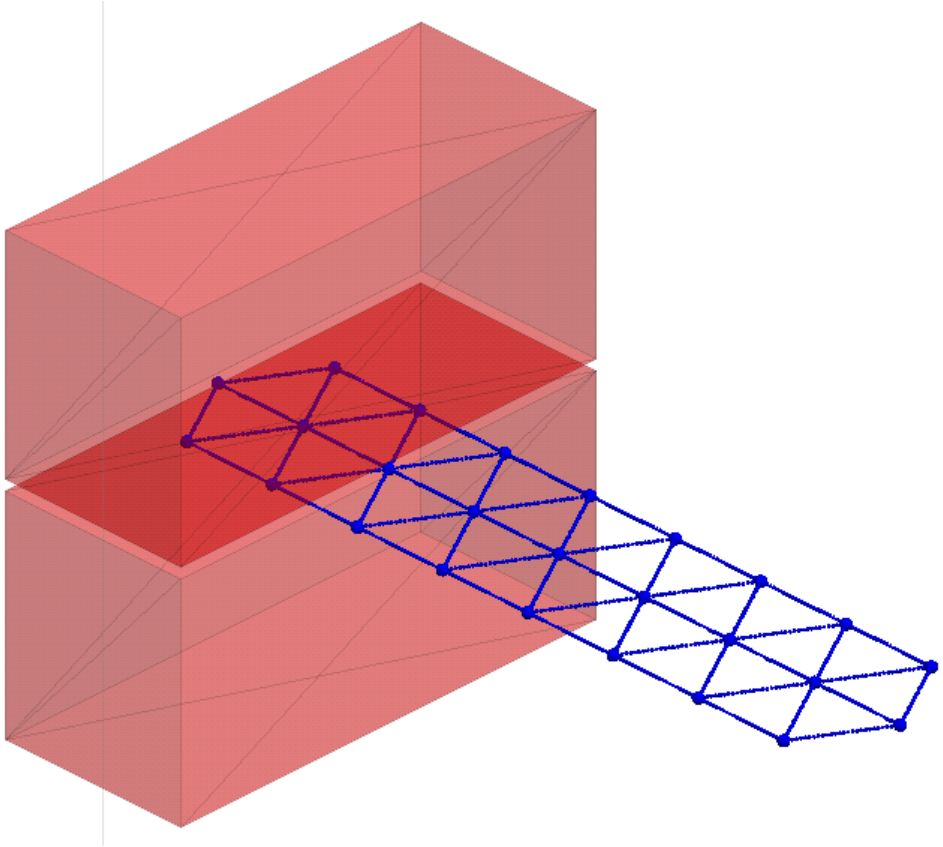

Figure 4.20 Flexural rigidity test simulation setup

Figure 4.21. presents the results from this simulation. As can be observed, the geogrid model deformed beyond the 41.5º line used in the physical test; therefore, this indicates that the geogrid model does not fully represent the physical geogrid flexural rigidity.

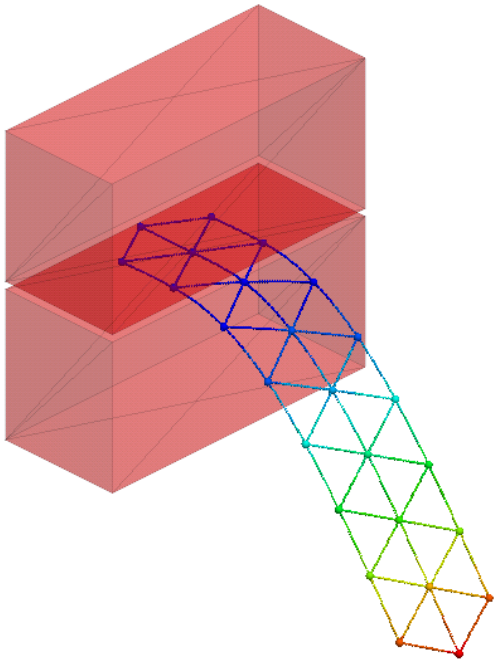

(a).

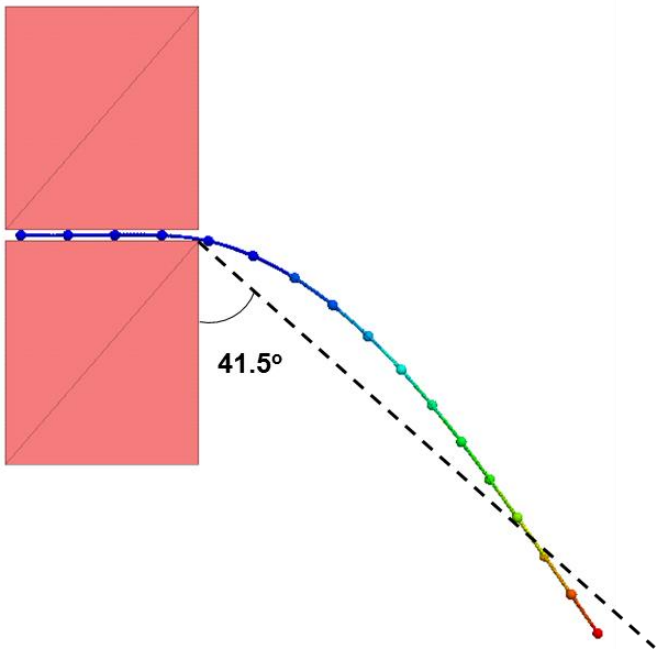

(b).

Figure 4.21 (a). Isometric and (b). Side view of flexural rigidity simulation results for a geogrid model with λ = 1.14

In order to gauge the radius multiplier value required to obtain the desire geogrid model flexural stiffness results, multiple simulations of geogrid compression were ran. The initial model state before deformation is presented in Figure 4.22.The deformation of the geogrid model for different radius multiplier cases are presented in Figure 4.23.

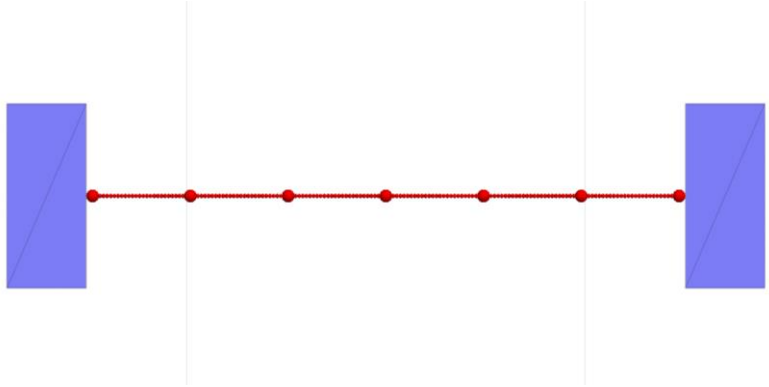

(a.)

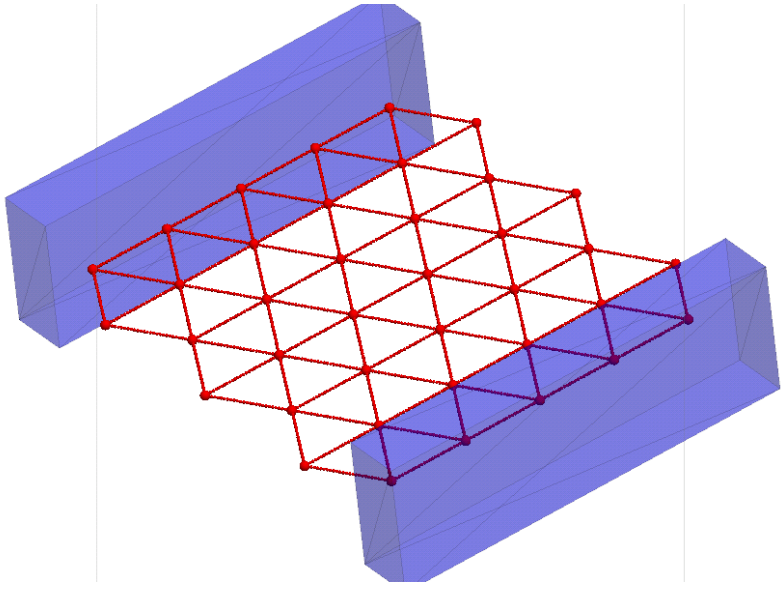

(b).

Figure 4.22 (a). Side and (b). Isometric view of TX190L at initial state before applying a compressing force

Radius multiplier	Front View	Isometric View
$\lambda = 1.14$		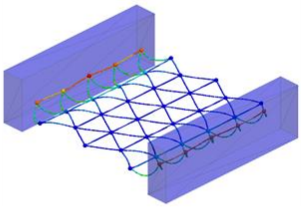
$\lambda = 5.0$	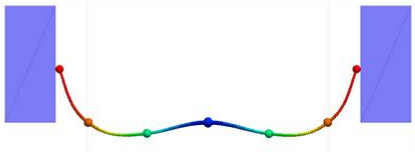	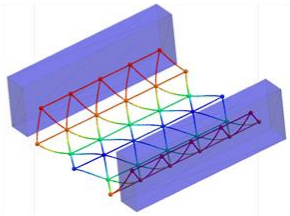
$\lambda = 10$	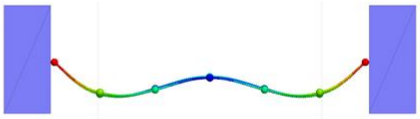	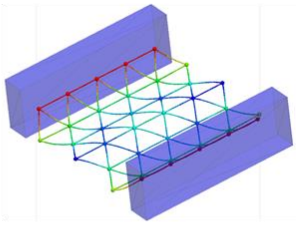
$\lambda = 15$		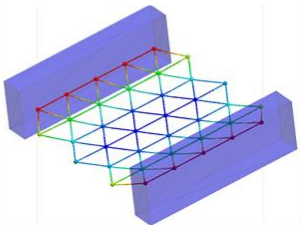
$\lambda = 20$		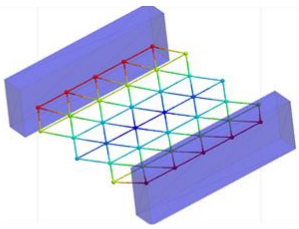
$\lambda = 25$		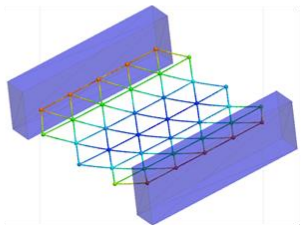

Figure 4.23 Geogrid compression deformation results for geogrid specimens modeled with different radius multiplier values after 50,000 steps.

These results illustrate that in order to obtain a geogrid with sufficient flexural rigidity, it is necessary to virtually increase the radius of the parallel bond by a factor between 15 and 25. The increment of the parallel bond radius by factors of this magnitude might seem unreasonable; however, as it was observed previously (Figure 4.23.) when this is the case, the geogrid deforms more realistically. Unfortunately, since it was not possible to establish a physical relationship to support the usage of radius multiplier values as high as 25, the geogrid model did not include them. The radius multiplier for the final geogrid specimen was kept at 1.14; even though, it did not entirely perform as was envisioned.

4.4.5 Geogrid geometry generation

In order to translate all the geogrid physical properties and geometry into PFC3D, an accurate sphere arrangement had to be created. It was important to verify that this geometrical arrangement of spheres was symmetric and did not have overlapping spheres. In order to achieve this goal, the following method was implemented.

4.4.5.1 *Geogrid D**E**M modeled using wall elements*

PFC3D has the capability to import a three-dimensional mesh developed from a drawing sketched in any CAD software and model it as a wall element. Each triangle in the mesh is represented as a wall element in PFC3D. This feature is used to simulate machinery where grains flow through, such as hoppers and mixing containers.

The idea to use this feature for geogrid modeling purposes was considered, since a wall element with the shape of a geogrid could behave as a continuum material, the usage of bonded particles would be avoided, and computational time could be reduced. A multiaxial geogrid hexagon 3D mesh was imported into PFC3D, in order to assess its

deformation capacity. Due to the fact that walls do not obey the laws of motion, it is not possible to develop a deformable model of a geogrid using a wall element. Figure 4.24. presents the mesh developed in CAD and the wall element modeled in PFC3D as it interacts with four clumps.

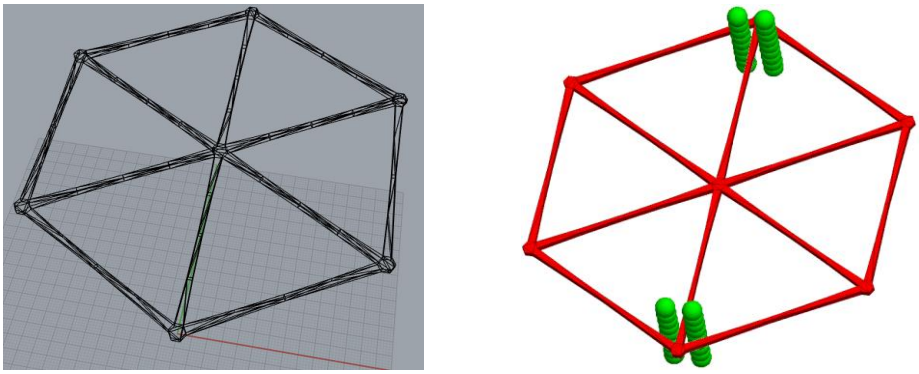

(a). **(b).**

Figure 4.24 (a). Geogrid mesh drawn in Rhinoceros (b)..Geogrid modeled as a wall in PFC3D

Although this geogrid process cannot be used to study the micromechanical interactions between geogrids and aggregate materials, it could be used to assess the aperture size compatibility between different types of geogrids and different aggregate gradations.

4.4.5.2 *Process to develop geogrid geometry and input for PFC3D*

The process to develop the geogrid geometry consisted on the following steps:

1. The geogrid geometry was drawn using a computer aided drafting (CAD) commercial software. The geogrid drawing included the thickness of the ribs and the junctions, as well as the overall geogrid size required to perform the final simulation.

2. The outline of the geogrid was populated with circles of a specific diameter. It was fundamental to make sure that the circles did not overlap.

3. The coordinates of the center of the circles was extracted using a routine built into the CAD software.

4. The coordinates were imported into MATLAB, where with the aid of a short script, the necessary syntax to create the spheres in PFC3D was develop.

5. Finally, this syntax was imported into PFC and the specimen was created.

Figure 4.25. presents the CAD drawing and the PFC3D model developed from it.

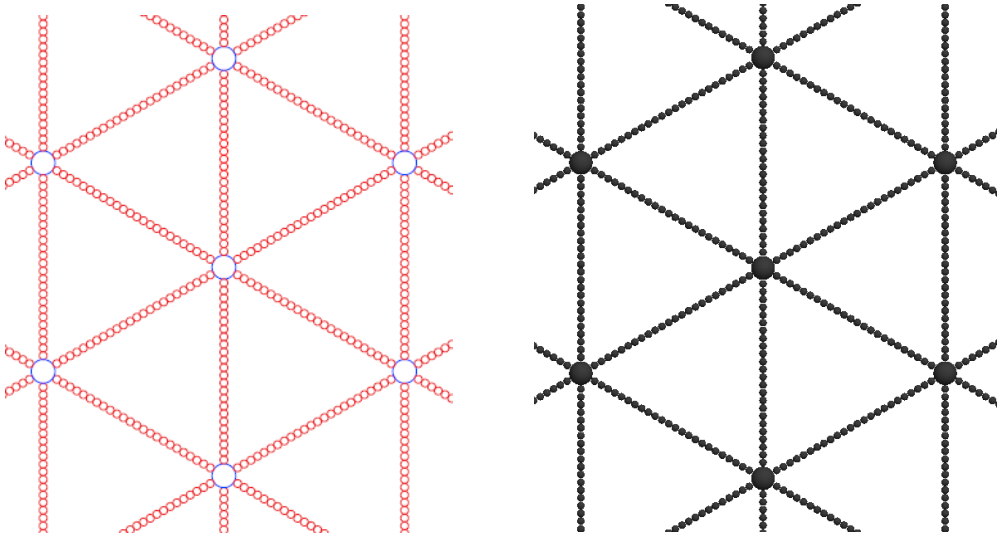

(a). **(b).**

Figure 4.25 (a). Geogrid CAD drawing (b). Geogrid PFC3D model visualization

The final visualization of the one of the geogrid models (TX190L) in PFC3D is presented in Figure 4.26.

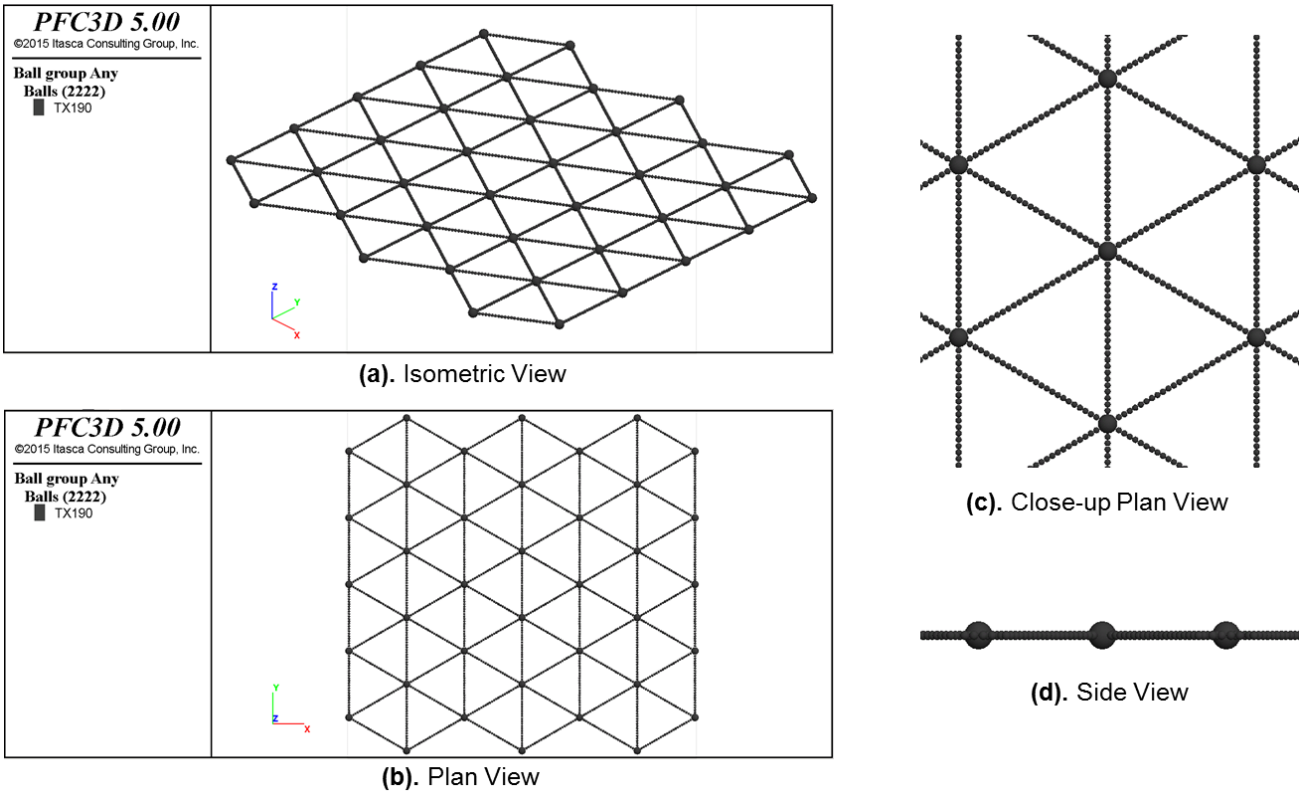

Figure 4.26 TX190L DEM model visualized in PFC3D

The overall number of spheres per multiaxial geogrid specimen DEM model are presented in Table 4.9.

Table 4.9 Summary of the number of spheres per multiaxial geogrid specimen.

TX Type	Total Number of Spheres per DEM specimen
130S	7,065
140	6,474
190L	2,222

4.5 Conclusions

This chapter presented the procedure by which DEM models for TX130S, TX140, and TX190L were developed. These models were calibrated against data obtained from single rib tensile tests, and it was noticed that the simulation results closely replicated the experimental results. The DEM models developed for TX130S, TX140, and TX190L consisted of 7,065, 6,475, and 2,222 spheres respectively.

The parallel-bond contact method is a useful technique to develop geogrid models in DEM. The geogrid model closely behaves like actual geogrids, and provides results representative to reality, as long as the quality of the micromechanical parameters assigned to the spheres and parallel bonds is high. In order to obtain high quality micromechanical parameters, it is necessary to perform multiple laboratory procedures, so the behavior of the geogrid model can be quantitatively and qualitatively calibrated against the actual geogrid.

It was noted that the geogrid models developed in this chapter fell short in simulating the response of the out-of-plane geogrid stiffness. An attempt to improve this behavior was made; however, it was not possible to achieve an optimum response. Although it is clear that the out-of-plane stiffness of the geogrid can be closely simulated by increasing the radius multiplier (λ) of the parallel bond, a physical meaning to justify the usage of a radius multiplier between 15 and 25 was not found; therefore, for the presented simulations, a radius multiplier (λ) of 1.14 was used pending further studies.

Lastly, the modeling of geogrids as a wall element is possible in PFC3D, by utilizing a three-dimensional mesh. Although wall elements do not obey the laws of motion, cannot deform, and ultimately cannot represent the physical behavior of geogrids, these types of

models could be used to perform preliminary assessments to find the optimum aggregate gradation for each geogrid type. After those gradations are determined, the parallel-bond DEM model of geogrid can be implemented to observe the deformation of the geogrid and assess the geogrid/aggregate interaction when utilizing this type of gradation.

CHAPTER V: DEM SIMULATION OF CYCLIC LOAD TEST ON GEOGRID STABILIZED AND NON-STABILIZED BINARY MIXTURES

5.1 Introduction

In order to determine the optimum aggregate gradation for multiaxial geogrids utilizing DEM, it is necessary to simulate their behavior under similar traffic loading conditions as real unpaved roads with mechanically stabilized layers (MSL) do. In order to simulate these conditions, a DEM model of a cyclic loading test was developed in PFC3D. This model consists of a low strength subgrade layer simulated by a wall element, a 250 mm thick aggregate layer simulated as both spheres and clumps, a multiaxial geogrid layer simulated by parallel-bonded spheres in the shape of the geogrid layer, and a loading plate simulated as a 300 mm diameter circular clump. Four simulations were performed using this setup with two different types of geogrid stabilized and non-stabilized binary mixtures. For the simulations presented in this section, both binary mixtures consist of only spheres. The procedure to develop the cyclic loading setup and determine the binary mixtures used for this study, as well as the results of the four simulations are presented in this chapter.

5.2 Particle gradation

In order to obtain an aggregate gradation that exhibits the least deformation under traffic loading, it is necessary to specify a particle size distribution capable of developing a particle packing with a minimal amount of void space. The reduction in voids lowers the

amount of space available for particle rearrangement due to traffic loading, and enables optimum densification of the aggregate more rapidly. Multiple studies have focused on determining this optimum particle size distribution, and the necessary amount of each particle size to obtain this ideal packing. In this section the findings of several prior studies are summarized and used, to investigate the optimum aggregate gradation for multiaxial geogrids.

5.2.1 Previous studies

McGeary (1967) studied the packing of spherical metal shot of different diameters, and observed the densification of single, binary, ternary, and quaternary particle packings. The single particle packing exhibited the least amount of densification at 62.5%, while the quaternary particle packing exhibited the largest amount of densification at 95.1%. The study found that for binary mixtures the density of the particle arrangement increased as the ratio between the sizes of the particles increased. Furthermore, the study found that an effective packing was obtained with a particle diameter ratio of 1:7, and that the density of a binary mixture did not significantly increase as this ratio was further increased as shown in Figure 5.1. This behavior was attributed to the triangular pore path created by three closed-packed spheres, which hindered the capacity of particles to fit through this opening and reach a higher density. Finally, it was observed that for binary mixtures, 20% to 40% of small particles were present when the maximum density was achieved.

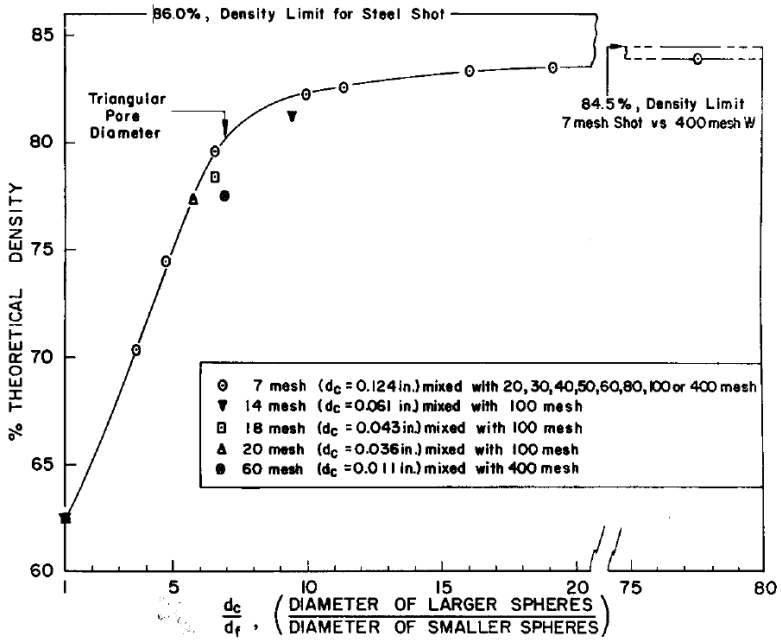

Figure 5.1 Maximum observed packing of binary mixtures of spheres (McGeary, 1961)

Fuggle et al. (2014) demonstrated experimentally and numerically that the void ratio of binary mixtures of sand change in a non-linear fashion as additional fine particles are included. Binary mixtures of sand with particle size ratios equal to 2.1, 2.8, and 6.1 were studied to find the minimum and maximum void ratios. A parameter called the Volume Reduction Ratio (VRR) was developed, in order isolate the effect of mixing two different sizes of particles, and allow a comparison of different particle size ratio mixtures starting at the same place. This parameter computed the ratio between the volume of a two-layered system to the volume of a homogeneous mixture for the same material mass. By utilizing VRR the impact of increasing the amount of finer particles was clearer. From the experimental results and the numerical simulation, it was observed that between 30% and 40% of fine particles by weight, the specimen achieved the lowest void ratio as shown in Figure 5.2.

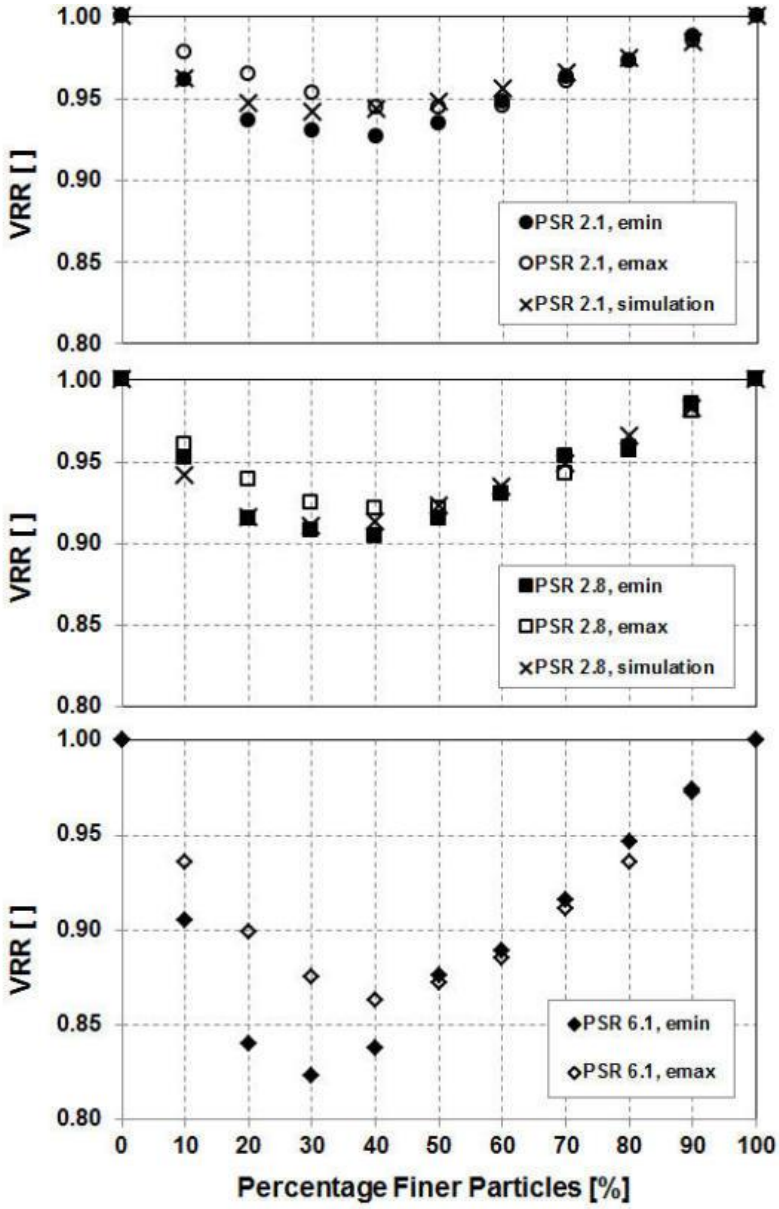

Figure 5.2 Volume reduction ratio for different particle size ratios (PSR). (Fuggle et al., 2014)

Xiao et al. (2012) studied different aggregate gradations in the state of Minnesota with the goal to understand how differences in aggregate gradations affected the behavior and performance of unbound aggregate base and subbase materials. The study focused on investigating the relationship between resilient modulus and the shear strength of the different aggregate gradations. The study found that the gravel-to-sand ratio was the

gradation parameter that influenced the shear strength behavior of aggregate materials the most. The study concluded that the aggregate specimens reached their maximum shear strength at a gravel-to-sand ratio equal to 1.5 by weight, due to the fact that at this ratio, void spaces around the coarse aggregate particles were completely filled by the smaller particles as observed in Figure 5.3.

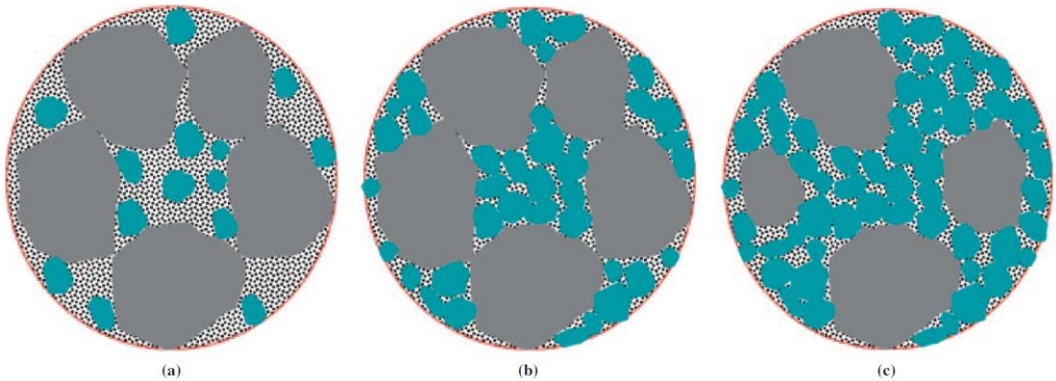

Figure 5.3 Packing states of gravel-sand-fines with different gravel-to-sand ratios: (a) Large, (b) optimum, and (c) small. (Xiao et. al, 2012)

From the three studies previously presented, three main conclusions can be drawn:

1. Binary mixtures with a sufficiently large particle size ratio (PRS) achieve the highest packing density.

2. A binary mixture with a percentage of fines equal to about 40% by weight achieve the lowest void ratio.

3. A binary mixture with a fines content equal to about 40% by weight influences the shear strength of the aggregate material the most.

$$\left(Gravel\ to\ sand\ ratio = 1.5 = \frac{60\%\ gravel}{40\%\ sand}\right)$$

From these three conclusions, a binary mixture that consists of 40% fines and 60% coarse particles, and that exhibits a PSR close to 7 would likely provide the best binary mixture for roadway applications.

5.2.2 Determination of particle gradation

The previous findings provide a useful framework to determine an optimum aggregate gradation for transportation applications; however, in order for a particle gradation with these characteristics to benefit from the stabilizing effects of geogrids, size compatibility must exist. Multiple studies have focused on determining the optimum geogrid aperture size to particle size ratio, and they have determined that the geogrid aperture size needs to be between 15% and 60% larger than the mean particle size of the aggregate specimen (Brown et al. 2007, Indraratna et al., 2012). Although these studies present conclusive results to support their findings with laboratory data, these results were obtained from studying geogrids with square aperture geometries, and their applicability to geogrids with triangular shaped apertures is unknown. In order to determine the optimum aggregate gradation for multiaxial geogrids, a similar approach was taken.

Since multiaxial geogrids have a triangular shaped apertures, in this study the diameter of the larger particle in the binary mixture was related to the length of the geogrid rib, instead of the aperture size. A binary mixture was used as the starting point to determine the optimum aggregate gradation for multiaxial geogrids. Two binary mixtures, one with a D_{Max} equal to 70% of the rib length, and the other one with a D_{Max} equal to

50% the rib length, were used for this purpose. These mixtures consisted of 60% coarse particles and 40% fine particles by weight as observed in Fuggle et al. (2014).

Although McGeary showed that binary mixtures with a PSR equal or larger than 7 achieve the best densification, it would require a tremendously large number of small particles to study this mixture. Performing numerical simulations on a binary mixture with large amounts of small particles using DEM is not practical and would require extensive time to yield results; therefore, it was determined that in order to find the optimum aggregate gradation for multiaxial geogrids, a PRS equal to 2.1 would be used as a starting point. The main approach of this binary mixture was to be able to attain a configuration within the aperture size as shown in Figure 5.4

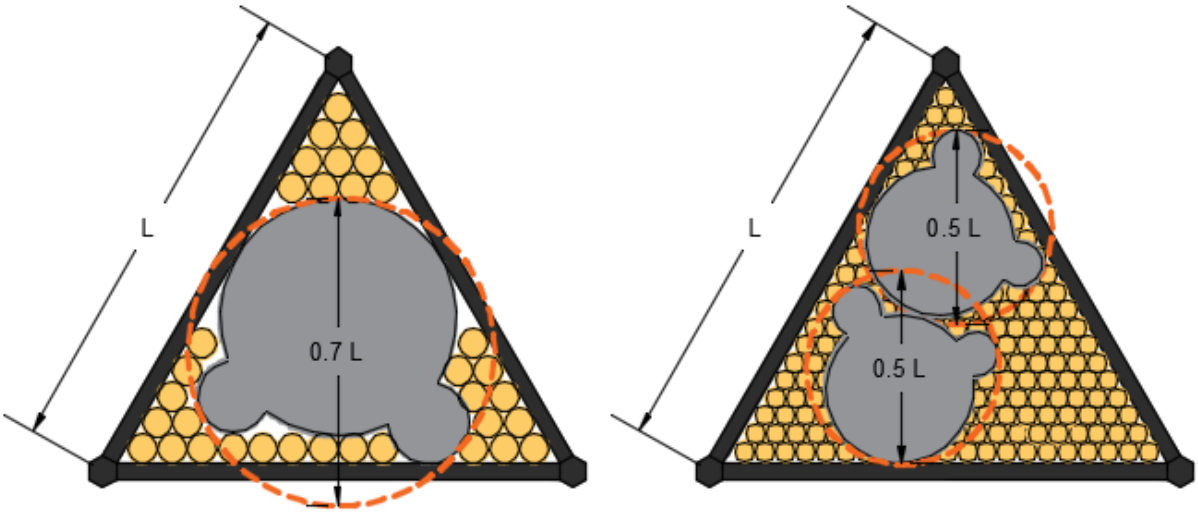

Figure 5.4 Idealized binary mixture configuration inside geogrid aperture in PFC

5.3 DEM Simulation of geogrid stabilized aggregate under cyclic loading

5.3.1 Cycling loading test setup

In order to assess the compatibility between a layer of multiaxial geogrid and each of the two different types of binary mixtures used in this study, simulated cyclic load tests were performed on a layer of spherical particles with and without a multiaxial geogrid layer. Figure 5.5. presents the cyclic loading setup in PFC3D.

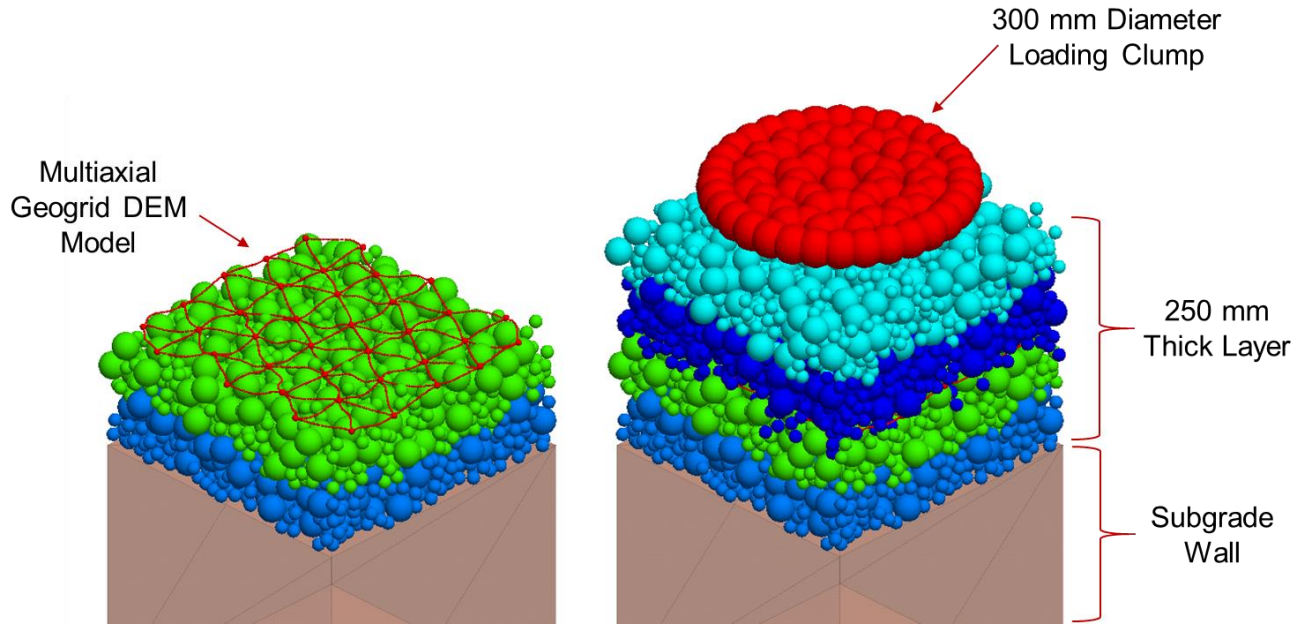

Figure 5.5 DEM model setup with spheres

This setup consisted of a wall element used as the subgrade of an unpaved road, a 250 mm thick binary mixture layer of spheres, a multiaxial geogrid specimen, and a 300 mm diameter loading clump plate. This setup was contained within a domain that utilized a periodic boundary condition (PBC). Each item in this test is explained below.

Low stiffness subgrade wall element:

Since the stabilization benefit of geogrids is more pronounced in weak subgrade layers as discussed in Chapter II, a wall element, with sufficiently low normal and shear stiffness, was used to model this behavior. A value equal to 4.9 x 10^6 N/m was used for these parameters, in order to simulate a subgrade layer with a modulus of elasticity equal to 25 MN/m^2, which is equivalent to a CBR value of 1.7, as presented by Chen and McDowell (2014).

Binary mixture layer:

The 250 mm binary mixture layer was filled with both previously discussed binary mixtures in Section 5.2. The details of the binary mixtures were presented in Section 5.3.1.

Multiaxial geogrid layer:

The multiaxial geogrid specimen used for this study consisted of 2,222 parallel bonded spheres, which generated a geogrid specimen with 42 triangular shaped apertures with a rib length equal to 60 mm. The micromechanical parameters used to develop this geogrid specimen were presented in Section 4.4.2.

Loading Clump:

The cyclic loading plate was modeled as an assembly of particles clumped together to simulate a circular plate with a 300 mm diameter. The application of the load to both stabilized and non-stabilized geogrid binary mixture layers consisted of allowing the loading clump to utilize its weight under a gravitational acceleration equal to 9.81 N/m^2 to apply the load. The clump was released from a distance equal to the diameter of the large particle in the binary mixture in order to mitigate dynamic effects. The clump had a density sufficiently high to apply a load equal to 50 kN. The clump was allowed to remain

at the surface of the specimen until the contact force under the loading clump reached 40 kN. Since the loading plate was 300 mm, at a contact force equal to 40 kN, it was assumed that the specimen had reached a loading stress equal to 556 kPa or 80 PSI, which is equivalent to the load applied by a H/HS-20 truck axel.

Domain under a Periodic Boundary Condition:

In order to avoid boundary effects in the model, a domain using a Periodic Boundary Condition (PBC) was utilized. When a PBC is utilized, the model assumes that the response of the surrounding material can be represented by identical elements, which behave in the same way as the elements contained inside the domain as can be observed in Figure 5.6. (O'Sullivan, 2011). The concept behind PBC is that as particles are being pushed out due to large contact forces, they exit the domain and reenter it through the opposite face of the domain as shown in Figure 5.7. This model practice is particularly useful to simulate large assemblies of particles such as in the study of unpaved roadways, since the constant confinement provided by the particles surrounding the domain is capable of simulating an infinitely large specimen (O'Sullivan, 2011).

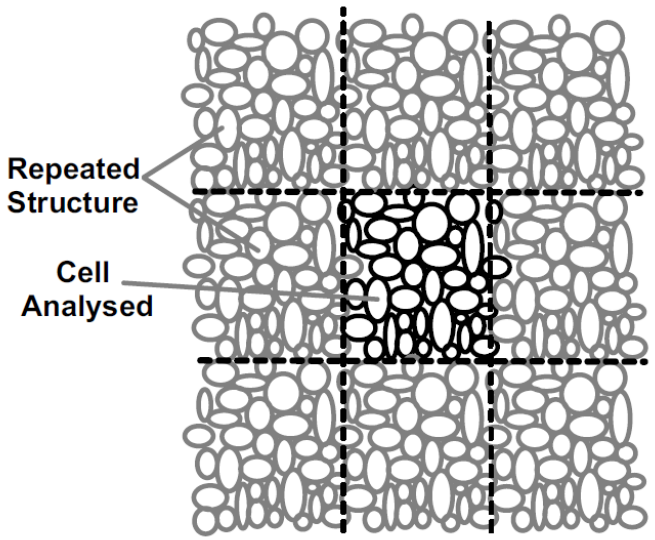

Figure 5.6 Graphical representation of a periodic boundary (O'Sullivan, 2011)

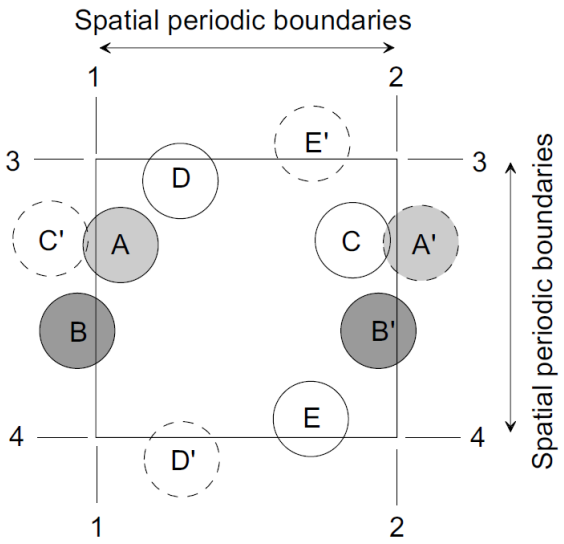

Figure 5.7 Particle movement in PBC (O'Sullivan, 2011)

5.3.2 Preparation and cyclic loading test of geogrid stabilized and non-stabilized binary mixtures

As mentioned before, two different binary mixtures were used for the determination of the optimum aggregate gradation for multiaxial geogrids. The first specimen, which will be referred to as binary mixture – 70%, consisted of particles of two different diameters with a PSR equal to 2.1. The D_{max} was equal to 70% of the rib length, while the D_{min} for this specimen was equal to 33% of the rib length. Since the TX190L specimen was used in all the simulations performed with this binary mixture, and its rib length is equal to 60 mm, the D_{Max} and the D_{Min} on this binary mixture was equal to 42 mm and 20 mm, respectively. This binary mixture consisted of 40% fine particles by weight and 60% coarse particles by weight, in order to reach the least void reduction ratio (VRR) possible; therefore, 1,732 particles with a diameter equal to 20 mm and 280 particles with a diameter equal to 40 mm were used.

The second specimen, which will be referred to as binary mixture – 50%, also consisted of particles of two different diameters with a PSR equal to 2.1. The D_{max} was equal to 50% of the rib length, while the D_{min} was equal to 23.8% of the rib length. Since the TX190L specimen was used with this binary mixture, the D_{max} and the D_{min} of this specimen were equal to 30 mm and 14.3 mm respectively. This binary mixture also aimed to achieve the least VRR, so 40% fine particles by weight and 60% coarse particles by weight were used. 2,752 particles with a diameter equal to 14.3 mm and 444 particles with a diameter equal to 30 mm were used for this simulation.

The sample was prepared by pouring the binary mixture in four lifts, in order to achieve an acceptable density, which was monitored by observing the porosity of each layer. After the first and second layers were poured, a surcharge clump consisting of sixty-six pebbles was used to densify the binary mixture. This procedure yield densification more rapidly than using a wall element. After the first two layers were compacted, the TX190L specimen was generated just above the second layer and dropped by gravity on top of the second layer. For the specimens without geogrid, this step was omitted. In order to generate lifts three and four, the coordinates of the spheres in layers one and two were extracted. The Z coordinate was offset by 135 mm and regenerated in the model. This approached was taken because it was noticed that once the geogrid was in place, the time step decreased significantly, so the process of dropping the particles and compacting them required longer times. After the particles were regenerated, the surcharge clump used to compact the specimen was placed above the forth layer and allowed to drop by gravity. After layers three and four came into contact with the geogrid, the surcharge clump was not removed until a target porosity was attained. Once the surcharge clump was removed, and the velocity of the particles remained at a velocity close to zero meters per second, the loading clump was generated just above the surface of the specimen.

This clump applied the load to the specimen through its mass and gravitational acceleration. The idea behind this loading mechanism was that as the contact forces created between the clump and the spheres increased due to the weight of the clump, the contact forces underneath the clump increased to the point where the overall clump contact force was equal to 40 kN. At this point the clump was positioned just above the surface of the specimen and dropped again. This loading cycle deformed the surface of the specimen, so at the end of every cycle the position of the center of the loading clump was recorded, in order to keep track of the surface deformation of the specimen. This procedure was repeated 500 times for each specimen. At the culmination of the test, the surface deformation of the geogrid stabilized and non-stabilized specimens were compared. The results are presented in the Section 5.4.

5.4 Results and discussion

The results obtained from the cyclic loading of geogrid stabilized and non-stabilized binary mixtures with different particle sizes are summarized in this section. Prior to presenting the results from these simulations, a schematic of each setup before and after cyclic loading application is presented. Figure 5.8 presents the initial conditions for both geogrid stabilized and non-stabilized binary mixture – 50%. Figure 5.9 presents the final conditions and surface deformations for both geogrid stabilized and non-stabilized binary mixture – 50% after of 500 loading cycles. Figure 5.10 presents the initial conditions for both geogrid stabilized and non-stabilized binary mixture – 70%. Lastly, Figure 5.11 presents the final conditions and surface deformations for both geogrid stabilized and non-stabilized binary mixture – 70% after of 500 loading cycles.

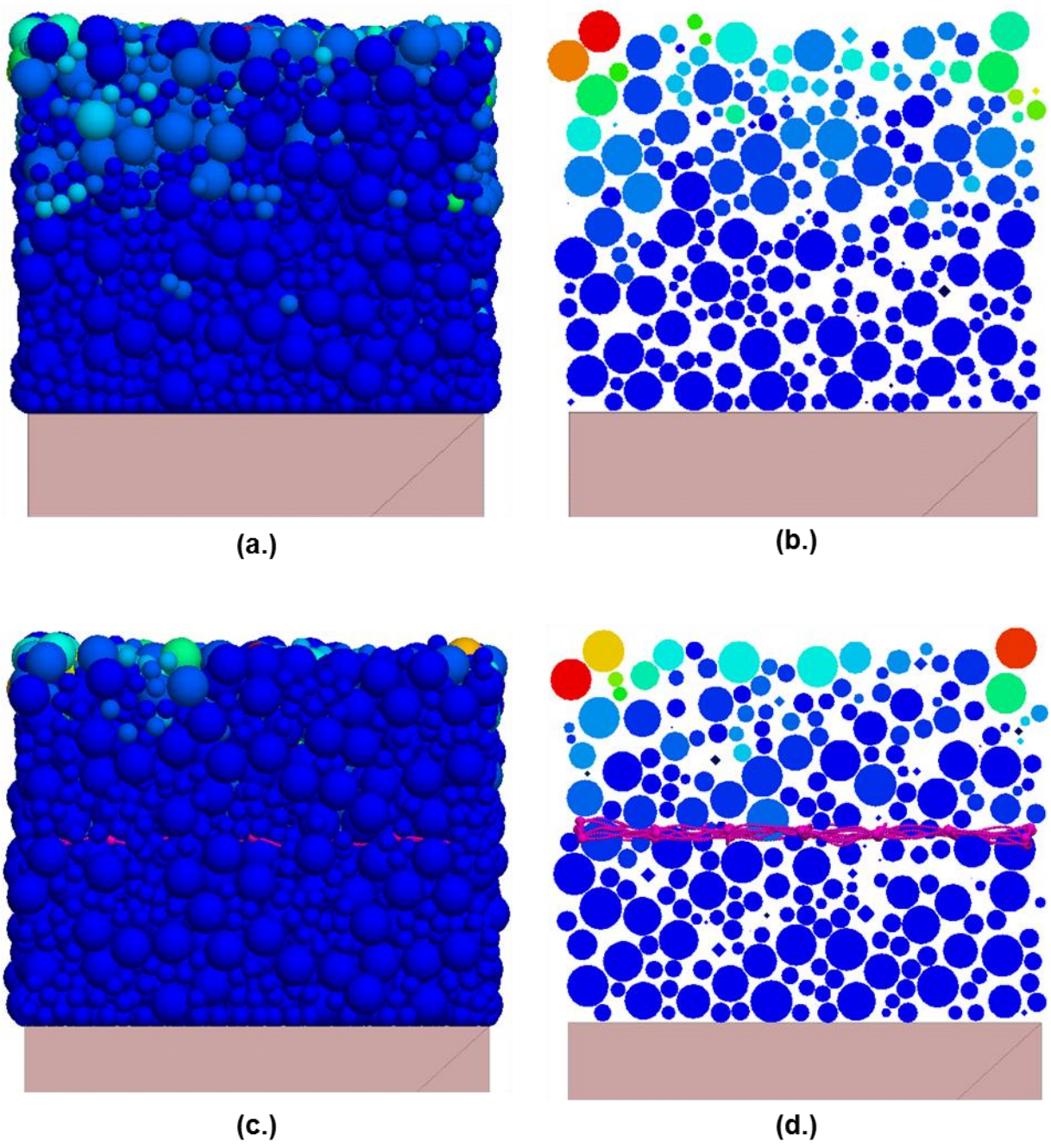

Figure 5.8 (a.) Initial condition for a non-stabilized binary mixture – 50% and its (b.) cross-section prior to cyclic load application (c.) Initial condition for a geogrid stabilized binary mixture – 50% and its (d.) cross-section prior to cyclical load application

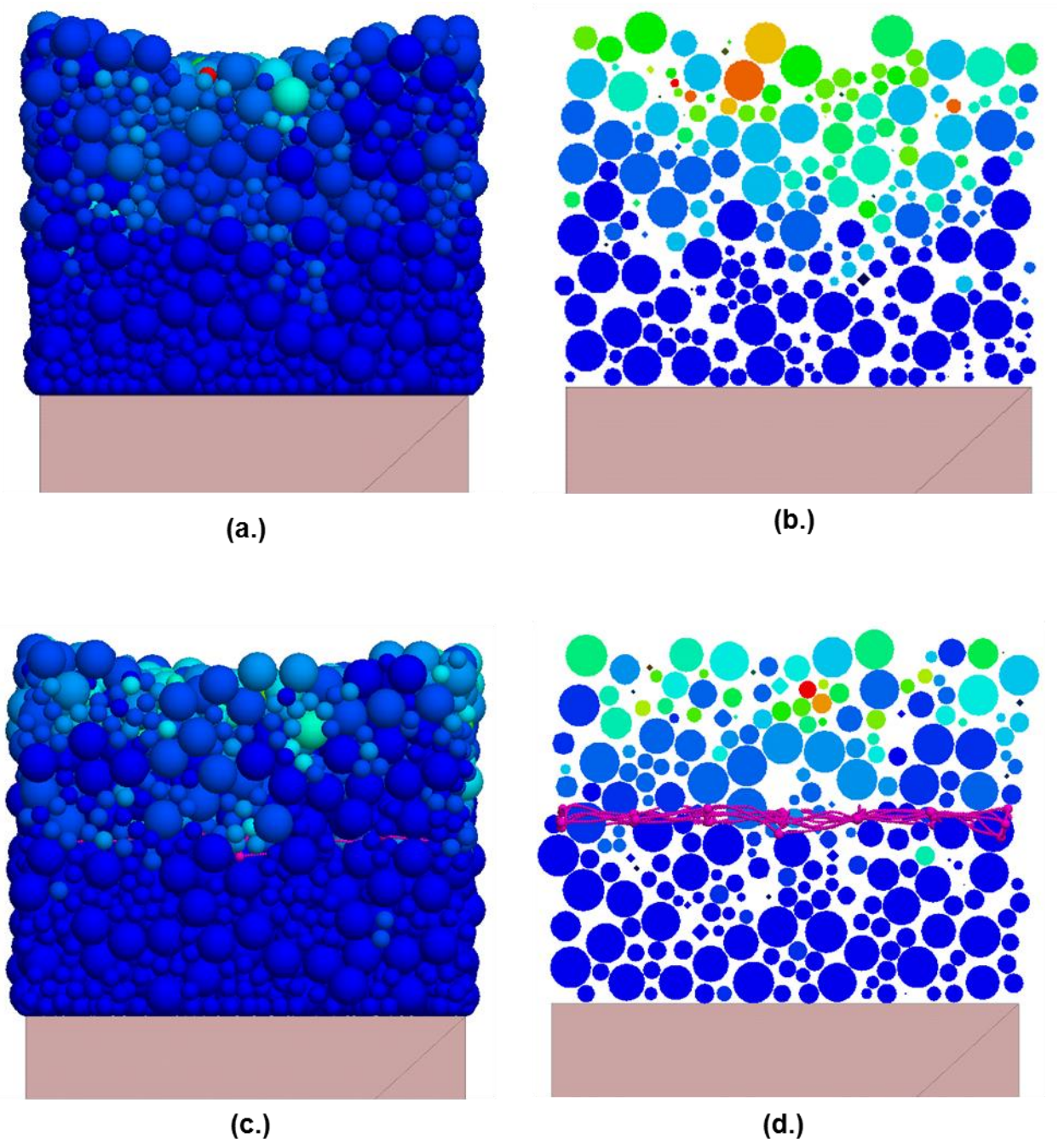

Figure 5.9 (a.) Final condition non-stabilized binary mixture – 50% and its (b.) cross-section after the application of 500 load cycles (c.) Final condition geogrid stabilized binary mixture – 50% and its (d.) cross-section after the application of 500 load cycles

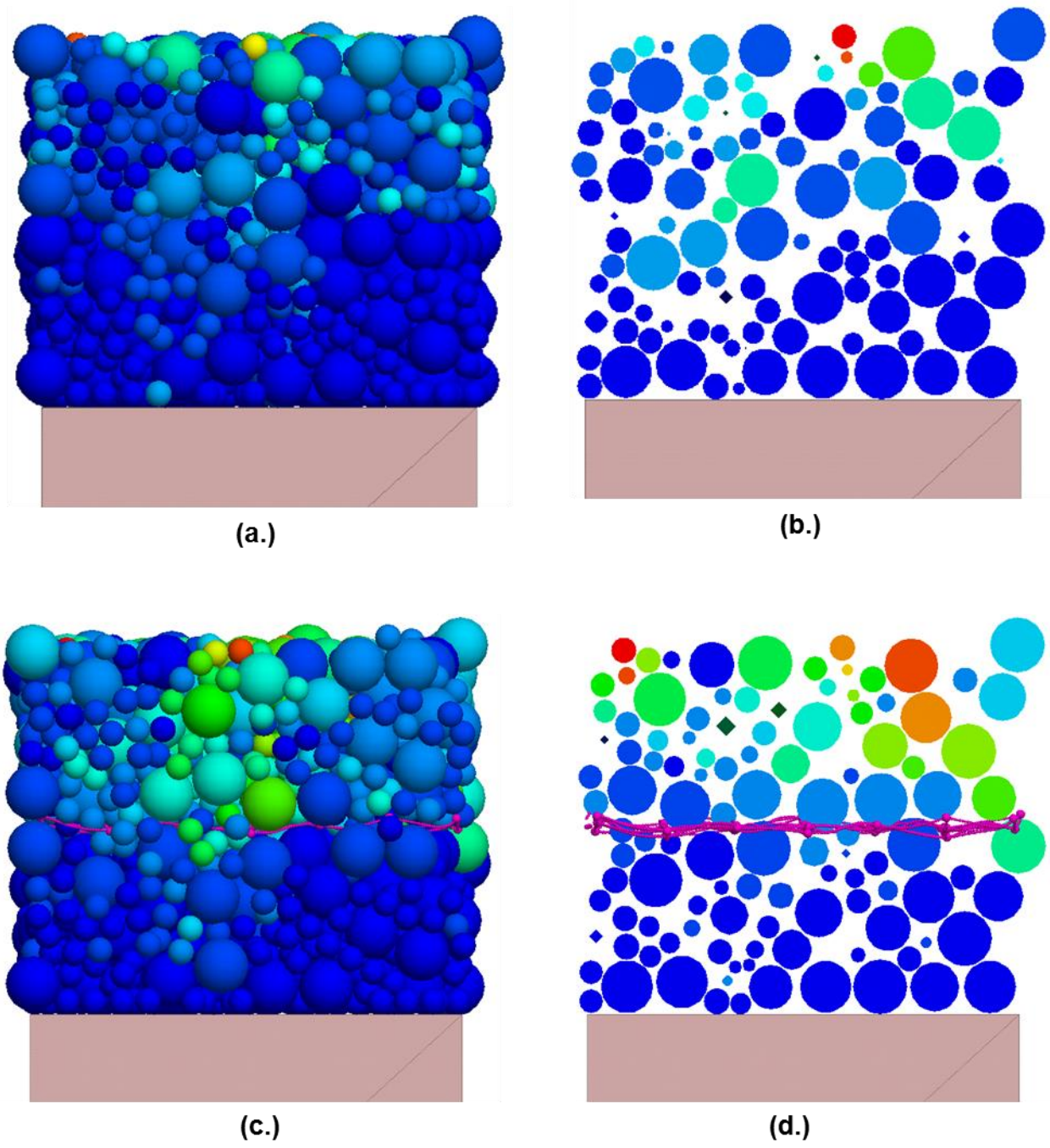

Figure 5.10 (a.) Initial condition for a non-stabilized binary mixture – 70% and its (b.) cross-section prior to cyclic load application (c.) Initial condition for a geogrid stabilized binary mixture – 70% and its (d.) cross-section prior to cyclical load application

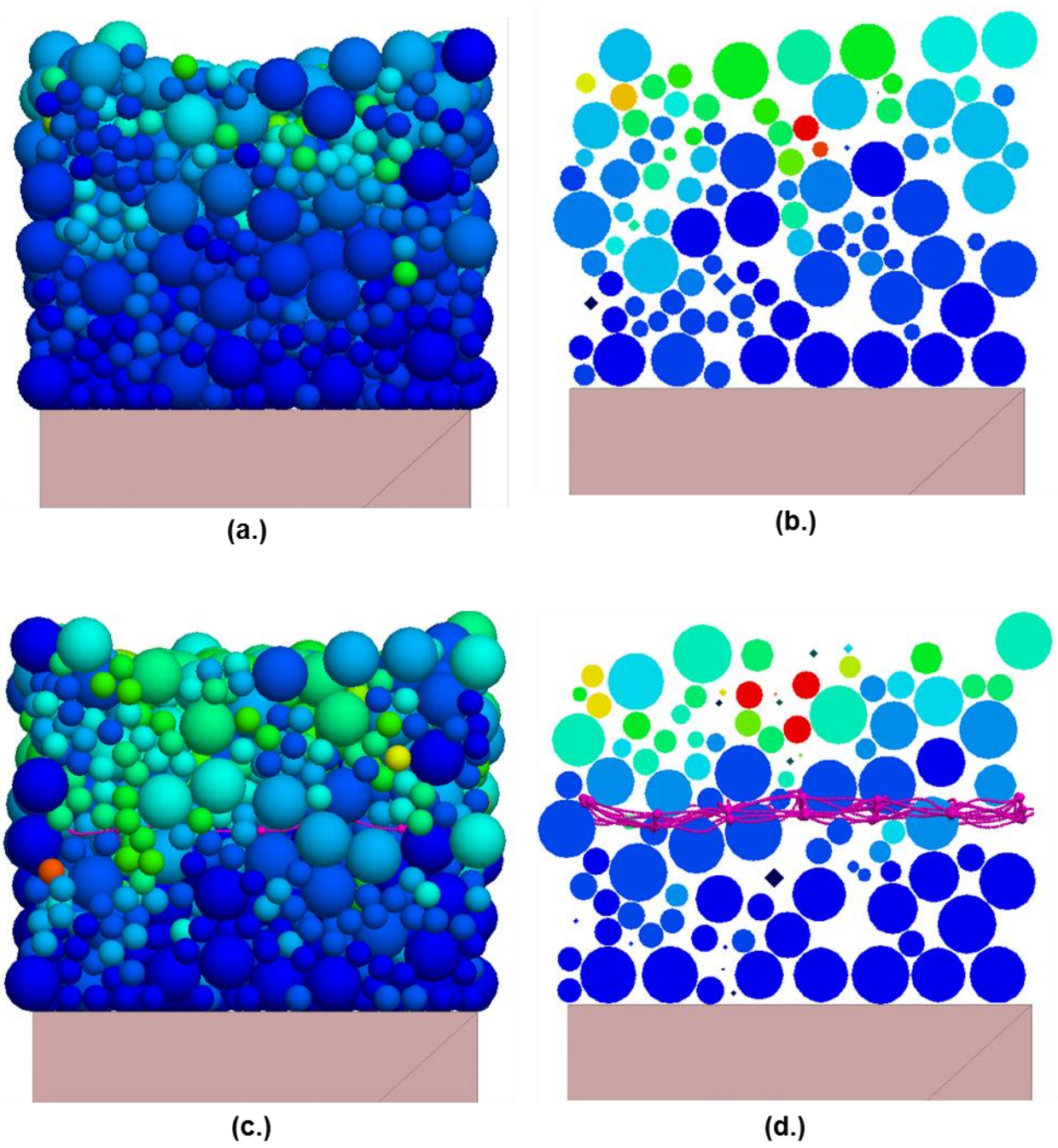

Figure 5.11 (a.) Final condition for a non-stabilized binary mixture – 70% and its (b.) cross-section after the application of 500 load cycles (c.) Final condition for a geogrid stabilized binary mixture – 70% and its (d.) cross-section after the application of 500 load cycles

Figure 5.12 presents the comparison between the surface displacements of a geogrid stabilized binary mixture – 50% and a non-stabilized one, after 500 loading cycles. The geogrid stabilized binary mixture exhibited a final surface deformation equal to 14.2 mm, while the non-stabilized one exhibited a final surface deformation equal to 21.2 mm. From this figure it can be observed that the geogrid stabilized binary mixture significantly outperformed the behavior of the non-stabilized one, since the latter one deformed 7.0 mm less than the former one. The initial deformation behavior of the geogrid stabilized and the non-stabilized binary mixtures exhibited similarities for the first 45 cycles; however, after this point was surpassed, the behavior between these two deviated dramatically. This dramatic change in behavior is attributed to the stabilization contribution of the geogrid layer.

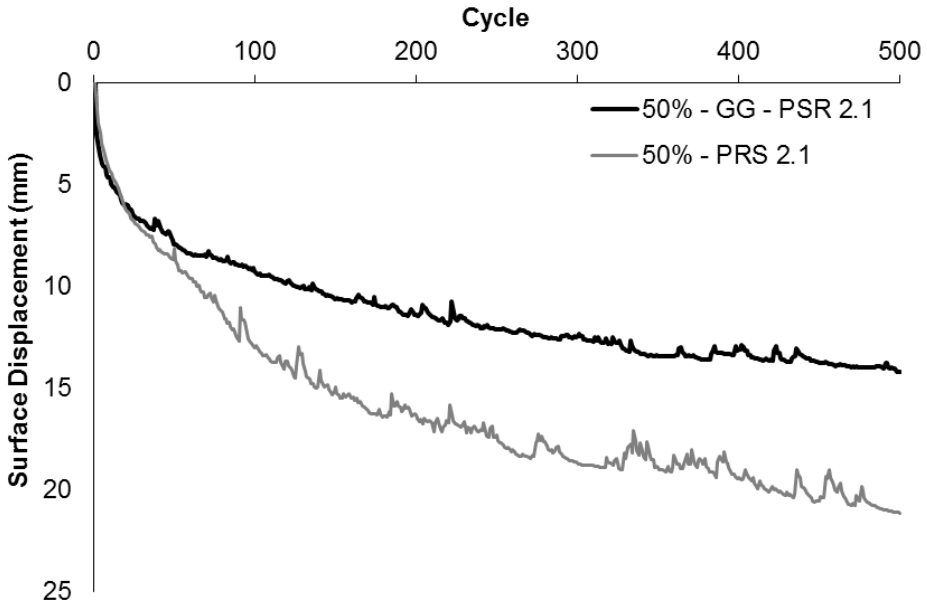

Figure 5.12 Surface displacement comparison between geogrid stabilized and non-stabilized binary mixtures – 50% after 500 loading cycles

Figure 5.13 presents the comparison between the surface displacements between a geogrid stabilized binary mixture – 70% and a non-stabilized one, after 500 loading cycles. The geogrid stabilized binary mixture exhibited a final surface deformation equal to 19.2 mm, while the non-stabilized one exhibited a final surface deformation equal to 18.2 mm. The difference in surface deformation between these two binary mixtures was negligible and it can be concluded that the stabilizing effect of a layer of geogrid was not observed.

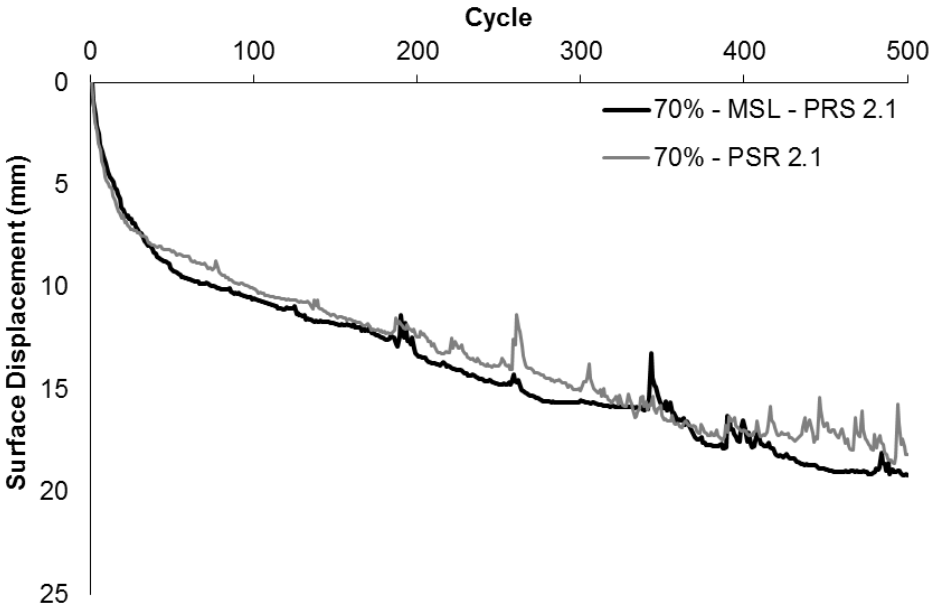

Figure 5.13 Surface displacement comparison between geogrid stabilized and non-stabilized binary mixture – 70% after 500 cycles

Since the only difference between both binary mixtures with geogrid layers is the diameter of the particles within each mixture, the difference in performance is attributed to the ability of the smaller particles in the binary mixture – 50% to interlock with the geogrid layer. In order to visually evaluate particle interlocking to validate this claim, both geogrid stabilized specimens were dissected at the geogrid location, and the interaction between

the particles and the geogrid was observed. The findings are presented in Figure 5.14 and Figure 5.15.

Figure 5.14 (a.) presents the interaction between a multiaxial geogrid layer and the layer of binary mixture – 50% underneath it, while Figure 5.14 (b.) presents the interaction between the same multiaxial geogrid layer and the binary mixture – 50% layer above this one, both at 500 loading cycles. Figure 5.15 (a. & b.) presents a similar scenario as before; however, for this case, a binary mixture – 70% is implemented.

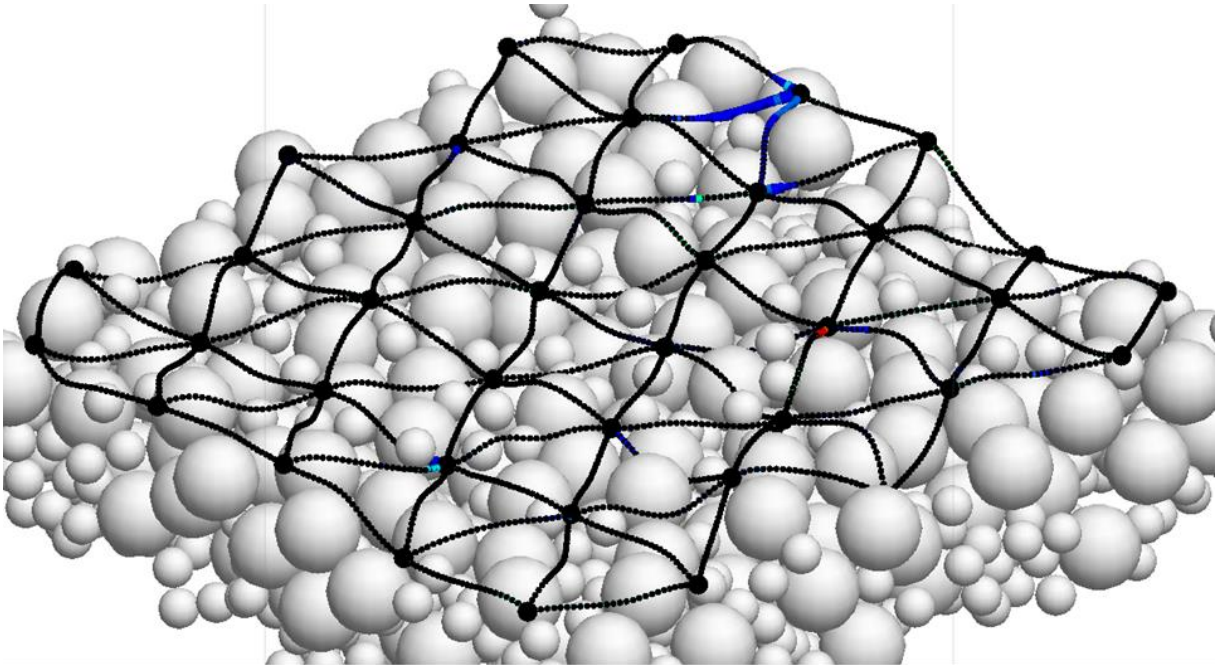

(a).

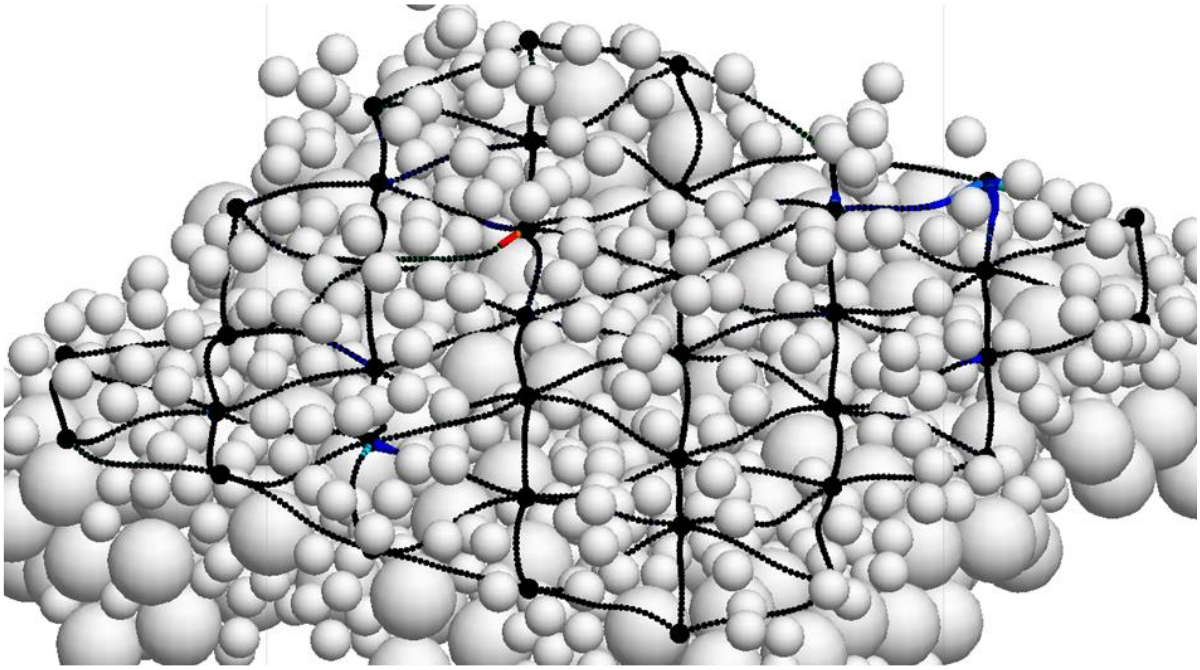

(b).

Figure 5.14 Interaction between (a.) lower and (b.) upper layer of binary mixture – 50% and multiaxial geogrid layer at 500 loading cycles

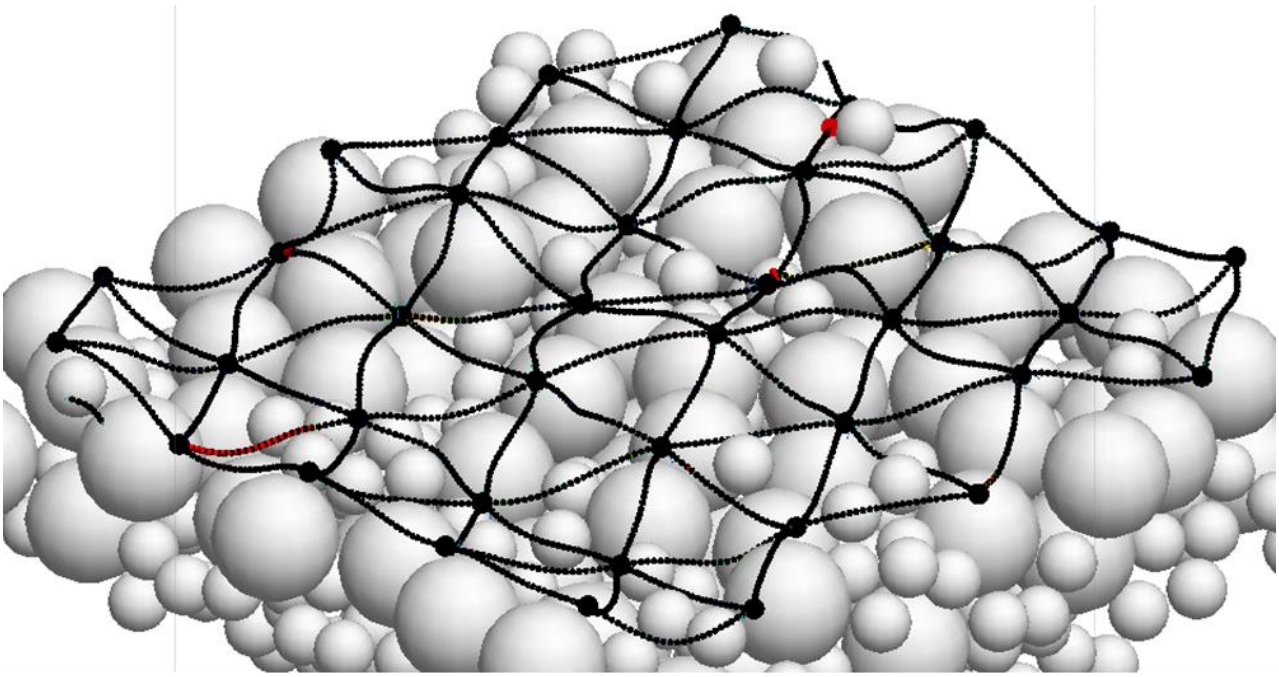

(a).

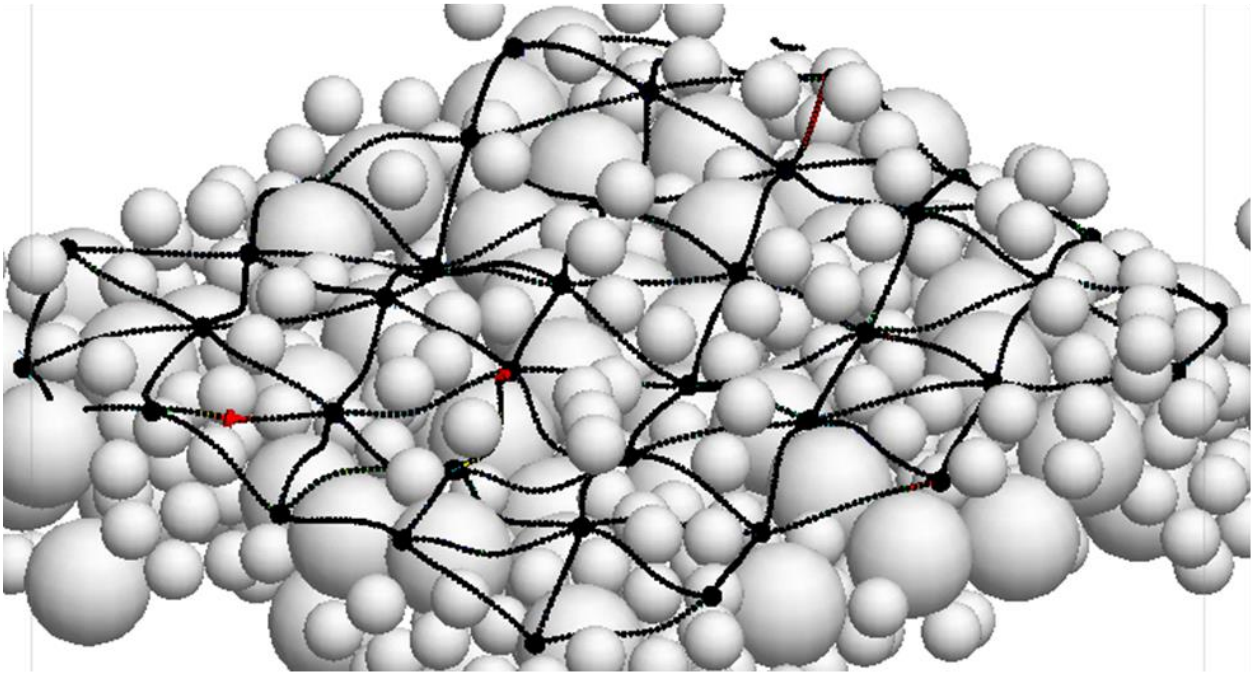

(b).

Figure 5.15 Interaction between (a.) lower and (b.) upper layer of binary mixture – 70% and multiaxial geogrid layer at 500 loading cycles

Multiple observations about the interlocking behavior between binary mixtures and multiaxial geogrids can be made from these two figures. The first observation is that multiple small particles of the binary mixture – 50% penetrate the geogrid layer and become interlocked within the geogrid apertures, as observed in Figure 5.14. As these particles penetrate, they become confined between the geogrid ribs and also interlocked among the large particles underneath the geogrid layer.

The second observation is that particle penetration through the geogrid layer was reduced when a binary mixture – 70% was utilized as observed in Figure 5.15. Not only interlocking was reduced, but it was also observed that particles, instead of penetrating through the geogrid aperture, remained resting on top of the geogrid ribs. This behavior appears to have pushed the geogrid layer on the direction of the force, because the geogrid experienced a convex deformation in this case. This type of deformation ultimately indicates that the geogrid is not providing any lateral confinement of the participles, and instead it is deforming with the entire specimen.

The interlocking mechanism developed between the particles of the binary mixture and the geogrid layer can be studied even further, by observing the parallel bond forces developed between the particles that comprise the geogrid layer as the specimen is loaded. As the particles interlock within the apertures of the geogrid, these parallel bond forces increase as they confine the particles laterally to resist lateral particle movement. These confining forces applied by the geogrid ribs create tension within the geogrid layer; however, when these forces are released, the parallel bonds contract to their initial state, and this mobilizes compressive forces within the geogrid ribs. The interlocking behavior between multiaxial geogrids and binary mixture particles can be assessed by the intensity of these parallel bond forces, and by the intensity of these tensile and compressive forces.

Figure 5.16 and Figure 5.17 present the development of parallel bond forces, and tensile and compressive forces, within the geogrid layer for binary mixtures – 50% and 70%, respectively.

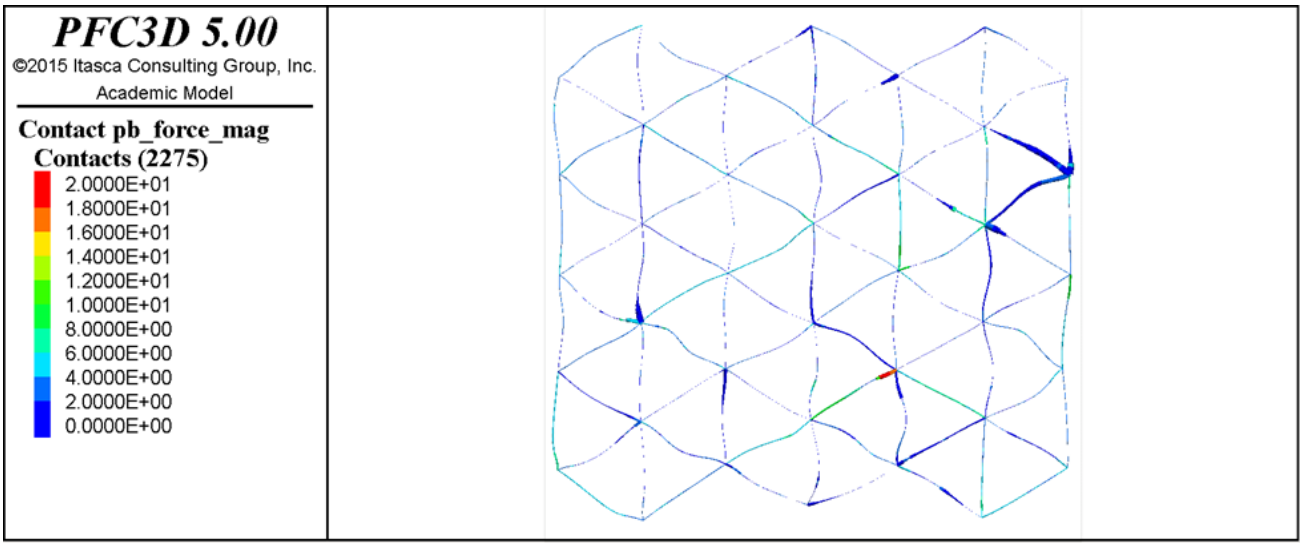

(a).

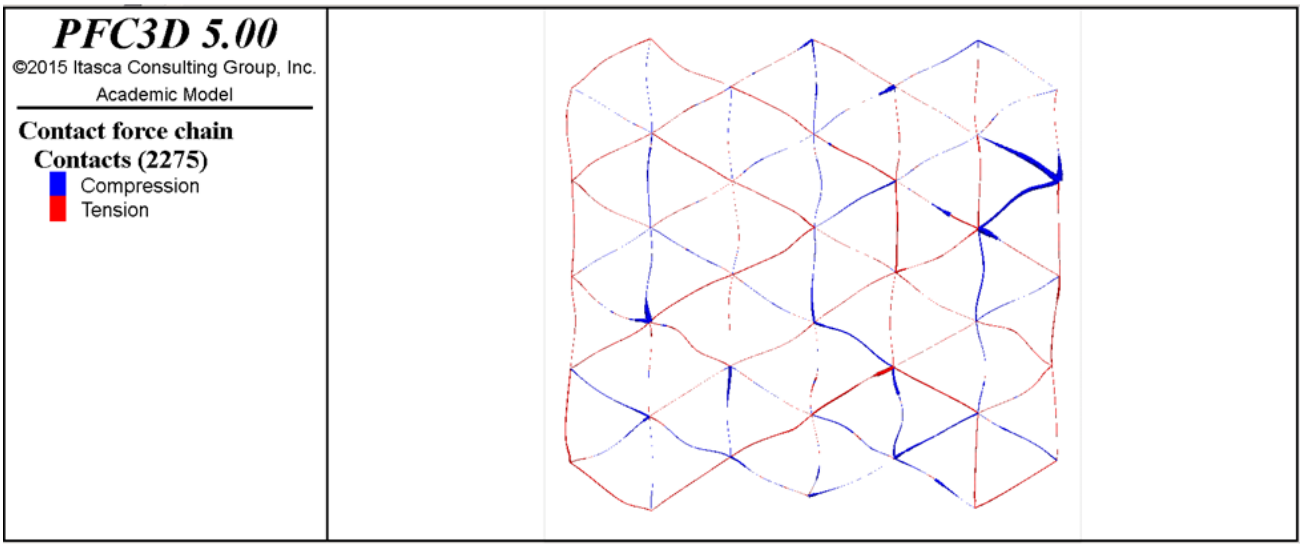

(b).

Figure 5.16 (a). Parallel bond forces and (b.) tensile and compressive forces developed within the geogrid layer for a binary mixture – 50% at 500 loading cycles

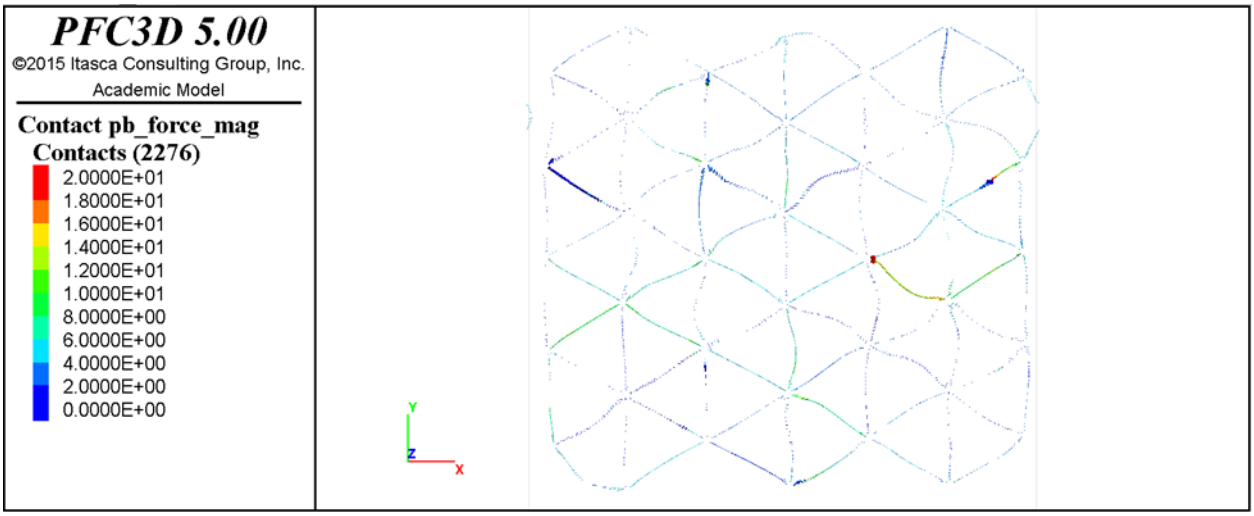

(a).

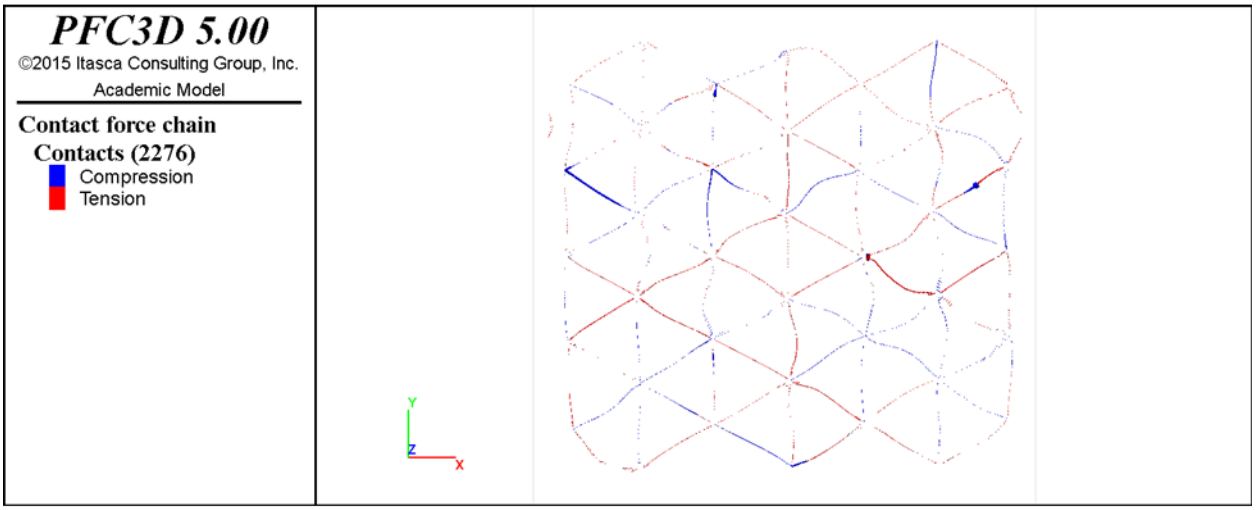

(b).

Figure 5.17 (a). Parallel bond forces and (b.) tensile and compressive forces developed within the geogrid layer for a binary mixture – 70% at 500 loading cycles

The force chains presented in Figure 5.16 and Figure 5.17 are scaled by the magnitude of their force; therefore, as the force increases, the radius of each parallel bond increases, and as the force decreases, the radius of this parallel bonds decreases as well.

Moreover, these force increment are color scaled from blue to red, where blue represents a parallel bond force equal to 0 N, and red represents a parallel bond force equal to 20 N. Lastly, the compressive forces in both figures are represented by blue force chains, and the tensile forces are represented as red force chains.

In Figure 5.16 (a & b) the outline of the multiaxial geogrid specimen is well defined by the parallel bond forces, which indicates that tensile and compressive forces in all the chains of spheres that comprise the geogrid specimen are mobilized, and thus interlocking exists. The blue force chains in Figure 5.16 (b) indicate that compression of these ribs is occurring, which suggests that the particles that were interlocked in the apertures formed by these ribs moved outwards. This behavior indicates that at this time in the test, particle rearrangement is still occurring.

In Figure 5.17 (a & b), the outline of the multiaxial geogrid specimen is poorly defined, since the parallel bond forces within the geogrid were not effectively mobilized. This poor parallel bond definition suggests that lateral forces within the apertures were low, and thus effective geogrid interlocking did not occur at that time. From Figure 5.17 (b) it can be observed that some tensile and compressive forces were developed at different locations within the geogrid. Since it was observed that the geogrid layer placed within a binary mixture – 70% presented a convex deformation, the development of most of these forces were attributed to vertical displacement instead of horizontal displacement.

Further analysis of the lack of stabilization effect of multiaxial geogrids in conjunction with a binary mixture – 70% can be performed by studying the rearrangement of the particles at the interface between the geogrid layer and both binary mixtures. Figure

5.18 presents the evolution of porosity at the interface between the multiaxial geogrid layer and both binary mixtures.

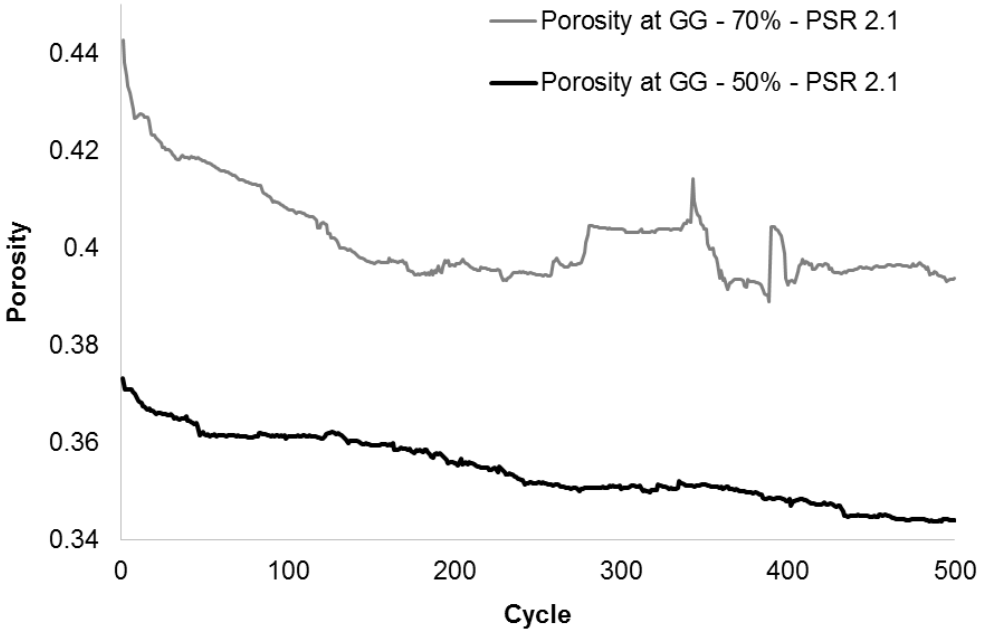

Figure 5.18 Porosity evolution for both binary mixture – 50% and binary mixture - 70% at the geogrid location

This figure indicates that the porosity for both binary mixtures decreased as the amount of loading cycles progressively increased. The porosity for the binary mixture – 70% decreased from 0.44 to 0.39, while the porosity for the binary mixture – 50% decreases from 0.37 to 0.34, which represented a changed in porosity equal to 0.05 and 0.03 for the binary mixture – 70% and 50% respectively. In order to compare these results from a common starting point, the porosity of each binary mixture at this location was normalized by the maximum porosity of each specimen. This procedure allows the study of the change in porosity in terms of the percentage of porosity reduction with respect to its maximum porosity as observed in Figure 5.19.

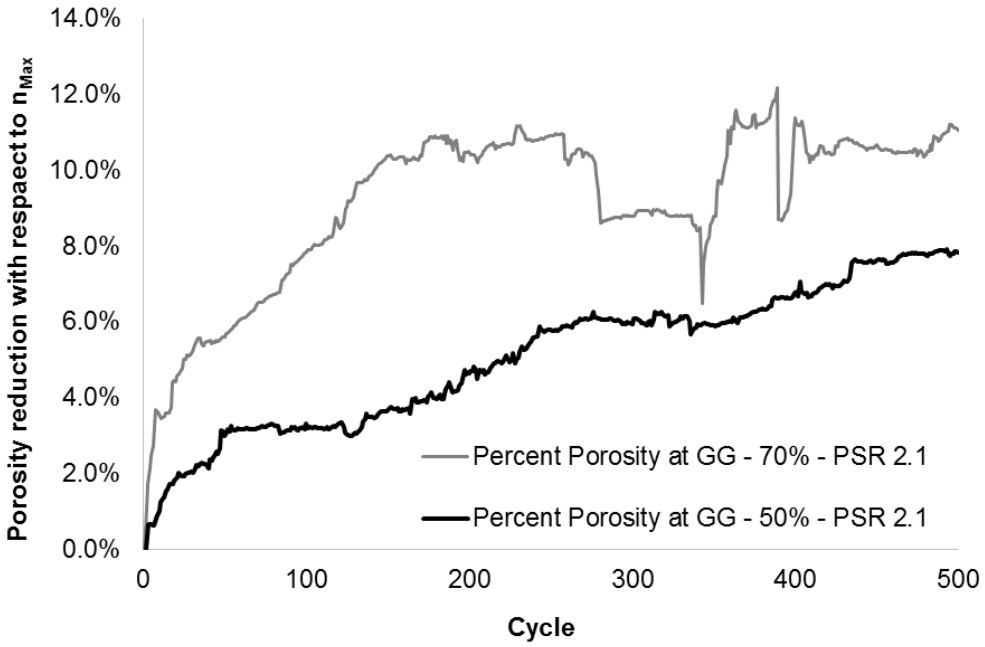

Figure 5.19 Evolution of porosity reduction with respect to n_{Max} for both binary mixture – 50% and binary mixture - 70% at the geogrid location

From Figure 5.19, it can be observed that the reduction in porosity for the binary mixture – 70% is 11.1%, while the reduction in porosity for the binary mixture – 50% is only 7.8%. Although both binary mixtures were exposed to the same loading conditions for the same amount of loading cycles, particle rearrangement, which controls the reduction in porosity at this location, was greater for the binary mixture – 70%. This larger amount of particle rearrangement is most likely caused by the lack of interlocking between the geogrid layer and the particles of the binary mixture – 70%. The reasoning behind this justification is that as larger particles are free to move laterally, continuous movement of smaller particles through the voids occurs, which in the end fills these voids and causes a reduction in porosity.

Another factor that indicates lack of interlocking between the binary mixture – 70% and the geogrid layer is the sudden fluctuation in porosity reduction for this specimen. Lack of interlocking allow particles with large contact forces to surpass the shear resistance at the interface between particles and slip, which potentially creates sudden changes in porosity as observed in Figure 5.19. Had there been optimum interlocking, particle slippage would be hindered, and porosity would not fluctuate so drastically at this location. This rationale is supported by the behavior evidenced for the porosity reduction of the binary mixture – 50%. For this case the porosity reduction increases with a more uniform trend and does not exhibit abrupt changes. This behavior might be the result of particles interlocking in the geogrid apertures more effectively and hindering particle movement and rearrangement at this location.

Lastly, the stabilization of binary mixtures can be assessed by the response of the granular layer beneath the geogrid; therefore, the porosity evolution and the movement of the particles of both binary mixtures beneath the geogrid layer were studied.

Figure 5.20 presents the evolution of the porosity of the particles below the location of the geogrid layer for a geogrid stabilized and non-stabilized binary mixture – 50%. From this figure it is evident that the geogrid stabilized binary mixture exhibits a constant porosity beneath the geogrid later, while the non-stabilized binary mixture exhibits the contrary. In order to compare both cases from a common starting point, the porosity reduction with respect to the maximum porosity observed within each specimen was determined.

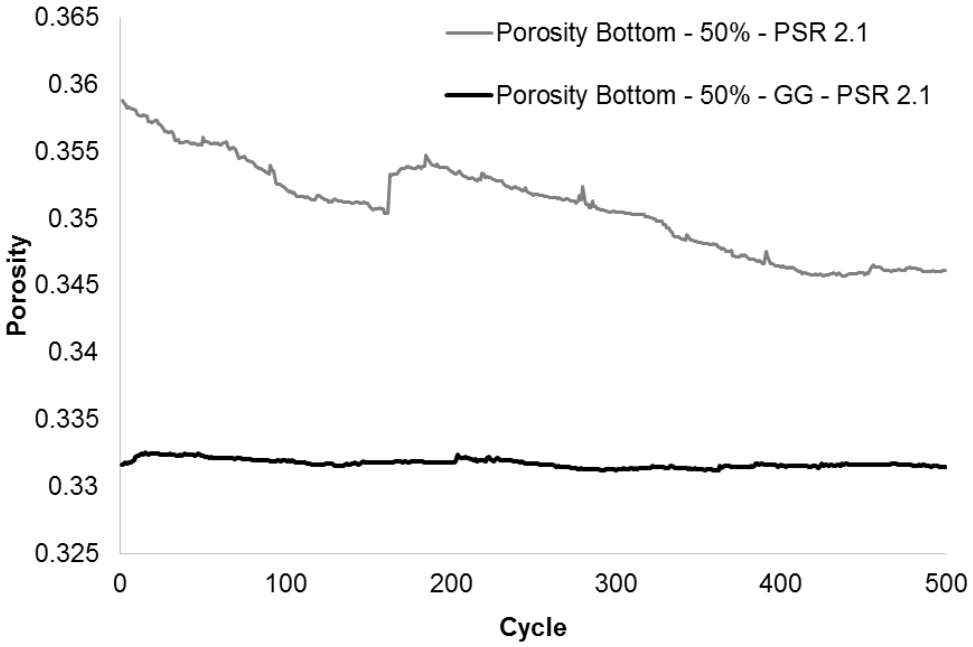

Figure 5.20 Porosity evolution of the particles underneath the geogrid layer location for a binary mixture – 50%

Figure 5.21 presents the porosity reduction difference between the geogrid stabilized specimen and the non-stabilized specimen for a binary mixture – 50%. This figure shows that the non-stabilized binary mixture experienced a porosity reduction equal to 3.7%, while the geogrid stabilized mixture experienced a porosity reduction equal to 0.4%. Additionally, this figure shows a relatively flat porosity reduction trend for the geogrid stabilized binary mixture – 50%, which suggests that significant particle rearrangement did not occur, and that the layer remained stable throughout the duration of the test. This figure also shows a sharper porosity reduction trend for the non-stabilized binary mixture – 50%, which is consistent with particle rearrangement and lack of stabilization. Furthermore, by observing these results, one could argue that particle arrangement of the non-stabilized binary mixture – 50% had not ceased after 500 loading cycles, and it is expected to continue experiencing particle rearrangement and porosity reduction with the

application of additional cyclic loading. This behavior is not anticipated for the geogrid stabilized binary mixture – 50%.

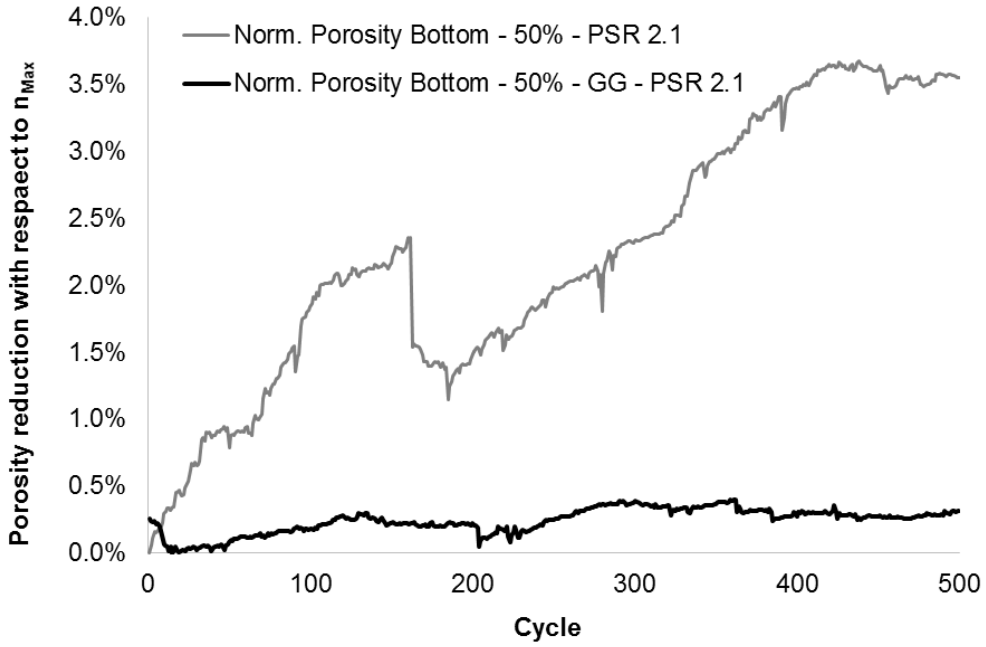

Figure 5.21 Evolution of porosity reduction with respect to n_{Max} for both binary mixture – 50% underneath the geogrid layer location

Figure 5.22 presents the evolution of the porosity of the particles below the location of the geogrid layer for a geogrid stabilized and non-stabilized binary mixture – 70%. From this figure it is clear that both geogrid stabilized and non-stabilized binary mixtures beneath the geogrid later exhibit a similar change in porosity as the simulation was carried out. In this case the stabilizing effect of the multiaxial geogrid was not present, and particle rearrangement occurred at the same scale for both cases throughout most of the test. In order to compare the porosity development for both cases from an equivalent starting point, the porosity reduction with respect to the maximum porosity observed within both geogrid stabilized and non-stabilized binary mixture – 70% was performed.

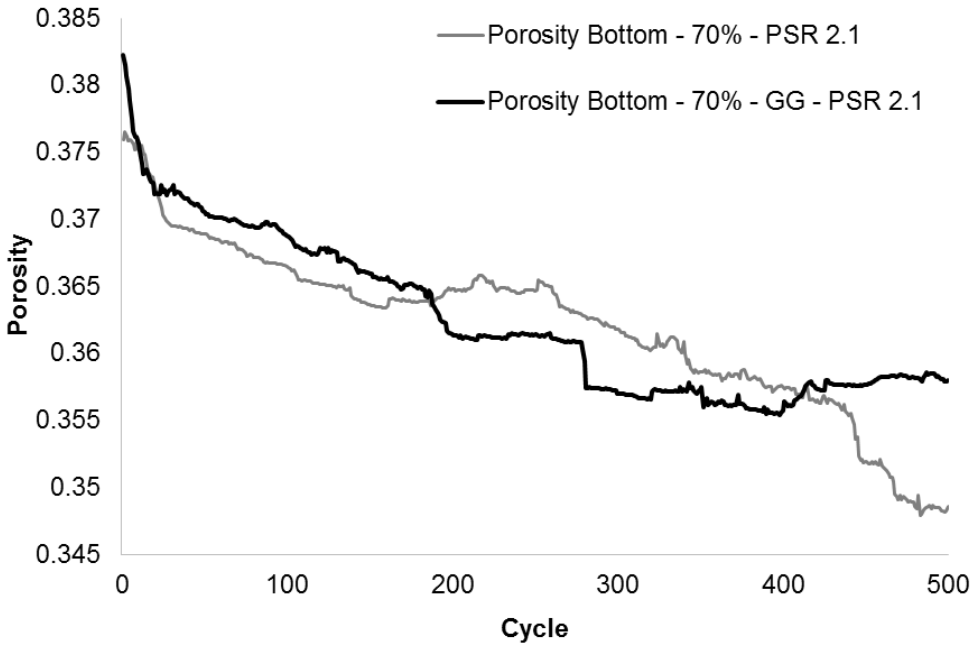

Figure 5.22 Porosity evolution of the particles underneath the geogrid layer location for a binary mixture – 70%

Figure 5.23 presents the porosity reduction with respect to the maximum porosity observed within both geogrid stabilized and non-stabilized binary mixture – 70%. This figure shows that the non-stabilized binary mixture experienced a smaller porosity reduction throughout the entire test until loading cycle 450. At this point the porosity reduction surpassed the porosity reduction of the geogrid stabilized binary mixture and reached a value of 7.4%. The geogrid stabilized mixture exhibited a higher porosity reduction for most of the duration of the test up to 450 loading cycles. At this point the porosity reduction seemed to reach a consistent value of 6.3% for the last 50 loading cycles. This behavior suggests that after 450 cycles some stabilization effect from the geogrid could have been experienced by this layer, and particle rearrangement slowed down.

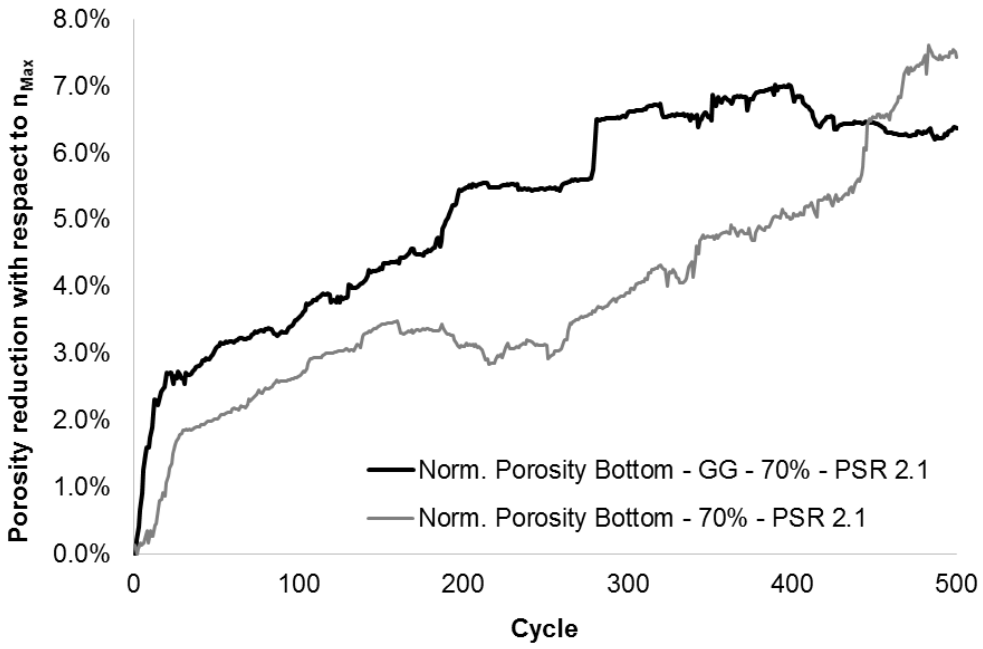

Figure 5.23 Evolution of porosity reduction with respect to n_{Max} for both binary mixture – 70% underneath the geogrid layer location

5.5 Conclusion

By utilizing DEM, the cyclic loading of two geogrid stabilized and non- stabilized binary mixtures with a PSR equal to 2.1 was simulated. After studying their response under cyclic loading, the following conclusions were drawn:

1. A binary mixture – 50% with a PSR equal to 2.1, a D_{max} equal to 30 mm, and a D_{min} equal to 14.3 mm exhibits a satisfactory compatibility with a multiaxial geogrid layer with a rib length equal to 60 mm.

2. A binary mixture – 70% with a PSR equal to 2.1, a D_{max} equal to 42 mm, and a D_{min} equal to 20 mm does not demonstrate an effective compatibility with a multiaxial geogrid with a rib length equal to 60 mm.

3. Development of particle interlocking between a multiaxial geogrid layer and the particles of a binary mixture – 50% was visually observed by dissecting the binary mixture specimen at the geogrid location, and assessing the parallel bond forces mobilized between the particles that comprised the geogrid layer. Interlocking between the multiaxial geogrid layer and the particles of a binary mixture – 70% was not observed.

4. When interlocking is developed between the particles of the binary mixture – 50% and a multiaxial geogrid layer, particle rearrangement and evolution of porosity is reduced, in comparison with non-stabilized binary mixtures.

5. A 33% surface deformation reduction is observed, when a binary mixture – 50% is used versus a binary mixture – 70%, in conjunction with a multiaxial geogrid with a rib length equal to 60 mm.

CHAPTER VI: CONCLUSIONS AND FUTURE WORK

6.1 Conclusions

The Discrete Element Method (DEM) was utilized to model geogrid-stabilized aggregate, and its behavior was studied by applying plate cyclic loading to this composite system in PFC3D. In order to develop a model, which accurately exhibited the properties and behavior of each component in this composite system, the aggregate and the multiaxial geogrid were studied and modeled separately.

Image analysis was performed on four different specimens of aggregate from across the State of Georgia using the University of Illinois Aggregate Image Analyzer (UIAIA), in order to characterize the locally available aggregate. The Flat-and-Elongated (FE) ratio, the Angularity Index (AI), and the Surface Texture (ST) Index were calculated. Aggregate particles were modeled as clumps. Nine different clumps, each with different amount of pebbles, were developed, in order to simulate aggregate particles with different AI. The AI of the clumps was assessed by performing image analysis on three-dimensional (3D) prints of each clump. The results obtained from this procedure exhibit an acceptable AI agreement between hand-calculated values versus computed values by using the UIAIA. Furthermore, aggregate heap simulations using different clumps with the same coefficient of friction were performed, in order to observe the rise in angle of repose due to the change in AI. These simulations were effective in demonstrating that as the AI increases, the angle of repose of the clumps also increases. These results indicated that the clumps developed in this study are suitable for the study of the influence of aggregate morphology in the stabilizing capabilities of multiaxial geogrids

Single rib tensile tests were performed on multiple rib specimens obtained from TX130S, TX140, and TX190L. DEM models of each multiaxial geogrid type were developed by implementing the parallel-bond contact method on chains of spheres. The DEM models developed for TX130S, TX140, and TX190L consisted of 7,065, 6,475, and 2,222 spheres, respectively, and the micromechanical parameters determined for each model were summarized.

The behavior of each multiaxial geogrid model was successfully calibrated against the physical data obtained from the single rib tensile tests. However, it was noted that the geogrid models developed in this study fell short of exhibiting an adequately out-of-plane stiffness response. An attempt to improve this behavior was made, by virtually increasing the cross-sectional area of the ribs, in order to correctly simulate the rib second moment of area (I), and thus increase the flexural rigidity of the member. Although it was determined that this was possible by increasing the radius multiplier (λ) of the parallel bond by a ratio between 15 to 25, a physical meaning to justify the usage of such a radius multiplier was not found; therefore, for the presented simulations a radius multiplier (λ) equal to 1.14 was used pending further studies.

Cyclic load tests were performed on binary mixtures, which were stabilized with a layer of TX190L located at a depth of 125 mm from the subgrade. Two binary mixtures with a particle size ratio of 2.1 were used. The binary mixture – 50% had a D_{max} equal to 30 mm and a D_{min} equal to 14.3 mm, while the binary mixture – 70% had a D_{max} equal to 40 mm and a D_{min} equal to 20 mm. From these simulations it was observed that the binary mixture – 50% exhibited a satisfactory compatibility with TX190L; however, it was also

noted that the binary mixture – 70% did not demonstrate an effective compatibility with the same type of multiaxial geogrid.

This DEM model was effective in providing an insight into the behavior of this composite system, since it permitted the examination of particle interlocking, and the development of tensile and compressive force chains within the multiaxial geogrid model form TX190L. From these results, it was possible to visually determine that optimal interlocking existed between the binary mixture – 50% and the multiaxial geogrid model for TX190L; however, it was also noticed that minor interlocking was developed between the binary mixture – 70% and the multiaxial geogrid model for TX190L, which explained its poor performance. Finally, it was observed that the optimum interaction between the binary mixture – 50% and TX190L hindered the surface deformation by 33% with respect to the non-stabilized case. Furthermore, no stabilizing benefit was observed for the case where the binary mixture – 70% was used.

6.2 Future Work

A number of tasks to continue and expand the study presented herein have been identified and are summarized below.

1. Out-of-plane geogrid stiffness:

   Further study of the implication of the radius multiplier on the out-of-plane stiffness of the geogrid, and development of a multiaxial geogrid model that exhibits a more representative out-of-plane stiffness behavior. In order to do this, a test that assess the out-of-plane stiffness of geogrid ribs should be carried out. Perhaps, compression test of individual ribs, or individual hexagons, could provide insights into the buckling

behavior of the individual ribs, and allow a better evaluation of the out-of-plane stiffness of the physical specimen to then apply to the model.

2. Assessment of Geogrid model complexity:

Multiple studies have shown complex DEM models to simulate the geogrid layer. It would be beneficial for further study of this topic to compare the response of a complex multiaxial geogrid DEM model versus the one presented in this study. Multiple aspects, such as the out-of-plane stiffness, the roughness of the geogrid ribs, and the rib deformation, could be evaluated to determine if the simplified model developed in this study is more effective than the complex models presented elsewhere.

3. Cyclic load test with a binary mixture with a smaller D_{max}:

In order to have a complete image of the compatibility between the multiaxial geogrid model and binary mixtures, an additional cyclic load simulation with a binary mixture – 30% needs to be performed. This simulation could potentially show a geogrid/aggregate compatibility improvement or diminishment, as the particles become smaller. This additional simulation, would bring this study a step closer to identifying the optimum gradation for this type of multiaxial geogrid.

4. Cyclic load test with clumps:

In order to obtain a cyclic loading response more representative to an actual geogrid-stabilized unpaved road section, it is necessary to repeat the simulations presented in this study with the clumps developed in Chapter III. The implementation of clumps is also necessary, in order to study the effect aggregate morphology has in the stabilizing effect of geogrids.

5. Simulations with other Particle Size Ratios:

The simulations presented in the study utilized two binary mixtures with a Particle Size Ratio equal to 2.1. Expansion of the work to include simulations with binary mixtures with different Particle Size Ratios would be evaluated.

6. Simulations with TX130S and TX140:

The simulations presented herein were limited to the study of TX190L multiaxial geogrids. Expansion of the work to include simulations with TX130S and TX140 would be evaluated.

7. Simulations with variation of geogrid location:

The simulations presented herein were performed with the geogrid layer located at the middle of the granular layer. Expansion of the work to include simulations with the geogrid at different elevations would be valuable.

8. Physical cyclic load testing:

The simulation results obtained in this study are an approximation to the actual physical response of geogrid-stabilized unpaved roadways. In order to corroborate that this model is accurately predicting the behavior of such structures and validate the obtained in this study, it is necessary to perform physical cyclic load tests on geogrid-stabilized binary mixtures of aggregate.

APPENDIX A: ANGULARITY INDEX CALCULATION OF A TRIANGLE

1. After the three images of the front, side, and top of the aggregate particle have been acquired, each image is broken into a polygon of 24 segments of equal length.

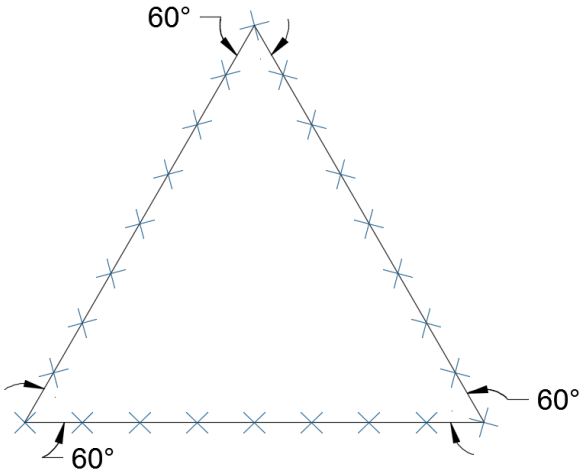

2. The angles at the vertices formed between the lines are computed. These angles are labeled α_1 through α_{24}.

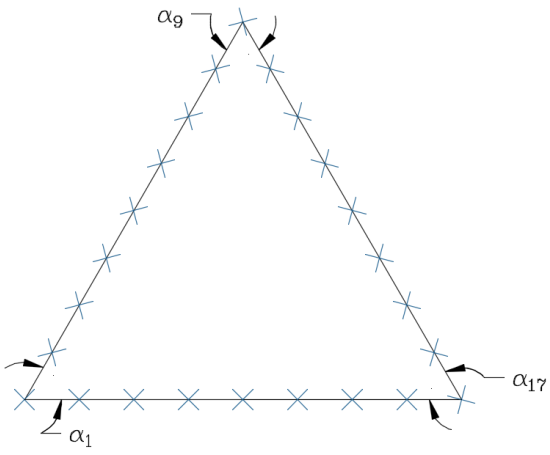

α-Value	Angle (Degrees)	α-Value	Angle (Degrees)
α_1	60	α_{13}	180
α_2	180	α_{14}	180
α_3	180	α_{15}	180
α_4	180	α_{16}	180
α_5	180	α_{17}	60
α_6	180	α_{18}	180
α_7	180	α_{19}	180
α_8	180	α_{20}	180
α_9	60	α_{21}	180
α_{10}	180	α_{22}	180
α_{11}	180	α_{23}	180
α_{12}	180	α_{24}	180

3. The relative change in slope of the sides of the polygon is determined by computing the change in the angle α at each vertices with respect to the previous one. These angle differences are denominated β and are computed in the following fashion: $\beta_1=(\alpha_1-\alpha_2)$, $\beta_2=(\alpha_2-\alpha_3)$,…, $\beta_{24}=(\alpha_{24}-\alpha_1)$. The values obtained by this expression are always positive.

α-Value	Angle (Degrees)	α-Value	Angle (Degrees)
β_1	120	β_{13}	0
β_2	0	β_{14}	0
β_3	0	β_{15}	0
β_4	0	β_{16}	120
β_5	0	β_{17}	120
β_6	0	β_{18}	0
β_7	0	β_{19}	0
β_8	120	β_{20}	0
β_9	120	β_{21}	0
β_{10}	0	β_{22}	0
β_{11}	0	β_{23}	0
β_{12}	0	β_{24}	120

4. A frequency distribution of the β values is developed in 10 degree class intervals; therefore, if a β values is equal to 15°, this value will be accounted for in the class interval 10-20. Class intervals range from 0-10 to 170-180.

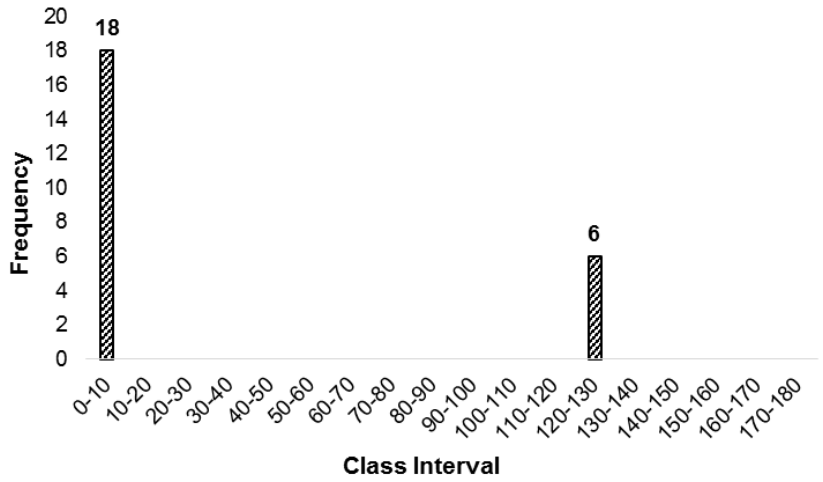

5. The angularity of each face of the aggregate particle is computed by the following equation:

$$A = \sum_{e=0}^{170} e \cdot P(e)$$

Where e = 0, 10, 20, 30… 170, and P(e) is the probability that β has a value in the range of e to e+10 (Rao et al., 2002).

Class interval	Frequency of β	e	P(e)	Angularity
0-10	18	0	1	0
10-20	0	10	0	0
20-30	0	20	0	0
30-40	0	30	0	0
40-50	0	40	0	0
50-60	0	50	0	0
60-70	0	60	0	0
70-80	0	70	0	0
80-90	0	80	0	0
90-100	0	90	0	0
100-110	0	100	0	0
110-120	0	110	0	0
120-130	6	120	1	720
130-140	0	130	0	0
140-150	0	140	0	0
150-160	0	150	0	0
160-170	0	160	0	0
170-180	0	170	0	0
			Angularity	**720**

6. The Angularity Index (AI) of the particle is computed by calculating the weighted average angularity of all three faces with respect to their areas. The following formula is used for this purpose:

$$AI = \frac{\left(Area_{Front} \cdot Angularity_{Front} + Area_{Top} \cdot Angularity_{Top} + Area_{Side} \cdot Angularity_{Side}\right)}{\left(Area_{Front} + Area_{Top} + Area_{Side}\right)}$$

APPENDIX B: CALCULATION OF A 24-SIDED POLYGON FOR IMAGE ANALYSIS PURPOSES

- For the sake of argument let's say a clump consisting of seven pebbles needs to be generated. This clump will consist of six small pebbles that will be equally distributed on the surface of one larger pebble. Since the pebbles around the larger sphere are significantly smaller than the larger particle, they will only be able to fit a triangle within their outline. The larger sphere will be able to fit a polygon with a side count equal to:

$$No.of\ sides\ of\ polygon\ in\ larger\ sphere = 24 - No.of\ small\ spheres$$

- For a regular polygon, the diameter *d* of a circumscribed circle touching the vertices of the polygon is equal to:

$$d = s \cdot \csc\left(\frac{\pi}{n}\right)$$

Where:

s is the length of the side of the polygon.

n is the number of sides of the polygon.

Therefore, if the diameter of the larger pebble d_{large} is known, and the number of sides of the polygon inside of the smaller pebble are also known (3 for a triangle), the following equations can be used to determine the radius of the small pebbles d_{small} to obtain polygons with sides of equal lengths inside the outline of the clump.

$$d_{large} = s \cdot \csc\left(\frac{\pi}{24 - No.small\ pebbles}\right)$$

$$d_{large} = \frac{s}{\sin\left(\frac{\pi}{24 - No.\,small\ pebbles}\right)}$$

$$\therefore s = \sin\left(\frac{\pi}{24 - No.\,small\ pebbles}\right) \cdot d_{large}$$

$$d_{small} = s \cdot \csc\left(\frac{\pi}{3}\right) = \frac{s}{\sin\left(\frac{\pi}{3}\right)}$$

$$\therefore d_{small} = \frac{\sin\left(\frac{\pi}{24 - No.\,small\ pebbles}\right) \cdot d_{large}}{\sin\left(\frac{\pi}{3}\right)}$$

Therefore, for the case of the clump that consists of seven pebbles with a d_{large} equal to 2.0 cm, the length of the sides of the polygon s, and the diameter of the small pebbles d_{small} can be calculated as follows:

$$s = \sin\left(\frac{\pi}{24 - 4}\right) \cdot 2cm = 0.3129\ cm$$

$$d_{small} = \frac{\sin\left(\frac{\pi}{24 - 4}\right) \cdot 2cm}{\sin\left(\frac{\pi}{3}\right)} = 0.3613\ cm$$

As it can be seen in Figure A.3.2, each one of the smaller pebbles on the clump can be outlined with a triangle sides equal to 0.3129 cm long, and the large clump can be outlined with a 20 sided polygon with sides equally long as the triangles.

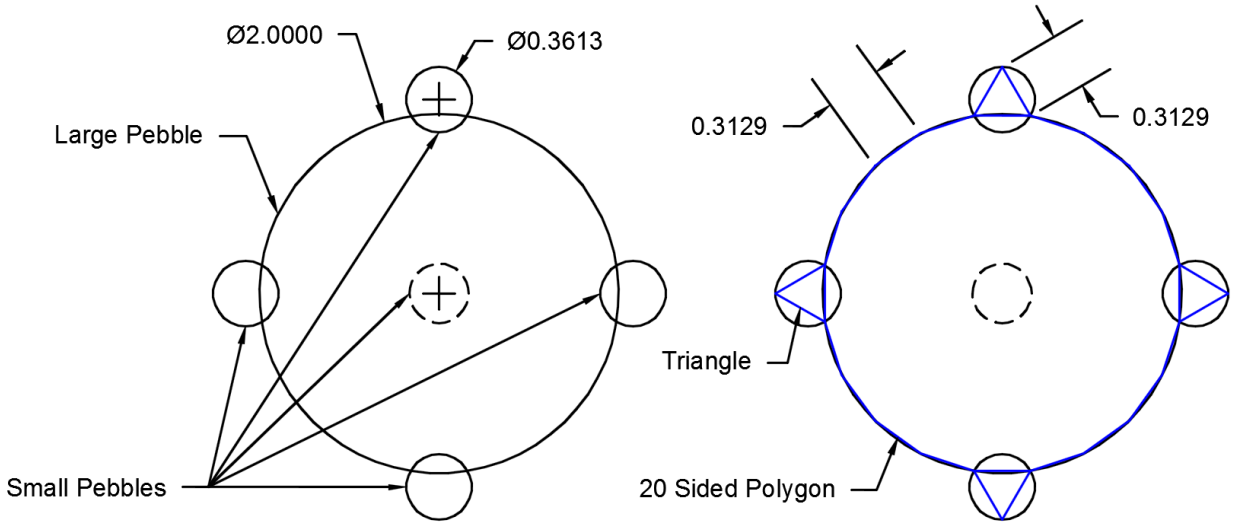

Figure A.3.2 Front view of a seven-pebble clump without and with different polygons demarcating the outline of the clump

REFERENCES

Abu-Farsakh, M., et al. (2011). "Evaluation of factors affecting the performance of geogrid-reinforced granular base material using repeated load triaxial tests." Journal of Materials in Civil Engineering 24(1): 72-83.

Abu-Farsakh, M. Y. and Q. Chen (2011). "Evaluation of geogrid base reinforcement in flexible pavement using cyclic plate load testing." International Journal of Pavement Engineering 12(03): 275-288.

ASTM D6637/D6637M-15, Standard Test Method for Determining Tensile Properties of Geogrids by the Single or Multi-Rib Tensile Method, ASTM International, West Conshohocken, PA, 2015, www.astm.org

ASTM D7748/D7748M-14e1, Standard Test Method for Flexural Rigidity of Geogrids, Geotextiles and Related Products, ASTM International, West Conshohocken, PA, 2014, www.astm.org

Barker, W. R. (1987). “Open-Graded Bases for Airfield Pavements”, Miscellaneous Paper GL-87-16, US Army Engineer Waterways Experiment Station, Vicksburg, MS.

Barrett, P. (1980). "The shape of rock particles, a critical review." Sedimentology 27(3): 291-303.

Brown, S., et al. (2007). "Identifying the key parameters that influence geogrid reinforcement of railway ballast." Geotextiles and Geomembranes 25(6): 326-335.

Chan, F., et al. (1989). "Aggregate base reinforcement of surfaced pavements." Geotextiles and Geomembranes 8(3): 165-189.

Chen, C., et al. (2012). "Discrete element modelling of cyclic loads of geogrid-reinforced ballast under confined and unconfined conditions." Geotextiles and Geomembranes 35: 76-86.

Chen, C., et al. (2013). "A study of geogrid-reinforced ballast using laboratory pull-out tests and discrete element modelling." Geomechanics and Geoengineering 8(4): 244-253.

Chen, C., et al. (2014). "Investigating geogrid-reinforced ballast: Experimental pull-out tests and discrete element modelling." Soils and Foundations 54(1): 1-11.

Chen, C. and G. R. McDowell (2014). "An investigation of the dynamic behavior of track transition zones using discrete element modelling." Proceedings of the Institution of Mechanical Engineers, Part F: Journal of Rail and Rapid Transit: 0954409714528892.

Chen, J., et al. (2012). “Mechanical Evaluation of Different-Size Particles in Compacted Aggregate Structure Using Three-Dimensional Discrete Element Method”. CICTP 2012: Multimodal Transportation Systems—Convenient, Safe, Cost-Effective, Efficient, Beijing, China, American Society of Civil Engineers.

Cho, G.-C., et al. (2006). "Particle shape effects on packing density, stiffness, and strength: natural and crushed sands." Journal of Geotechnical and Geoenvironmental Engineering 132(5): 591-602.

Cundall, P. A. and O. D. Strack (1979). "A discrete numerical model for granular assemblies." Geotechnique 29(1): 47-65.

Fannin, R. and O. Sigurdsson (1996). "Field observations on stabilization of unpaved roads with geosynthetics." Journal of Geotechnical Engineering 122(7): 544-553.

Ferellec, J.-F. and G.R McDowell (2012). "Modelling of ballast–geogrid interaction using the discrete-element method." Geosynthetics International 19(6): 470-479.

Ferellec, J.-F. and G.R. McDowell (2010). "A method to model realistic particle shape and inertia in DEM." Granular matter 12(5): 459-467.

Fuggle, A. R., et al. (2014). “Size effects on the void ratio of loosely packed binary particle mixtures”. Geo-Congress 2014 Technical Papers: Geo-characterization and Modeling for Sustainability, ASCE.

Gere, J. M. and B. J. Goodno (2009). “Mechanics of materials”. Toronto ON, Cengage Learning

Giroud, J., et al. (1985). “Design of unpaved roads and trafficked areas with geogrids”. Polymer grid reinforcement – Conference proceedings, Thomas Telford Publishing: 116-127.

Giroud, J. and J. Han (2004). "Design method for geogrid-reinforced unpaved roads. I. Development of design method." Journal of Geotechnical and Geoenvironmental Engineering 130(8): 775-786.

Guo, P. and X. Su (2007). "Shear strength, interparticle locking, and dilatancy of granular materials." Canadian Geotechnical Journal 44(5): 579-591.

Haas, R., et al. (1987). “Granular base reinforcement of flexible pavements using geogrids”. Proceedings of Geosynthetics’ 87.

Hufenus, R., et al. (2006). "Full-scale field tests on geosynthetic reinforced unpaved roads on soft subgrade." Geotextiles and Geomembranes 24(1): 21-37.

Indraratna, B., et al. (2013). "The lateral displacement response of geogrid-reinforced ballast under cyclic loading." Geotextiles and Geomembranes 39: 20-29.

Indraratna, B., et al. (2012). "On the shear behavior of ballast-geosynthetic interfaces." Geotechnical Testing Journal 35(2): 1-8.

Itasca (2015). “Particle Flow Code (PFC) in three dimension”. Minnesota. Itasca Consulting Group, Inc.

Jas, H., et al. (2015). “Discrete Element Modeling of a Trafficked Sub-Base Stabilized With Biaxial and Multiaxial Geogrids to Compare Stabilization Mechanisms”. Geosynthetics, Portland OR.

Jenner, C. (2009). “Significant Developments over the Last 25 Years”. Jubilee Symposium on Polymer Geogrid Reinforcement, London, United Kingdom.

Jensen, R. P., et al. (1999). "DEM simulation of granular media—structure interface: effects of surface roughness and particle shape." International Journal for Numerical and Analytical Methods in Geomechanics 23(6): 531-547.

Koerner, R. M. (2009). “An Overview of Geogrids”. Jubilee Symposium on Polymer Geogrid Reinforcement, London, United Kingdom.

Konietzky, H., et al. (2004). "Use of DEM to model the interlocking effect of geogrids under static and cyclic loading." Numerical modeling in micromechanics via particle methods: 3-12.

Kuo, C.-Y., et al. (1996). "Three-dimensional image analysis of aggregate particles from orthogonal projections." Transportation Research Record: Journal of the Transportation Research Board (1526): 98-103.

Kwon, J., et al. (2015). "Characterization of unbound aggregate materials considering physical and morphological properties." International Journal of Pavement Engineering: 1-6.

Leng, J. and M. Gabr (2002). "Characteristics of geogrid-reinforced aggregate under cyclic load." Transportation Research Record: Journal of the Transportation Research Board (1786): 29-35.

Love, J., et al. (1987). "Analytical and model studies of reinforcement of a layer of granular fill on a soft clay subgrade." Canadian Geotechnical Journal 24(4): 611-622.

Lu, M. and G. McDowell (2007). "The importance of modelling ballast particle shape in the discrete element method." Granular matter 9(1-2): 69-80.

McDowell, G., et al. (2006). "Discrete element modelling of geogrid-reinforced aggregates." Proceedings of the Institution of Civil Engineers-Geotechnical Engineering 159(1): 35-48.

McGeary, R. (1961). "Mechanical packing of spherical particles." Journal of the American ceramic Society 44(10): 513-522.

Milligan, G., et al. (1989). "A New Approach to the Design of Unpaved Roads - Part 1." Ground Engineering 22(3).

Miura, N., et al. (1990). "Polymer grid reinforced pavement on soft clay grounds." Geotextiles and Geomembranes 9(1): 99-123.

Montanelli, F., et al. (1997). “Geosynthetic-reinforced pavement system: testing and design”. Proceeding of Geosynthetics.

Nazzal, M., et al. (2007). "Laboratory characterization of reinforced crushed limestone under monotonic and cyclic loading." Journal of Materials in Civil Engineering 19(9): 772-783.

Ngo, N. T., et al. (2014). "DEM simulation of the behavior of geogrid stabilized ballast fouled with coal." Computers and Geotechnics 55: 224-231.

O'Sullivan, C. (2011). “Particulate discrete element modelling”, Taylor & Francis.

Pan, T. and E. Tutumluer (2006). "Quantification of coarse aggregate surface texture using image analysis." Journal of testing and evaluation 35(2): 1-10.

Perkins, S. and M. Ismeik (1997). "A Synthesis and Evaluation of Geosynthetic-Reinforced Base Layers in Flexible Pavements-Part II." Geosynthetics International 4(6): 605-621.

Qian, Y., et al. (2011). "Stress Analysis on Triangular-Aperture Geogrid-Reinforced Bases over Weak Subgrade under Cyclic Loading: An Experimental Study." Transportation Research Record: Journal of the Transportation Research Board (2204): 83-91.

Qian, Y., et al. (2012). "Performance of triangular aperture geogrid-reinforced base courses over weak subgrade under cyclic loading." Journal of Materials in Civil Engineering 25(8): 1013-1021.

Qian, Y., et al. (2013). “Comparative evaluation of different aperture geogrids for ballast reinforcement through triaxial testing and discrete element modeling”. Geosynthetics 2013.

Qian, Y., et al. (2011). “A validated discrete element modeling approach for studying geogrid-aggregate reinforcement mechanisms”. Geo-Frontiers Congress 2011.

Rao, C., et al. (2002). "Quantification of coarse aggregate angularity based on image analysis." Transportation Research Record: Journal of the Transportation Research Board (1787): 117-124.

Rao, C., et al. (2001). "Coarse aggregate shape and size properties using a new image analyzer." Journal of testing and evaluation 29(5): 461-471.

Schuettpelz, C., et al. (2009). "Evaluation of the zone of influence and stiffness improvement from geogrid reinforcement in granular materials." Transportation Research Record: Journal of the Transportation Research Board (2116): 76-84.

Shamsi, M. M. and A. Mirghasemi (2012). "Numerical simulation of 3D semi-real-shaped granular particle assembly." Powder technology 221: 431-446.

Stahl, M., et al. (2014). "Discrete element simulation of geogrid-stabilized soil." Acta Geotechnica 9(6): 1073-1084.

Sukumaran, B. and A. Ashmawy (2001). "Quantitative characterization of the geometry of discrete particles." Geotechnique 51(7): 619-627.

Tingle, J. and S. Webster (2003). "Corps of Engineers Design of Geosynthetic-Reinforced Unpaved Roads." Transportation Research Record: Journal of the Transportation Research Board (1849): 193-201.

Georgia Department of transportation (GDOT) (2016). “Office of Materials and Testing Qualified Products List”. Atlanta GA. Available at: http://www.dot.ga.gov/PartnerSmart/Materials/Documents/qpl02.pdf. Accessed April 15. 2014.

Tutumluer, E., et al. (2010). "Geogrid-Aggregate interlock mechanism investigated through aggregate imaging-based discrete element modeling approach." International Journal of Geomechanics 12(4): 391-398.

USGS (2005). “Digital Geologic Map of Georgia (Ver. 2)”, United States Geological Survey

Walls, J. and L. Galbreath (1987). “Railroad ballast reinforcement using geogrids”. Proceedings of geosynthetics 1987.

Webster, S. L. (1993). ‘‘Geogrid reinforced base courses for flexible pavements for light aircraft: Test section construction, behavior under traffic, laboratory tests, and design criteria.’’ Final Rep., DOT/FAA/RD-92/25, U.S. Department of Transportation and Federal Aviation Administration, 91 pp.

Xiao, Y., et al. (2014). DEM Approach for Engineering Aggregate Gradation and Shape Properties Influencing Mechanical Behavior of Unbound Aggregate Materials. Geo-Congress 2014 Technical Papers: Geo-characterization and Modeling for Sustainability, ASCE.

Xiao, Y., et al. (2012). "Gradation effects influencing mechanical properties of aggregate base-granular subbase materials in Minnesota." Transportation Research Record: Journal of the Transportation Research Board (2267): 14-26.

Zheng, J. and R. Hryciw (2015). "Traditional soil particle sphericity, roundness and surface roughness by computational geometry." Geotechnique 65(6): 494-506.

Zhou, W., et al. (2013). "Influence of particle shape on behavior of rockfill using a three-dimensional deformable DEM." Journal of Engineering Mechanics 139(12): 1868-1873.